Stochastic Real-Time Flood Forecasting Using Weather Radar and a Distributed Hydrologic Model

By

KIM Sunmin

2006

Stochastic Real-Time Flood Forecasting Using Weather Radar and a Distributed Hydrologic Model

By

KIM Sunmin

A Dissertation

Submitted in partial fulfillment of the requirement for the Degree of Doctor of Engineering of Kyoto University, Japan

August 2006

Acknowledgements

All the work that I did in this doctoral thesis were carried out in Professor Takara's laboratory in Disaster Prevention Research Institute, Kyoto University, Japan. This work has been made possible through the help of a number of people who I would like to thank.

It is difficult not to overstate my thankfulness to Professor Kaoru TAKARA for his valuable supervision, continuous encouragement and support throughout my research and stay in Japan. I am grateful to Associate Professor Yasuto TACHIKAWA for his valuable teaching and restless effort to guide my research. Without their assistance and openness in inviting me to Japan and in providing a comfortable research environment, my work with Kyoto University would not have been possible. A special gratitude is also due to Professor Michiharu Shiiba and Professor Eiichi Nakakita for the invaluable guidance and comments on my research.

Sincere thanks are extended to the members of our laboratory, Innovative Disaster Prevention Technology and Policy Research Laboratory. I am grateful to Assistant Professor Takahiro Sayama for his many positive comments on my work. I express my thanks to Ms. Keiko Kanzaki, the secretary of our laboratory, for her tireless support in all kinds of administrative tasks. I express my thanks to Dr. Shen Chiang, Dr. Rohan Kumar Shresta, Dr. NMNS Bandara Nawarathna as well as many other former students and researchers of our laboratory, for the invaluable discussions and conversations we have shared, for their support over the years in helping me to make the most of my time in Japan, and for their friendship. I would also like to thank my fellow students Giha Lee (who is also my old friend), Mondonedo Carlo, Minh Nhat Le, Apip, as well as many other members including Dr. Dayong Shen. Their valuable comments and help made it possible to achieve my research career.

I am indebt to Professor Kwansue JUNG of Chungnam National University, Korea for his unforgettable help and guidance during my time as an undergraduate and master

course student. Thanks are also extended to Dr. Hyoseob Cho and Dr. Jungyeob Kim who were excellent teachers as well as research partners even until now.

Finally, I would like to deeply thank my parents and my two brothers for all their love, encouragement and understanding during my long stay abroad.

August 24, 2006

KIM Sunmin

Contents

List of Figures

List of Tables

Chapter 1

Introduction

Water is an essential material for human beings. However, it can cause severe problems when this material becomes scarce or excessive in our life. For the proper control and usage of water, we have tried to understand the cycle of water in our living environments. Hydrology is the study of understanding water cycles on the earth in order to avoid water quantity problems, droughts and floods.

> "The world is experiencing a dramatic increase of suffering from the effects of disasters, ranging from extreme droughts to huge floods, caused by the poor management of water and land and possibly by climate change. Human society and particularly the poor are becoming more vulnerable to such disasters." (UNESCO-WWAP, 2003)

Floods have been in conflict with humankind since we have existed, and have become a serious issue especially since mass settlement and residential improvements. Following an explosive increase in population in the last century, several factors such as urbanization, deforestation, and denser occupancy of flood plains are believed to amplify flood disaster. Furthermore, a flood of large magnitude would nowadays produce big property losses compared to earlier days as society has become highly sophisticated and industrialized.

There are two main types of countermeasures for flood problems: 'structural' and 'non-structural.' Structural countermeasure is mostly uses for flood protection via hydrologic structures, such as dam construction, channel embankment, etc. Non-structural countermeasure, however, emphasizes and implements various ways to decrease flood damages before, during and after floods. Flood forecasting and floodplain management take a main roll in non-structural countermeasure.

No matter how much engineers try to prevent or control floods by use of huge structures, there are currently no possible means for being absolutely free from flood related problems. In addition, engineering is a matter of economics. In some cases, it would economically be much better to allow a flood to happen and reestablish the flooded area rather than rebuild the entire channel network wasting large amounts of money. However, even in such a situation, we must be aware of the time and magnitude of the possible flood in order to safely evacuate the people and save as much property as possible. Real-time flood forecasting is therefore the job of anticipating flood danger and allows sufficient time for necessary preparation.

1.1 Background

The advances in knowledge and technology up to now have increased the performance of flood forecasting. Hydrologists have understood the detailed physics of water movement with various analytical and empirical equations. At the same time, progress in other fields of engineering has produced methodologies that can observe and efficiently handle vast amounts of meteorological and hydrological data. It is now possible to simulate sophisticated meteorological and hydrological phenomena with physics-based models. Data collecting techniques using remote sensing as well as increased computational technology have harnessed more accurate flood forecasting on a real-time basis.

However, even with powerful technology and advanced knowledge, it is hard to determine whether current flood forecasting is successful or not since the results still fall short of what is required, especially in short-term forecasting. The efficiency of short-term flood forecasting is highly affected by the quality of the input data, namely precipitation, which is known for being difficult to accurately forecast. Furthermore, with very short lead times, high spatial and temporal resolution of precipitation data is required for forecasting of flash floods (Golding, 2000). To satisfy the demand for high quality precipitation forecasting, many studies are focusing on specialized schemes, such as hybrid numerical prediction and radar image extrapolation.

For any natural phenomenon scientists try to forecast, if the spatiotemporal boundary or initial condition were to be exactly known, and if the model were to simulate the process exactly, the computed phase path would thus provide an exact forecast. However, neither assumption is valid based on current technology or knowledge. One should bear in mind that there will always be an initial error in the model at the beginning of simulation and there will always be additional errors during a simulation due to the imperfection of the model's structure. To estimate the effect of the errors from the forecasts' results, it is necessary to supplement such deterministic forecasts with detailed information by estimates of forecast reliability. By this reason, the stochastic concept has been included in forecasting, and ensemble simulation has been used as an effective tool for incorporating stochastic concepts into computer simulation.

However, when considering that most ensemble forecasting relies on the probable initial analysis, the benefits of ensemble simulation is maximized under the condition in which the systematic error of a model is relatively small compared to the initial condition sensitivity (Du and Mullen, 1997). Because of this quality, ensemble forecasting has been criticized for ignoring its external error growth and, as a result, usually fails to include all sources of uncertainty in the forecasting (Leith, 1974; Krysztofowicz, 2001). An alternative to fill the shortage of the current ensemble techniques and to strengthen the reliability of the scheme is to give a continuous correction of forecasting results or model behavior itself by using the most updated observation. The continuous refinement of ensemble forecasting and/or model structure in order to get results that are more accurate is the main subject to be discussed in this study.

1.2 Objectives of the Study

This study discusses stochastic real-time flood forecasting with radar observation and a distributed hydrologic model. A new attempt of ensemble rainfall-runoff prediction is introduced with probabilistic radar rainfall forecasting and recursive measurement updating in a distributed hydrologic model. Detailed objectives of this study are as follows:

- To examine the availability of radar observed data in flood forecasting
- To understand radar image extrapolation methods for short-term rainfall forecasting
- To analyze error structures in the rainfall forecasting with consideration towards the deterministic characteristics of extrapolation methods
- To develop a prediction error simulation model for improved reliability and accuracy with radar rainfall forecasting
- To understand the behavior of a distributed hydrologic model
- To consider state variables in a distributed hydrologic model that are continuously updated through use of observed discharge data
- To couple the Kalman filter with a distributed hydrologic model for a recursive updating of state variables
- To consider the ensemble simulation method for stochastic flood forecasting

1.3 Outline of Thesis

This thesis mainly consists of two parts in discussing stochastic real-time flood forecasting. The first section focuses on stochastic radar rainfall forecasting using radar image extrapolation and prediction error simulation (Chapters 2 and 3). The second section focuses on recursive updating of state variables in a distributed hydrologic model based on the Kalman filter algorithm (Chapters 4 and 5).

In Chapter 2, short-term forecasting of precipitation using radar observation is explained. After a short review of weather radar usage in hydrology for nowcasting of precipitation, an extrapolation scheme of radar imagery is illustrated with an introduction of the Translation model (Shiiba *et al*., 1984). The radar extrapolation model projects deterministic rainfall prediction. Its prediction error structure is then analyzed by comparing the observed rainfall fields to obtain error results. Properly analyzed error structure can be used as vital information for improving the forecast accuracy and providing its reliability (Kim *et al*., 2005b).

A new attempt of ensemble rainfall forecast is introduced in Chapter 3 by use of a spatial random error field simulation. As opposed to a conventional ensemble simulation that uses initial condition control to obtain a statistical outcome, stochastic prediction error fields are generated to offer probable variations of deterministic predictions. For the error field generation, spatially correlated random errors are simulated using a covariance matrix decomposition method. The prediction error fields, which successfully keep the analyzed error structure, improve the accuracy of the deterministic rainfall prediction (Kim *et al.*, 2006). The random error fields along with the deterministic fields are thereafter tested with a distributed hydrologic model to measure its validity on an ensemble runoff prediction.

Chapter 4 describes the distributed hydrologic model, CDRMV3 (Kojima *et al.*, 2003), and discusses updating methodologies of distributed state variables in the model. During runoff simulation, inappropriate rearrangement of the spatial distribution of state variables produces negative effects towards the runoff simulation results (Kim *et al*., 2004). To avoid an unpredictable collapse of the internal model state throughout a simulation, an updating method introduced in this study retains the spatial distribution pattern of the state variables. This is conducted before and after the updating by using a ratio of total storage amount or outlet discharge.

The objective of Chapter 5 is to couple the Kalman filter into a physically based distributed model and test the performance of the coupled model under real-time conditions. For the incorporation of the filtering concept into a distributed model, there are several hurdles to be overcome. First of all, Monte Carlo simulation method makes it possible to project a nonlinear variation of system states and their error covariance without the need for linearized system equations. Secondly, as an alternative to the linear observation function, this study introduces an external relationship of observed data and the internal state variables of the hydrologic model. Here, the observed data is defined as outlet discharge and the state variable in the Kalman filter algorithm is the total amount in storage in the basin. The developed Kalman filter coupled with the distributed hydrologic model can incorporate the uncertainty of input and output measurement data as well as the uncertainty in the model's structure (Kim *et al*., 2005a).

Finally, Chapter 6 summarizes the study with a concluding remark.

References

Du, J. and Mullen, S. L. (1997): Short-range ensemble forecasting of quantitative precipitation, Monthly Weather Rev., Vol.125, pp. 2427-2459.

Golding, B. W. (2000): Quantitative precipitation forecasting in the UK, J. Hydrol., Vol.239, pp. 286-305.

Kim, S., Tachikawa, Y. and Takara, K. (2004): Real-time updating of state variables in a distributed hydrologic model, Annuals of DPRI, Kyoto University, No. 47B, pp. 273-282.

Kim, S., Tachikawa, Y. and Takara, K. (2005a): Real-time prediction algorithm with a distributed hydrologic model using Kalman filter, Annual of Hydraulic Engineering, JSCE, Vol. 49, pp. 163-168.

Kim, S., Tachikawa, Y. and Takara, K. (2005b): Rainfall-runoff prediction considering error structure of the predicted rainfall, Annuals of DPRI, Kyoto University, No. 48B, pp. 53-58.

Kim, S., Tachikawa, Y. and Takara, K. (2006): Ensemble rainfall-runoff prediction with radar image extrapolation and its error structure, Annual of Hydraulic Engineering, JSCE, Vol. 50, pp. 43-48.

Kojima, T. and Takara, K. (2003): A grid-cell based distributed flood runoff model and its performance, Proceding of symposium HS03, Weather radar information and distributed hydrological modeling, IAHS Publ. No. 282, pp. 234-240.

Krzysztofowicz, R. (2001): The case for probabilistic forecasting in hydrology, Journal of Hydrology, Vol 249, pp. 2-9.

Leith, C. E. (1974): Theoretical skill of Monte Carlo forecasts, Monthly Weather Rev., Vol.102, pp. 409-418.

Shiiba, M., Takasao, T. and Nakakita, E. (1984): Investigation of short-term rainfall prediction method by a translation model, Jpn. Conf. on Hydraul., 28th, pp. 423-428.

UNESCO-WWAP, (2003): Water for people water for life, The United Nations World Water Development Report, 2003.

Chapter 2

Short-term Forecasting of Precipitation with Weather Radar

> "For operational forecasting of river flow and flash floods, dense rain gage observations (telemetered) are desirable, but their installation has not been practical. Thus there has been considerable interest in utilizing weather radar, since it provides spatially and temporally continuous measurements that are immediately available at one location." (Wilson and Brandes, 1979)

Radar rainfall estimation and its utilization into flood forecasting has received growing attention in operational hydrology since Marshall and Palmer (1948) proposed the theory of drop size distribution. Nowadays, radar observed rainfall has became one of the most demanded data to hydrologists with a growing interest in distribute hydrologic modeling. However, there is continuous research on improving the radar's estimation accuracy of quantitative precipitation, as there is still vast amounts to improve upon when it is applied to flood forecasting.

This chapter presents weather radar usage in hydrology, especially in short-term forecasting of precipitation. First of all, a radar image extrapolation method is explained following with an introduction of the Translation model, that has been used in this study. Extrapolation of rainfall cells' movement is the most commonly used method in radar rainfall forecasting. As the next step, prediction error characteristics of the Translation model (Shiiba *et al.*, 1984) are analyzed for a deeper understanding of the model behavior and for improvement of forecasting accuracy. The analyzed error characteristics include basic statistics, such as the mean and standard deviation, as well as spatial correlation of errors as time passes. Finally, spatiotemporal distribution patterns of the errors are also analyzed. Properly analyzed error structure can be stochastically used as valuable information for providing updated reliability of forecasting (Kim *et al.*, 2005; Kim *et al.*, 2006).

2.1 Weather Radar in Hydrology

2.1.1 Radar Rainfall Estimation

Weather radars are an appealing instrument for observing rainfall over large spatial domains within fine time resolutions. The usual C-band radar (wave length 4~8cm, see Table 2.1 for more details on band types) quantitatively covers an area of 120 km radius and produces one set of cylinder shape observations down to every five minutes. After a 3-dimentional volume scanning, a horizontal radar projection at a specific altitude, or CAPPI (Constant Altitude Planned Position Indicator), is calculated. Rainfall intensity is estimated from this single horizontal section of radar reflectivity based on analytical and/or empirical relationships of the intensity and reflectivity.

Table 2.1 Weather radar band types and its characteristics.

	Wavelength	Frequency	Characteristics
S band	8~15cm	2~4GHz	Not easily attenuated, near and far range weather observation
C band	4~8cm	4~8GHz	More easily attenuated, short range weather observation
X band	2.5~4cm	8~12GHz	Possible to detect smaller particles, very short range weather observation

Marshall-Palmer's exponential drop-size distribution (Marshall and Palmer, 1948) is believed to be one of the most prominent works in weather radar research. The drop-size distribution is a simple function of the rain rate, which leads to a relation between radar reflectivity Z and rain rate R. Radar reflectivity is the received radiation power of backscattered signals from precipitation particles. Assuming the backscattered power is proportional to the summation of the sixth power of particle diameters in a unit volume, the radar reflectivity can be written as:

$$Z = \sum N_i D_i^6 = \int N(D) D^6 dD \tag{2.1}$$

where N_i is number of drops per unit volume having diameter D_i and $N(D)dD$ is the number of drops with diameters between D and dD. The unit of drop size is in *mm* and the volume is in *m*, so that Z is in units of mm^6/m^3. Assuming that rainfall rate R is related to D and the drop terminal velocity of a drop $V(D)$ as:

$$R = \frac{\pi}{6}\int N(D)D^3V(D)dD \tag{2.2}$$

leads to an expression of Z and R in the form:

$$Z = BR^{\beta} \tag{2.3}$$

Thus, if the drop-size distribution were exponentially known and if the vertical air motions are low relative to the drop terminal velocities, the accuracy of the radar rainfall estimation using equation 2.3 would have no limit (Wilson and Brandes, 1979). However, due to the uncertainty of the drop-size distribution and the terminal velocities, the *Z-R* relationship is not unique and therefore generates numerous empirical relationships. Because radar does not measure rainfall intensities directly, but rather the backscattered energy from precipitation particles, radar is prone to errors from many other sources. The error sources of radar rainfall estimation, which also incorporate radar systematic errors, are:

1) Incorrect relationship between the reflectivity and rainfall intensity

2) Height dependent variation of the reflectivity measurement

3) Ground echoes or blockage of the signal by any obstacle

4) Attenuation of the signal by precipitation

5) Systematic errors due to radar hardware calibration

Details of radar rainfall observation including error sources can be found in Wilson and Brandes (1979) and Einfalt *et al.* (2004) with well-documented research reviews.

The most general and successful techniques for improving radar rainfall estimates is the adjustment of radar observation with ground rain gauges. Both measurement devices are often times complementary, thus, the concurrent use of both can provide the best spatial estimate of rainfall for hydrological applications (Einfalt *et al.*, 2004). There are many ways in utilizing rain gauge observations to adjust the radar estimate, which has proven to be a major research subject still being conducted today.

2.1.2 Nowcasting of Precipitation

Nowcasting of precipitation is an essential prerequisite for real-time flood forecasting in operational hydrology. The term "nowcasting" is used to emphasize the specificity and shortness (0~3hrs) of rainfall forecast largely by radar image extrapolation, a method going back nearly 50 years (e.g. Smith and Austin, 2000; Fox and Wilson, 2005). Even though the benefits of short-term precipitation forecasts are well known, it is acknowledged as being among the most challenging areas in hydrology and meteorology (Collier and Krzysztofowicz, 2000).

Forecast techniques using radar observations are based on tracking past movements of rain cells and extrapolating those movements, assuming that rainfall intensities are constant. The early stage of the extrapolation methods applies the simplest technique. It does not usually allow for the growth and decay of the rainfall intensities or nonlinear motion of the rainfall band. The main disadvantage of this technique is that because of its simplicity, the forecast accuracy decreases rapidly within an hour (Bellon and Austin, 1984, Wilson *et al*., 1998). In a study of the improvement of forecasts accuracy, elaborate nonlinear extrapolation schemes only give negligible improvement or even worse results than the linear extrapolation (Smith and Austin, 2000).

Many hydrologists and meteorologists have conducted vast research effort over several decades allowing for the introduction of many new schemes. These new schemes include mathematical and stochastic models integrated with a meteorological component (e.g. Geogakakos and Bras, 1984; Nakakita *et al*., 1996) and hybrid models, which are a combination of Numerical Weather Prediction (NWP) and image

extrapolation models (e.g. Golding, 2000; Ganguly and Bras, 2003). In addition, there have been complex statistical approaches such as using fractal generation algorithms (Lovejoy and Schertzer, 1986) and artificial neural networks (Grecu and Krajewski, 2000). However, even though the vast research efforts, it has still proven hard to find a notable improvement of forecast accuracy.

The extrapolation techniques are yet in the main stream for nowcasting, as many studies are taking place in order to develop more accurate extrapolation models (*e.g.* Kawamura *et al.*, 1997; Georgakakos, 2000; Grecu and Krajewski, 2000). Although there are many NWP models, the model still has insufficient spatial and time resolution to represent the detail distribution of precipitation, and furthermore, it requires sophisticated data, which in many cases is not available (Golding, 2000). For this reason, the radar image extrapolation is very powerful nowcasting tool in many practical flood forecasting situations as will be discussed in this study.

2.2 Nowcasting Using Radar Image Extrapolation

2.2.1 Introduction of the Translation Model

The Translation model by Shiiba *et al*., (1984) is used in this study for deterministic predictions of short-term radar rainfall. In this model, the horizontal rainfall intensity distribution, z(x,y,t) with the spatial coordinate (x,y) at time t is defined as:

$$\frac{\partial z}{\partial t} + \frac{\partial z}{\partial x} + v\frac{\partial z}{\partial y} = w \tag{2.4}$$

$$u = \frac{dx}{dt}, \quad v = \frac{dy}{dt}, \quad w = \frac{dz}{dt}$$

where u and v are advection velocity along x and y, respectively, and w is rainfall growth-decay rate along time. Among other similar discrete equations for the rainfall

intensity distribution, characteristics of the translation model are on the vector *u*, *v*, and *w* formation, which are specified on each grid in the manner of:

$$
\begin{aligned}
u(x,y) &= c_1 x + c_2 y + c_3 \\
v(x,y) &= c_4 x + c_5 y + c_6 \\
w(x,y) &= c_7 x + c_8 y + c_9
\end{aligned}
\tag{2.5}
$$

so that the advection velocities can express the patterns of the non-uniform movement of rainfall, such as rotation and sheer strain (Takasao *et al*., 1994). In order to optimize the parameters c_1~c_9 using observed radar rainfall data, the equation 2.5 is approximated by the central difference scheme on the rectangular horizontal area with $\Delta x \times \Delta y$ grid size and Δt time resolution.

$$
\begin{aligned}
x_i &= (i - \frac{1}{2})\Delta x\,, \quad i = 1, \cdots, M \\
y_i &= (j - \frac{1}{2})\Delta y\,, \quad j = 1, \cdots, N \\
t_k &= k\Delta t\,, \quad k = -(K-1), \cdots, 0
\end{aligned}
\tag{2.6}
$$

Here, *M* and *N* are the number of grid along the *x* and *y*-axis, respectively, and *K* is the number of rainfall slides for the optimization. The parameters c_1~c_9 are sequentially optimized using the square root information filter in a manner of minimizing

$$
J_c = \sum_{k=-K}^{-1} \sum_{i=2}^{M-1} \sum_{j=2}^{N-1} v_{ijk}^2 \tag{2.7}
$$

where

$$
v_{ijk} = \left[\frac{\Delta z}{\Delta t}\right]_{ijk} + (c_1 x_i + c_2 y_j + c_3)\left[\frac{\Delta z}{\Delta x}\right]_{ijk} + (c_4 x_i + c_5 y_j + c_6)\left[\frac{\Delta z}{\Delta y}\right]_{ijk} - (c_7 x_i + c_8 y_j + c_9)
$$

The translation model provides expected rainfall movements under the assumption that the vectors *u* and *v* are time invariant for the next several hours and that there is no

growth-decay of rainfall intensities during that time. In this research, three consecutive observed rainfall fields, which have a resolution of 3 km and 5 min, are used to determine u and v. When forecasting rainfall fields, the u and v are assumed spatially uniform and updated every 5 min, although the rainfall movement would have spatially invariant movements in a real environment. Most of heavy rainfall in Japan, which occurs during the rainy and typhoon season, have a frontal rain band over a wide area, and therefore the movement of the rainfall band can be reviewed as a spatially uniform within a single radar range.

2.2.2 Forecasting Behavior of the Translation Model

Radar data used for testing the translation model is observed at the Miyama radar station located in the central part of Kinki district, Japan (Figure 2.1). The observation field of the radar includes all spaces within a radius of 120 km and a height of 15 km (more details of the radar station can be found in Nakakita *et al*., 1990). It takes 5 minutes to scan over the entire observation field and therefore produce rainfall reflectivity data every 5 min.

The reflectivity data is converted to rainfall intensity of a 3 km spatial resolution by the Z-R relationship, $Z=200R^{1.6}$ according to Marshall and Palmer (1948). During the conversion, basic correction for ground clutters and shadow effects are carried out. The converted rainfall intensities, called observed rainfall field in this study is believed to be the true rainfall value and are the targets of the accuracy improvements of prediction fields.

Two representative rainfall events have been selected for this study. Those events are of a typical frontal rain bands type, which occurred during the rainy season (Jun and July) and the typhoon season (August and September) in Japan. As shown in Table 2.2, one event that took place in August 1992 had severe rainfall intensity with fast movement velocity compared to the second event. The event of June 1993 had a rather steady and slowly moving rainfall band.

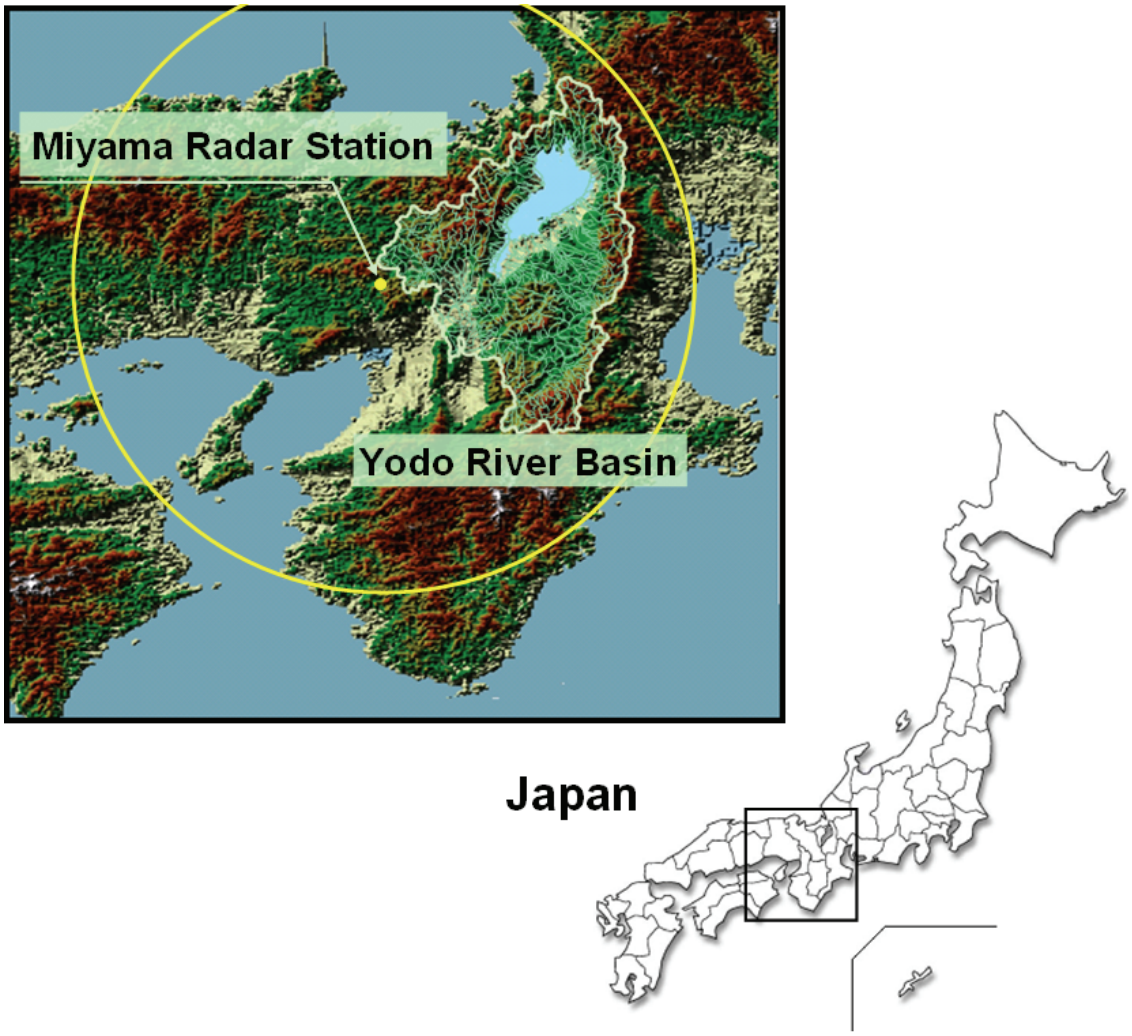

Figure 2.1 Miyama radar station and its covering area of 120 km radius.

Table 2.2 Radar data and its characteristics.

	Duration	Type
August 1992 Event	92/8/18~19	Typhoon season (Frontal)
June 1993 Event	93/6/30~31	Rainy season (Frontal)

Figure 2.2 shows spatially averaged rainfall intensities of the August 1992 Event and its covering area ratio by rainfall intensities. As previously shown, high rainfall intensities (for example an intensity over 10 mm/hr) normally have a 10 % ratio of the whole rainfall area, meaning that the most rainfall area is covered by very low rainfall intensities. This is a typical pattern of frontal rainfall band in Japan. The same characteristics can be found in the June 1993 Event shown in Figure 2.3.

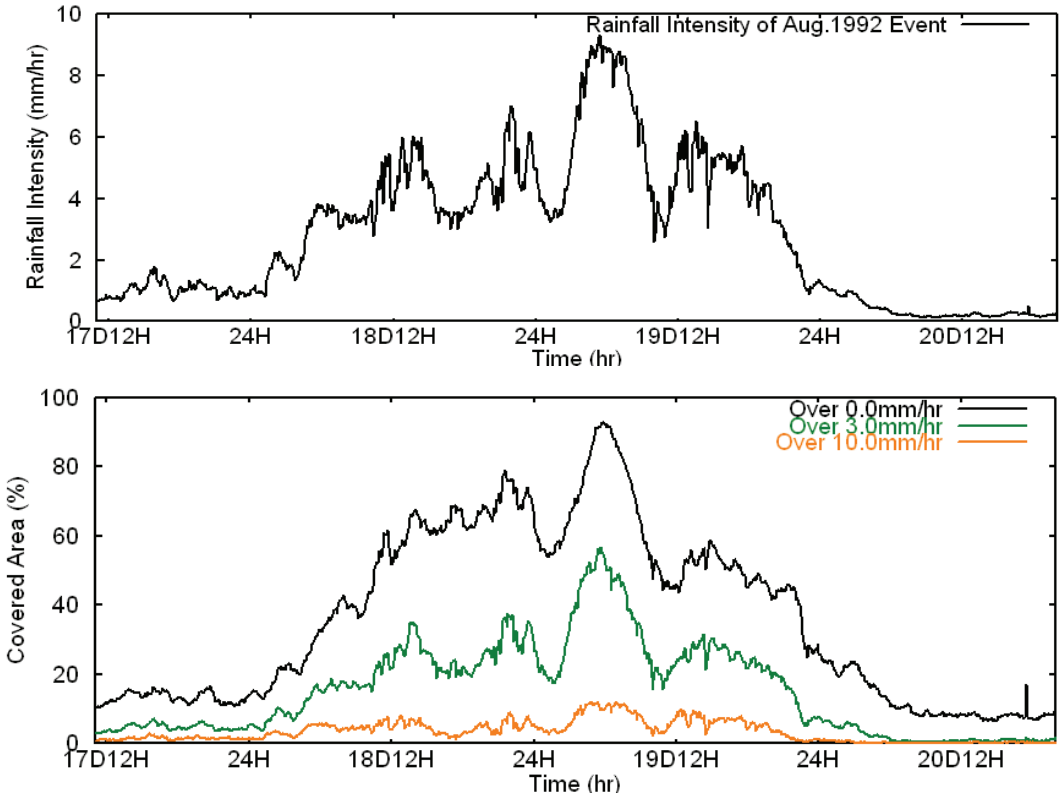

Figure 2.2 Rainfall Intensity Variations of August 1992 Event.

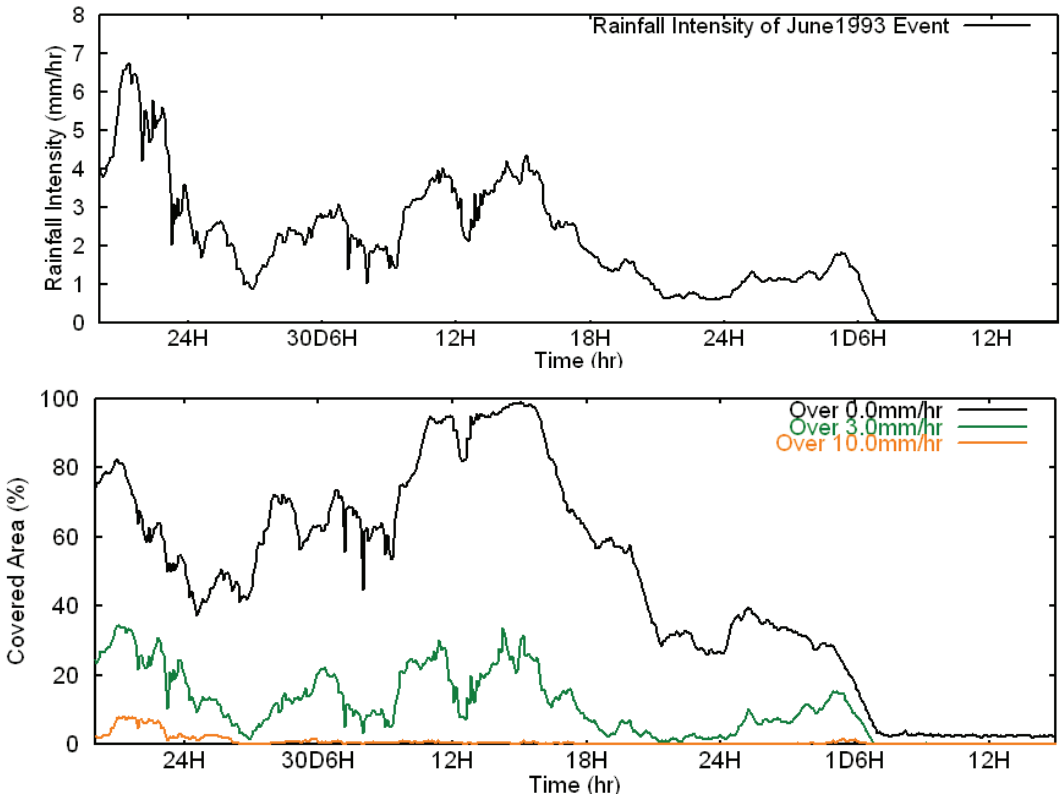

Figure 2.3 Rainfall Intensity Variations of June 1993 Event.

Both figure 2.4 and 2.5 show the characteristics of forecasted rainfall by the translation model. First of all, Figures 2.4 (a) and 2.5 (a) show the spatially averaged rainfall intensities of observation and each predictions with the August 1992 Event and June 1993 Event. In order to prevent outside influence by sizes and shapes of rainfall band, the intensity calculation includes every grid within the radar observation domain. Note that there are overall delays of rainfall intensities, as prediction time elongates. Because the translation model only represents the movement of the rainfall bands without their growth or decay, the model assumes the same amount of current rainfall intensities lasts until the prediction target time.

In Figures 2.4 (b) and 2.5 (b), correlation coefficients of the two events' observation and predictions are shown. The majority of the time for both events, correlation coefficients is under 0.5, which is a rather low value. As it can be expected, the coefficients with short lead-time have higher values compared to longer lead-time predictions. In the case of 180 min prediction of in the August 1992 Event, the most of the coefficients were less than 0.2. On the other hand, the June 1993 Event shows irregular variations of the coefficients values. After checking the variant forecasting results from other events, this kind of behavior is rather arbitrarily and does not follow a certain pattern.

Another method used to measure prediction accuracy is the Critical Success Index (CSI), which is given as:

$$CSI(\%) = \frac{X}{X+Y+Z} \times 100 \tag{2.8}$$

where X is the number of correct forecasts rainfall cells (*i.e.* rainfall is observed and also predicted in the grid), Y is the number of misses (*i.e.* rainfall is observed, but not predicted), and Z is the number of false alarms (*i.e.* rainfall is predicted, but not observed). The CSI is especially appropriate as a summary measure of forecasting for the case of extreme events, since the index value decreases when both the number of misses and false alarms increases (Smith and Austin, 2000). A threshold rain-rate for the CC and CSI is over 0.0 mm/hr in this study.

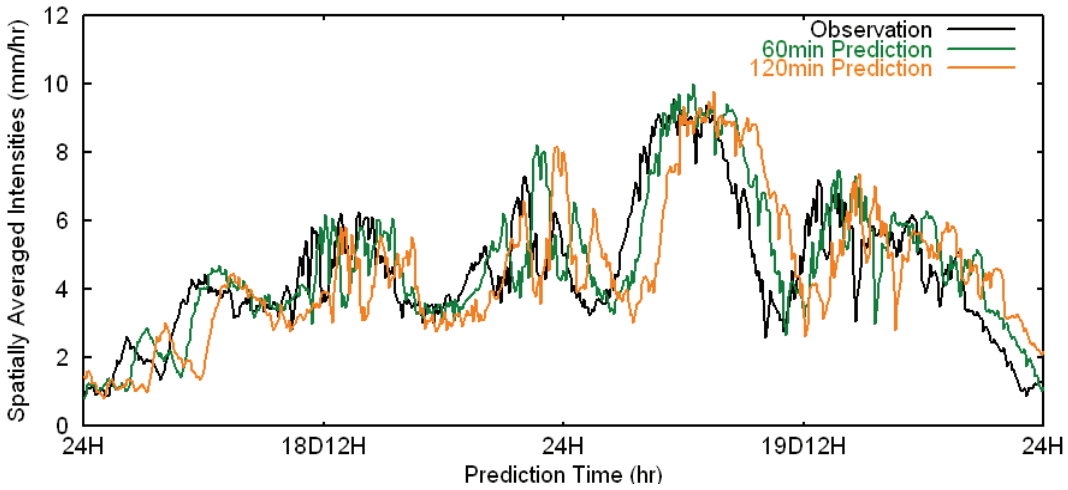

(a) Spatially averaged intensity of observed and predicted rainfall

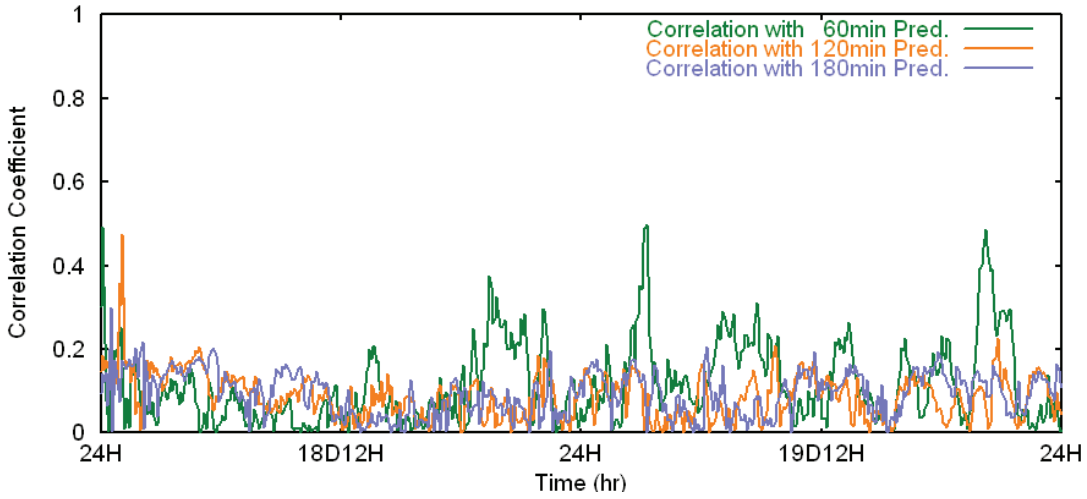

(b) Correlation coefficient of each prediction with observation

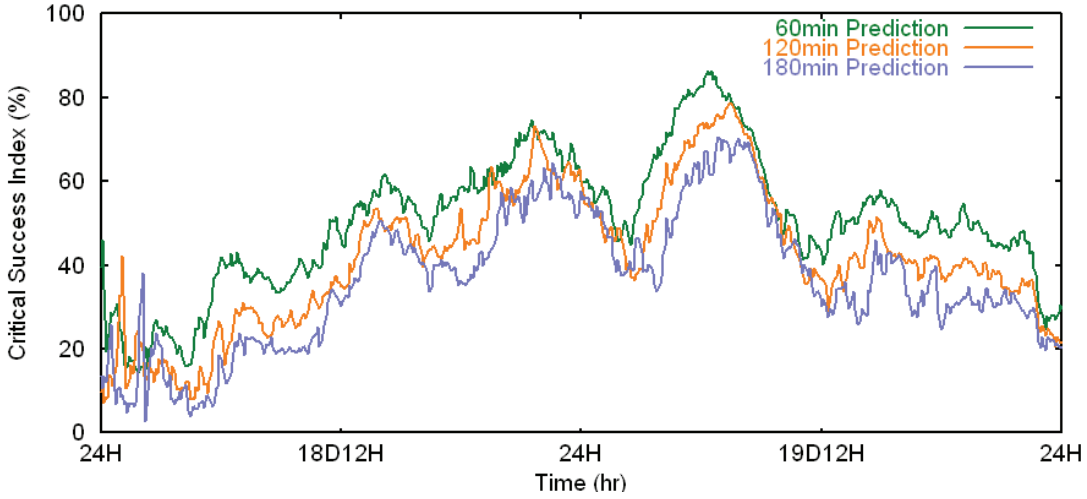

(c) Critical success index of each prediction to the observation

Figure 2.4 Prediction results and its performance index for August 1992 Event.

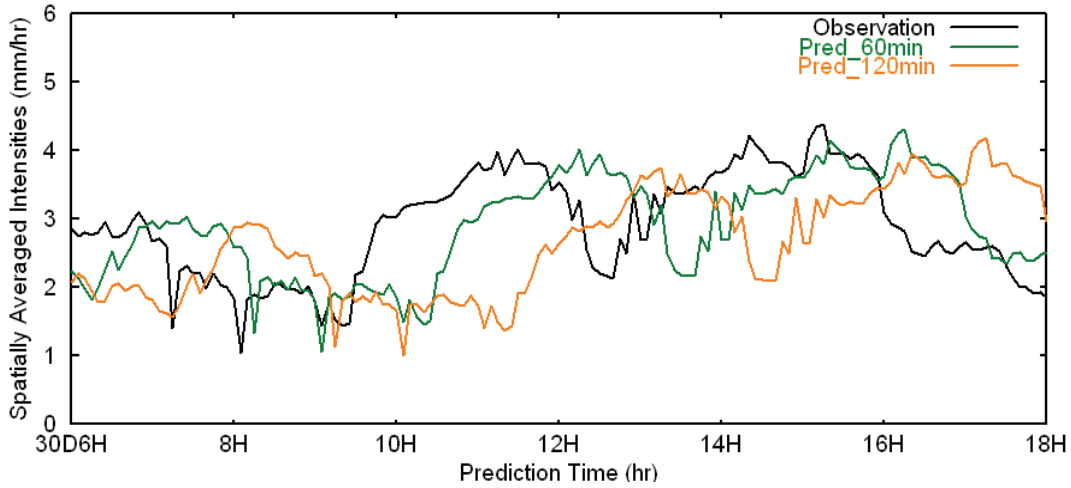

(a) Spatially averaged intensity of observed and predicted rainfall

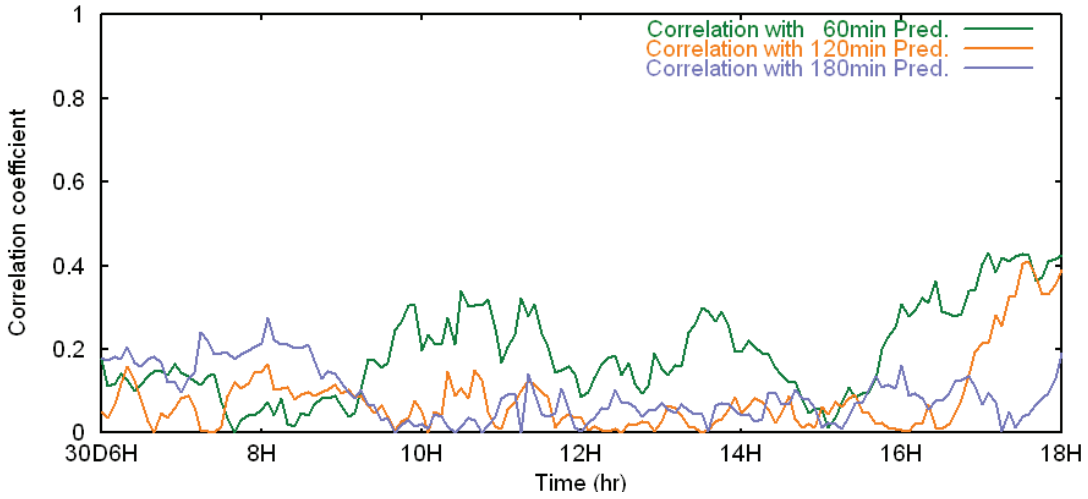

(b) Correlation coefficient of each prediction with observation

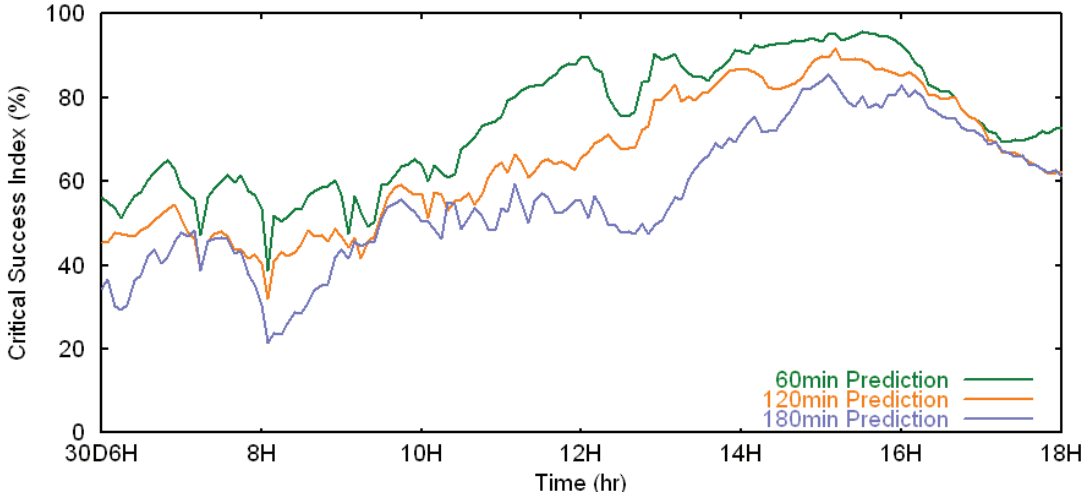

(c) Critical success index of each prediction to the observation

Figure 2.5 Prediction results and its performance index for June 1993 Event.

where X is the number of correct forecasts rainfall cells (*i.e.* rainfall is observed and also predicted in the grid), Y is the number of misses (*i.e.* rainfall is observed, but not predicted), and Z is the number of false alarms (*i.e.* rainfall is predicted, but not observed). The CSI is especially appropriate as a summary measure of forecasting for the case of extreme events, since the index value decreases when both the number of misses and false alarms increases (Smith and Austin, 2000). A threshold rain-rate for the CC and CSI is over 0.0 mm/hr in this study.

The CSI show rather high values in most prediction times even for the 180 min prediction (see Figures 2.4 (c) and 2.5 (c)). In the figures, the index clearly shows that shorter lead-time predictions have higher prediction accuracy compared to longer lead-time. The index appeared to have a positive relationship to the covering area of rainfall bands. It is rather reasonable phenomena since the index can be simply regarded as an overlap ratio of the prediction rainfall band to the observed band. If the area of rain bands is wide (or narrow), there would be higher (or lower) possibility to overlap the area with the predicted rainfall bands. Because of this characteristic of the CSI index, widespread frontal rainfall bands can give relatively higher values compare to the convective rainfall bands.

2.3 Prediction Error Structure Analysis

Tachikawa *et al*. (2003) statistically analyzed the characteristics of absolute prediction error and relative prediction error and defined them as shown in Equations 2.9 and 2.10.

$$E_{a,i} = R_{o,i} - R_{p,i} \tag{2.9}$$

$$E_{r,i} = (R_{o,i} - R_{p,i}) / R_{p,i} \tag{2.10}$$

The absolute prediction error $E_{a,i}$ on a certain grid i is calculated from the difference between predicted rainfall $R_{p,i}$ and observed rainfall $R_{o,i}$ on the grid, while the relative prediction error $E_{r,i}$ is the ratio of the absolute prediction error to its predicted rainfall.

Tachikawa *et al*. (2003) examined the timely accumulated error values with variant spatial resolutions and found that the distributions of absolute and relative error are respectively close to normal distribution and lognormal distribution.

This study concentrates on the absolute prediction error $E_{a,i}$ and simulates the spatially correlated possible error for future prediction target times on a real-time basis. Basic statistics of the prediction error examined in this study includes the mean and standard deviation as well as probability distribution of the error, which indicates normal distribution allowing a slight variation in each event and prediction case.

Figures 2.6 and 2.7 show basic statistics of the prediction error. It includes the mean, standard deviation, and spatial correlation coefficients of the error. During the August 1992 Event, the variation of mean and standard deviation values along the time-axis is rather drastic compared to the values of the June 1993 Event. This is because of higher rainfall intensity as well as its spatial variation of the August 1992 Event. However, the values are not significantly different between the variant prediction lead-times.

The Spatial Correlation Coefficients (SCC) of the absolute prediction error, which shows how much the error is spatially correlated to each other, are shown in Figures 2.6 (c) and 2.7 (c). The SCC is calculated for every increment of time by grouping every pair of the absolute error values, which is one grid apart for 3 km, two grids for 6 km, etc., on each error field. The SCC shows high values for close distances and decreases as the distance gets longer. It is found that the absolute error from longer prediction times has higher SCC values, and is diminished to approximately 15 km in most prediction cases. In addition, higher prediction error (the August 1992 Event) gives higher spatial correlation as shown in Figure 2.6 (c).

For the purpose of reviewing the spatial pattern of the prediction error, the absolute errors on each grid are accumulated event by event. For example, if there is a certain spatial and/or time pattern in the prediction error, because of perpetual overestimation or underestimation on a certain area during a certain event, the accumulated error will present those patterns. Otherwise, if the error does not have any spatiotemporal pattern

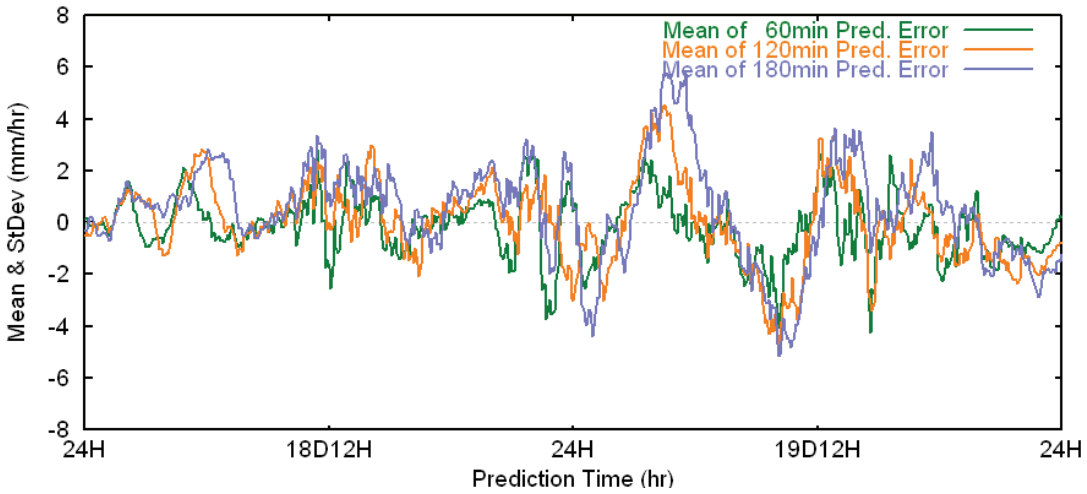

(a) Mean values of prediction error

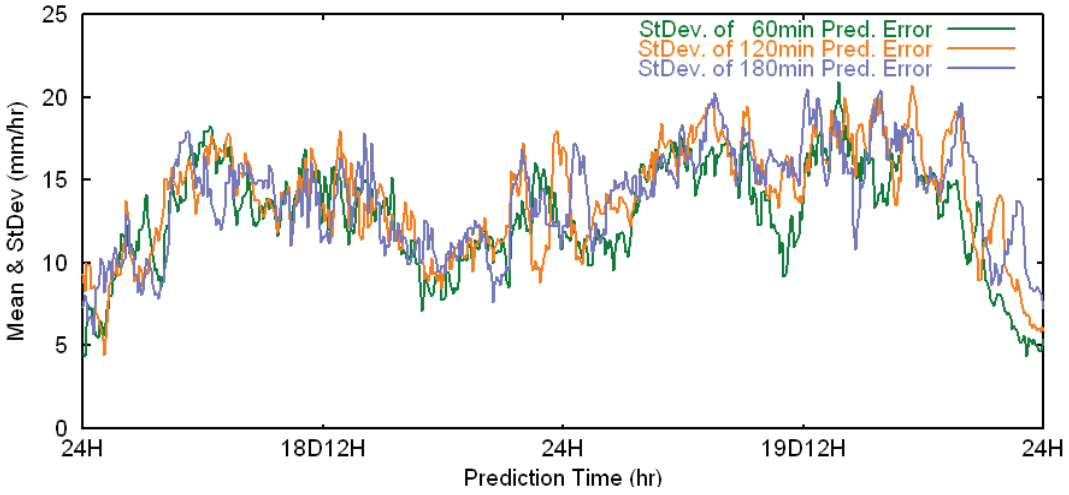

(b) Standard deviations of prediction error

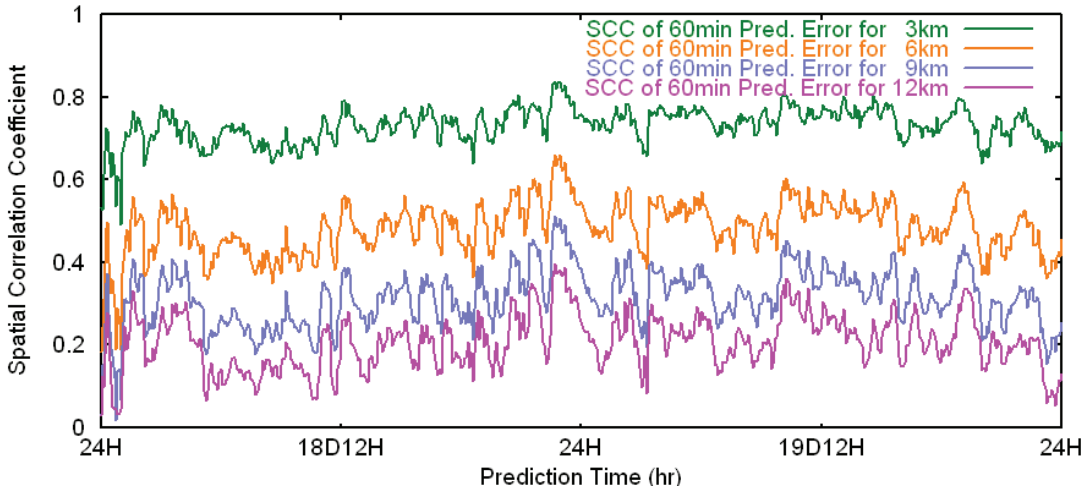

(c) Spatial correlation coefficients of prediction error

Figure 2.6 Prediction error characteristics of August 1992 Event.

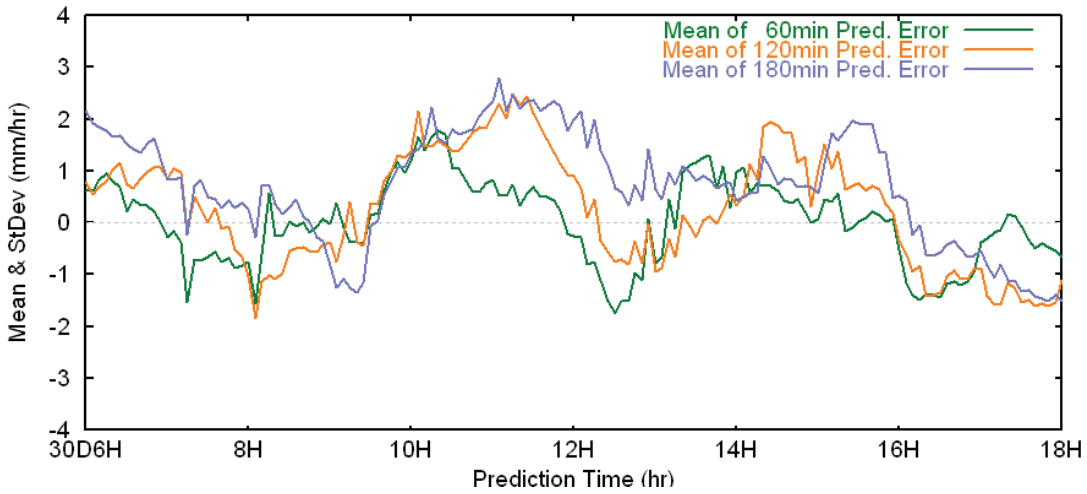

(a) Mean values of prediction error

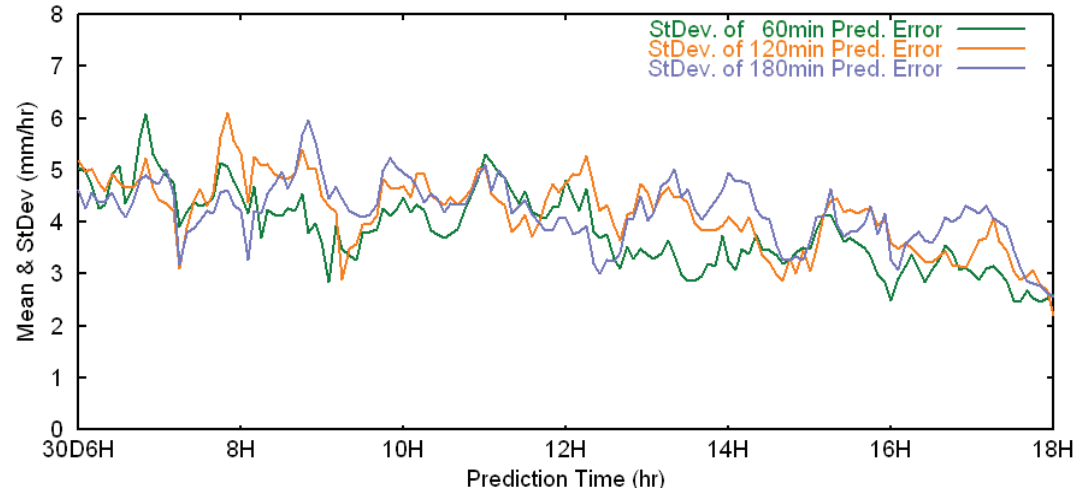

(b) Standard deviations of prediction error

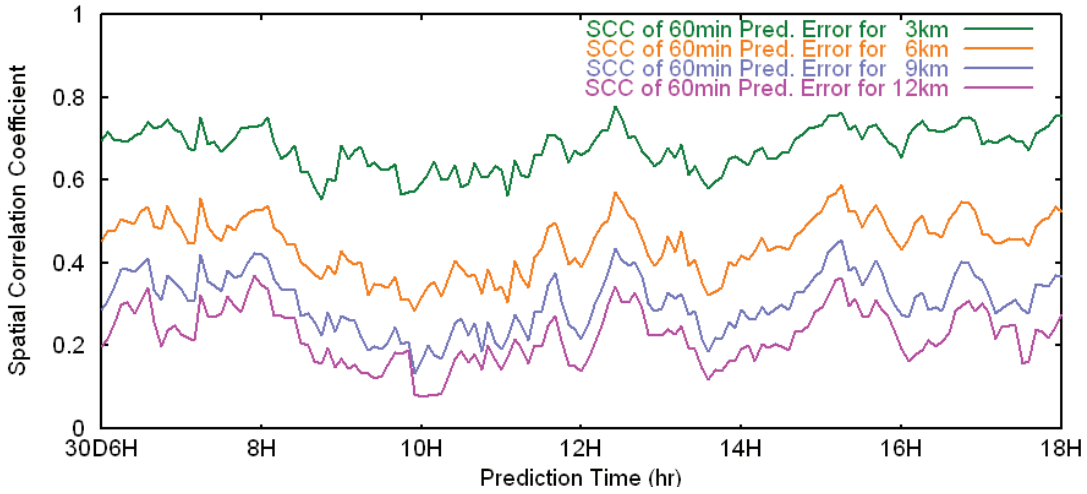

(c) Spatial correlation coefficients of prediction error

Figure 2.7 Prediction error characteristics of June 1993 Event.

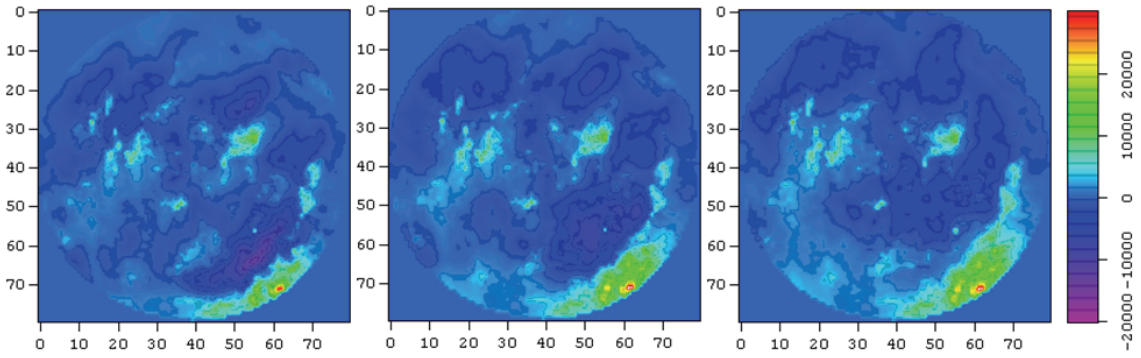

(a) 60min (left), 120min (middle) and 180min (right) prediction of August 1992 Event

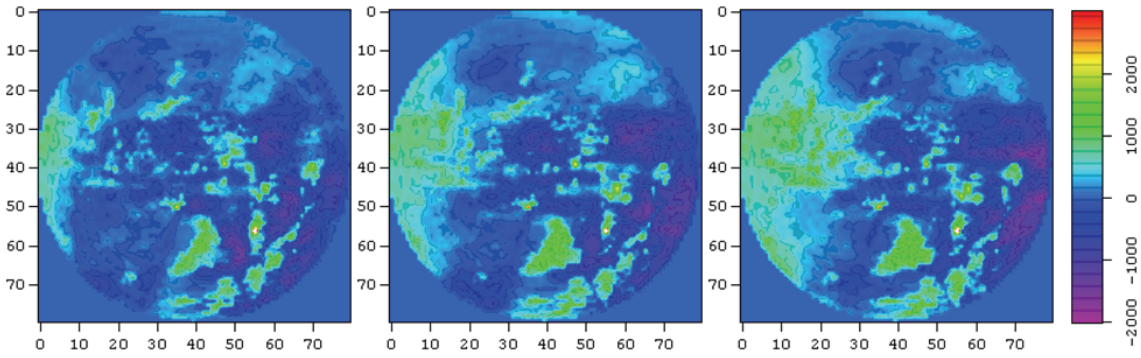

(b) 60min (left), 120min (middle) and 180min (right) prediction of June1993 Event

Figure 2.8 Accumulation of the prediction error during each event (unit: mm/hr).

namely arbitrarily random errors, the accumulated prediction error on every grid would compensate each other. As shown in Figure 2.8, there is a specific spatial pattern on each accumulation of prediction error. Another interesting point is that although each individual event depicts similar patterns within themselves, separately they remain quite distinct.

To forecast precipitation accurately hydrologists and meteorologists need to understand not only the rain band movement but also the generation, growth, and decay of rain cells. As mentioned earlier, the translation model ignores the growth-decay of rainfall intensities, and has inherent error sources related to this growth-decay rate. Many studies say that the rainfall generation and its amount are highly correlated to topographic patterns, but the relationships between precipitation and topography in mountainous areas continue to be vague due to the complexity of the topography of

those regions (Prudhomme and Reed, 1998). In addition, studies of precipitation pattern adjustments to topography are often based on annual precipitation. However, not only the effects of topography and its relation to precipitation can be vary with each event, but also the wind direction against mountains and wind speed are important factors in such cases (Johansson and Chen, 2003). From this point of view, it can be considered that different wind direction gives different spatial patterns of the prediction error. In the instances of the June 1993 and August 1992 Event, the main wind direction was West and South-East, respectively.

However, more detailed study is required in order to calculate the particular effects of topography on the prediction error patterns. The error would have a complex relationship with topography as well as meteorological conditions of each event, and it is difficult to define the error beforehand. Be that as it may, the information of spatially variant prediction error patterns can be used in real-time forecasts of precipitation, which is presented and discussed in the next section. In the next section, a method to obtain a spatially variant error pattern on a real-time basis is proposed and it is used for stochastic prediction in this study.

References

Bellon, A. and Austin G. L. (1984): The accuracy of short-term radar rainfall forecasts, J. Hydrol., Vol.70, pp. 35-49.

Collier, C. G. and Kzyzysztofowicz, R. (2000): Preface: Quantitative precipitation forecasting. J. Hydrol., Vol.239, pp. 1-2.

Einfalt, T., Arnbjerg-Nielsen, K., Golz, C., Jensen, N., Quirmbach, M., Vaes, G. and Vieux, B. (2004): Towards a roadmap for use of radar rainfall data in urban drainage, Journal of Hydrology, Vol. 299, pp. 186-202.

Fox, N. I. and Wilson, J. W. (2005): Very short period quantative precipitation forecasting, Atmos. Science Letters, Wiley Interscience, Vol.6, pp. 7-11.

Ganguly, A. R. and Bras R. L. (2003): Distributed quantitative precipitation forecasting using information from radar and numerical weather prediction models, J. Hydrometeorol., Am. Meteor. Soc., Vol.4, pp. 1168-1180.

Georgakakos, K. P. and Bras, R. L. (1984): A hydrologically useful station precipitation model: 1.Formulation, Water Resour. Res., Vol. 20, No. 11, pp. 1585-1596.

Georgakakos, K. P. (2000): Covariance propagation and updating in the context of real-time radar data assimilation by quantitative precipitation forecast models, Journal of Hydrology, Vol. 239, pp. 115-129.

Golding, B. W. (2000): Quantitative precipitation forecasting in the UK, J. Hydrol., Vol.239, pp. 286-305.

Grecu, M. and Krajewski, W. F. (2000): A large-sample investigation of statistical procedures for radar-based short-term quantitative precipitation forecasting, J. Hydrol., Vol.239, pp. 69-84.

Johansson, B. and Chen, D. (2003): The influence of wind and topography on precipitation distribution in Sweden: statistical analysis and modeling, Int. J. Climatol., Vol. 23, pp. 1523-1535.

Kawamura, A., Jinno, K., Berndtsson, R. and Furukawa, T. (1997): Real-time tracking of convective rainfall properties using a two-dimensional advection-diffusion model, Journal of Hydrology, Vol. 203, pp. 109-118.

Kim, S., Tachikawa, Y. and Takara, K. (2005): Rainfall-runoff prediction considering error structure of the predicted rainfall, Annuals of DPRI, Kyoto University, No. 48B, pp. 53-58.

Kim, S., Tachikawa, Y. and Takara, K. (2006): Ensemble rainfall-runoff prediction with radar image extrapolation and its error structure, Annual of Hydraulic Engineering, JSCE, Vol. 50, pp. 43-48.

Lovejoy, S. and Schertzer, D. (1986): Scale invariance, symmetries fractals and stochastic simulations of the atmosphere, Bull. Am. Meteor. Soc., Vol. 67, pp. 21-32.

Marshall, J. S. and Palmer, W. M. (1948): The distribution of raindrops with size, J. Meteorol., Vol. 5, pp. 165-166.

Nakakita, E., Ikebuchi, S., Shiiba, M., and Takasao, T. (1990): Advanced use into rainfall prediction of three-dimensionally scanning radar, Stochastic Hydrol. Hydraul., Vol. 4, pp. 135-150.

Nakakita E., Ikebuchi, S., Nakamura, T., Kanmuri, M., Okuda, M., Yamaji, A., and Takasao, T. (1996): Short-term rainfall prediction method using a volume scanning radar and grid point value data from numerical weather prediction, J. Geophys. Res., Vol.101, No. D21, pp. 26181- 26197.

Prudhomme, C. and Reed, D. W. (1998): Relationships between extreme daily precipitation and topography in a mountainous region: a case study in Scotland, Int. J. Climatol., Vol. 18, pp. 1439-1453.

Shiiba, M., Takasao, T. and Nakakita, E. (1984): Investigation of short-term rainfall prediction method by a translation model, Jpn. Conf. on Hydraul., 28th, pp. 423-428.

Smith, K. T. and Austin, G. L. (2000): Nowcasting precipitation-a proposal for a way forward, J. Hydrol., Vol.239, pp. 34-45.

Takasao, T., Shiiba, M. and Nakakita, H. (1994): A real-time estimation of the accuracy of short-term rainfall prediction using radar, Stochastic and Statistical Methods in Hydrol. and Environm. Eng., Vol.2, pp. 339-351.

Tachikawa, Y., Komatsu, Y., Takara, K. and Shiiba, M. (2003): Stochastic modeling of the error structure of real-time predicted rainfall and rainfall field generation, Weather Radar Information and Distributed Hydrological Modelling (ed. by Y. Tachikawa, B. E. Vieux, K. P. Georgakakos & E. Nakakita), IAHS Publ., No. 282, pp 66-74.

Wilson, J. W., Crook, N. A., Mueller, C. K., Sun, J. and Dixon, M. (1998): Nowcasting thunderstorms: A status report, Bull. Am. Meteor. Soc., Vol. 79, No. 10, pp. 2079-2099.

Wilson, J. W. and Brandes, E. A. (1979): Radar measurement of rainfall-A summary, Bull. Am. Meteor. Soc., Vol. 60, No. 9, pp. 1048-1058.

Chapter 3

Ensemble Flood Forecasting with Prediction Error Fields

> "In the course of the statistical hydrodynamical studies of the predictability problem, it has become clear that single numerical forecasts do not provide the best estimate of the true state of the atmosphere in the classical least mean square sense." (Leith, 1974)

NWP models have been run in 'ensemble mode' for the last decade or so, and statistical outcome has been obtained from the ensemble simulations by adopting small perturbations in the initial values and initial condition (*e.g.* Du and Mullen, 1997). The ensemble forecast of hydrographs is also a recent trend away from the conventional simple deterministic forecasts of hydrographs and towards probabilistic forecasts, which include prediction uncertainty (see Krzysztofowicz, 2001). However, most of the ensemble simulations in the early stages are concerned only with the internal growth of error rising from the difference in initial conditions (Leith, 1974). In considering the external growth of prediction error rising from an imperfect model structure, continuous corrections of model states or additional error simulation models are necessary. More specifically, to fill the shortage of the current ensemble techniques, real-time correction of forecasting results using the most updated observation should be brought into mind.

As a step towards addressing the improvement of forecast accuracy and ensemble forecasting with consideration of external error, this chapter introduces a new attempt of ensemble rainfall forecasting using a stochastic error field simulation. As apposed to the traditional ensemble simulation method that uses initial condition control to obtain statistical outcome, the error model independently offers stochastic error fields to the deterministic prediction results. The characteristics of the error fields are based on an analyzed error structure of the current rainfall prediction, and are simulated using the random field generation method.

The simulated error fields, responsible for successfully keep the analyzed error structure, not only give probable rainfall field variations for the ensemble simulation but also improve the accuracy of the deterministic prediction by correcting the possible prediction error (Kim *et al.*, 2006). Then, stochastically extended prediction fields are given to a distributed hydrologic model to achieve ensemble runoff predictions.

3.1 Stochastic Forecasting by an Ensemble Mode

In atmospheric modeling, stochastic dynamic forecast was introduced more than three decades ago (Epstein, 1969). Until now, the main purpose of ensemble forecasting in those models was to consider the uncertainty of initial conditions and boundary conditions at the start of forecasting. After Lorenz (1963) found that only slightly variant initial conditions yield quite different results in a numerical weather prediction model, small perturbations of the initial condition in the beginning of a model simulation were used as a trigger for ensemble forecasting. One good example of short-range ensemble forecasting of precipitation with well-documented review can be found in Du and Mullen (1997).

Most ensemble simulations in early stages are primarily concerned with the internal growth of error rising from the difference in initial conditions and ignore the external growth of error rising from the difference between a numerical model and the real atmosphere (Leith, 1974). Until now, ensemble simulations for probabilistic forecasting had been criticized for its underestimation of the total uncertainty as not all sources of uncertainty are accounted for in the ensemble generator (Krysztofowicz, 2001). Because the model conducting the simulation cannot be perfect, there is always a chance that the initiated variant initial conditions for an ensemble simulation have resulted in different forecast projections (Fig. 3.1).

Figure 3.1 presents schematic drawings of ensemble forecasting, plotted in terms of an idealized two-dimensional phase space. The first circles at initial time *t* represent initial states for ensemble forecasting, and the dot stands for the best prediction or the best

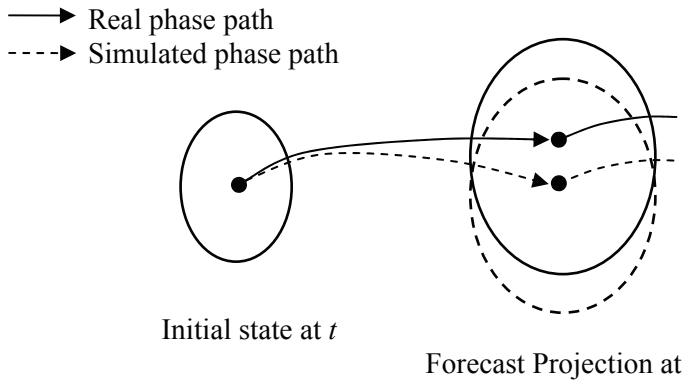

(a) Forecasted result from a model generates a shifted projection to the real projection

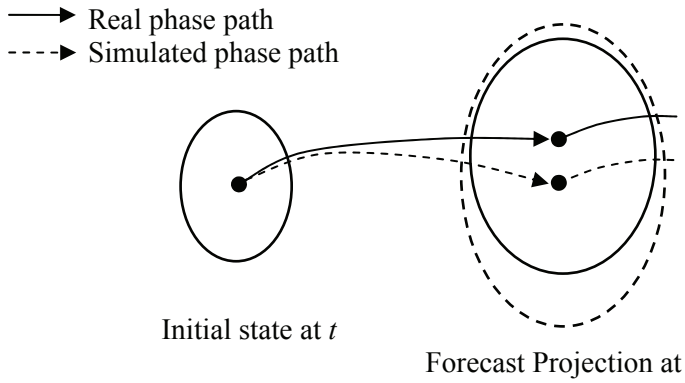

(b) Forecasted result from a model generates a diverged projection to the real projection.

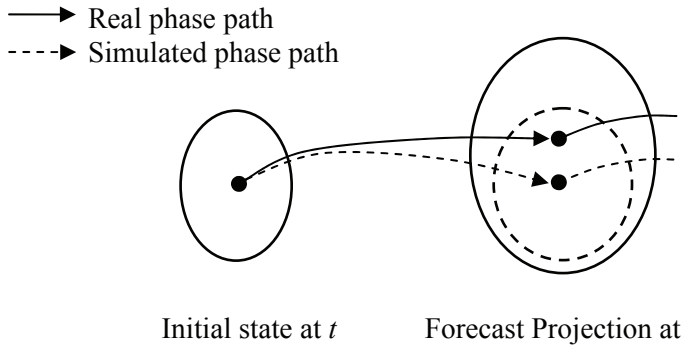

(c) Forecasted result from a model generates a localized projection to the real one.

Figure 3.1 Three different cases of forecast projection caused by variant conditions.

observation at the beginning of the simulation. The solid line represents the phase path of the states by processes in a real environment, and the dashed line represents the phase path of model simulations. Because of the imperfection of the model, the forecast projection (dashed line circle) has shifted from the real projection (solid line circle) as shown in Figure 3.1 (a). In other cases, the forecast projection can have a diverged state space (Figure 3.1 (b)) or can converge into a limited space area (Figure 3.1 (c)). These three cases can occur depending on whether different models are running or whether there are different situations in a one-model simulation. In any case, as forecasting continues for longer prediction time, noted as $t+ndt$, the shift or divergence of the simulation results makes a much bigger discrepancy in the real phenomena.

If any model shows one specific pattern of discrepancy that is recognizable, the model structure should be corrected for an improvement of forecasting behavior. If any model shows a different discrepancy pattern with different simulation times or conditions, which is more common in model simulations, the different forecast projection should be corrected by updating the model state vectors through means of most recent observations. Such real-time updating can be fulfilled by adopting a data assimilation method, for instance the Kalman filter (Kim *et al.*, 2005), or an additional error simulation model (Kim *et al.*, 2006).

3.2 Prediction Error Field Simulation Algorithm

3.2.1 Overview of the Algorithm

The main purpose of the algorithm is to simulate possible error fields after current time, t, using the current prediction error structure. This is conducted under the assumption that a temporal persistence of the error characteristics from the current time to the prediction target time exists. The proposed scheme uses a certain duration of prediction error data for the simulation of future prediction error as shown in Figure 3.2. In the figure, the observed rainfall fields, the previous prediction fields, and the prediction error fields are sequentially illustrated until the current time t. Various prediction fields

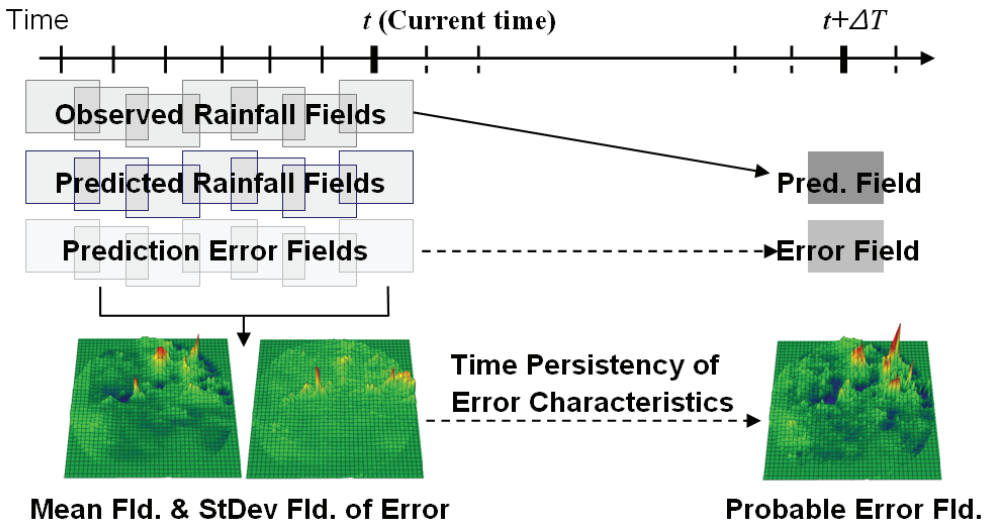

Figure 3.2 Schematic drawing of the stochastic error field simulation.

of each time segment are followed by various prediction lead-times. However, in this case only one prediction with the lead-time Δt is considered in the figure. Again, every prediction field at each time increment is the prediction results that are carried at Δt time before that time increment. At the current time t, the translation model carries another prediction for the time $t+\Delta t$ upon which the probable prediction error of the prediction is then simulated in accordance with the current error characteristics.

The current characteristics of the prediction error can be presented by basic probabilistic statistics under an assumption that the time series of the error on each grid follows normal probability distribution. Here, the basic statistics stand for the mean and standard deviation values of the most recent errors in certain duration, one hour for example, on each grid. Based on this procedure, the statistic fields can compromise spatial and temporal patterns of the current errors and can be updated on a real-time basis.

If the spatiotemporal characteristics of the prediction error lasts for a couple of hours, and the statistic characteristics of the error on the prediction target time $t+\Delta t$ are similar to the characteristics of the current statistic fields, the possible error fields at $t+\Delta t$ can be simulated by using the current statistic fields. The proposed algorithm is for offering a

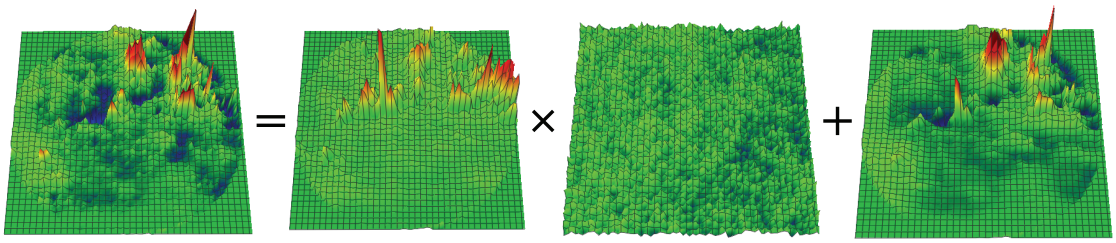

(a) Prediction error field (b) StDev field of error (c) Unit random error field (d) Mean field of error

Figure 3.3 Simulation procedure of the error field using the statistic fields and UREF.

probable variation of the deterministic extrapolation model as well as improving its forecast accuracy. This assumption, the temporal persistency of the error characteristics is evaluated in the next section.

Figure 3.3 explains the procedure for the simulation of the possible error field. The statistic field, the mean and standard deviation field of error (see Fig. 3.3(b) and (d)), contains the current characteristics of the prediction error. The statistic field therefore converts the Unit Random Error Field (UREF; Fig. 3.3(c)) to the target error field (Fig. 3.3(a)), which is the aim of the error field simulation.

The UREF is a set of random values, which are spatially correlated and follow normal distribution of $N(0,1)$. The spatial correlation for the UREF is determined by spatial correlation of the current error fields. A matrix decomposition method is used for a simulation of UREF in this study. Through numerous generations of the UREF it becomes possible to acquire many prospective error fields for the prediction target time.

Finally, the deterministic prediction field obtained by the translation model is extended to many prospective prediction fields by combining them with the simulated prediction error fields.

3.2.2 Time Persistency of the Error Characteristics

To confirm the temporal persistence of the characteristics of prediction error, this study has adopted modified CSI (MCSI) as Equation 3.1. The MCSI uses the same form of CSI, shown in Equation 2.8, with the exception of range concept. As noted in the

previous section, the statistic fields give a specific probabilistic range on each grid by the mean μ and the standard deviation σ of the error on its own grid. If the real, not simulated prediction error of the target time on a certain grid is within the range between μ-σ and μ+σ on the grid, it is counted as a correct value, *X*, and if the error is out of the range, it is counted as a wrong value, *Y*.

$$MCSI(\%) = \frac{X}{X+Y} \times 100 \tag{3.1}$$

Evaluations were firstly conducted with the 60 min lead-time predictions and three different sets of statistic fields were calculated using the error fields within 10, 30, and 60 min. After each statistic fields was prepared for every time increment, the MCSI was calculated with the corresponding real prediction error field.

Figure 3.4 (a) shows the MCSI values for the 60 min lead-time predictions with three different sets of statistic fields. With focusing on the MCSI with the statistic fields of a 30 min duration, the MCSI starts with high values around 80%, and lowers as the rainfall intensity becomes stronger. When it is considered that the probability area within $\pm 1.0\sigma$ of a normal distribution is 68%, this result is highly encouraging for adopting the time persistence of the prediction error.

Compared to the MCSI from the statistic fields of 30 min duration, MCSI from the 60 min duration statistic fields has larger values whereas 10 min duration statistic fields indicate lower values. When the statistic fields of different duration were compared to each other, the mean field of error did not show different spatial patterns. However, the longer the duration of a statistic field, the larger the produced standard deviation value is; therefore the value *X* can have bigger values in MCSI. There are no specific criteria to determine what length of duration is appropriate for making the statistic fields. 10 min duration would be too short for representing the current error characteristics while a 30 min duration is long enough to represent the current characteristics. Therefore, the statistic field of 30 min duration is used for the error field simulation in the next section.

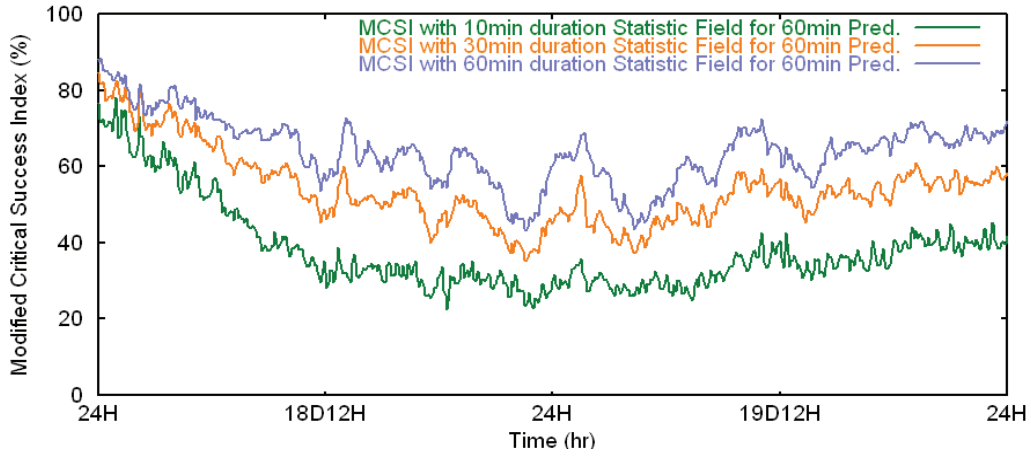

Figure 3.4 MCSI variations of 60 min prediction in August 1992 Event.

Table 3.1 and 3.2 show the time averaged MCSI values within different prediction lead-times: 60, 120 and 180 min prediction. Note that the statistic field for each prediction lead-time is derived from different prediction error fields. For example, a prediction with a 120 min lead-time generates error fields of its own lead-time whose statistic field consist of 10, 30 and 60 min durations for this prediction. As shown in both tables, the MCSI values remain approximately the same throughout each prediction lead-time. The values from the August 1992 Event are higher than the values form the June 1993 Event.

Table 3.1 Averaged MCSI values from variant prediction lead-times (August 1992 Event).

Lead-time	Error Durations for Statistic Fields		
	10 min	30 min	60 min
60 min Prediction	37.88	53.92	64.13
120 min Prediction	35.43	50.52	60.48
180 min Prediction	35.83	50.59	60.09

Table 3.2 Averaged MCSI values from variant prediction lead-times (June 1993 Event).

Lead-time	Error Durations for Statistic Fields		
	10 min	30 min	60 min
60 min Prediction	25.69	39.46	49.95
120 min Prediction	21.75	32.90	42.66
180 min Prediction	23.30	34.12	42.48

3.3 Stochastic Extension of the Deterministic Rainfall Prediction

3.3.1 Spatially Correlated Random Error Field

The UREF simulation is based on the decomposition of a matrix that includes spatial correlation characteristics of the prediction error in a covariance matrix form. The matrix is decomposed approximately into its square root matrix with the matrix factorization technique and the Chebyshev polynomials. Multiplying the square root matrix by a random vector $\boldsymbol{N}(0,1)$ gives a non-conditional simulation of the UREF (Davis, 1987; Tachikawa and Shiiba, 2000).

Davis (1987) proved a symmetric matrix B that satisfies $\mathbf{K}=\mathbf{BB}$ could be found when $\mathbf{K}$ is symmetric and positive-definite. Considering the random vector $\mathbf{Y}$ in this study, the spatially correlated unit random error vector is as follows:

$$\mathbf{Y}=\mathbf{B}\boldsymbol{w}$$

where $\boldsymbol{w}$ is the uncorrelated random vector $\boldsymbol{N}(0,1)$. The expected value of the matrix $\mathbf{YY}^{\mathrm{T}}$ (n×n) is given by

$$E[\mathbf{YY}_{\mathrm{T}}] = E[\mathbf{B}\boldsymbol{w}\boldsymbol{w}^{\mathrm{T}}\mathbf{B}^{\mathrm{T}}] = \mathbf{B}E[\boldsymbol{w}\boldsymbol{w}^{\mathrm{T}}]\ \mathbf{B}^{\mathrm{T}}$$

Because $\boldsymbol{w}$ is a vector of independent random numbers, $E[\boldsymbol{w}\boldsymbol{w}^{\mathrm{T}}] = \mathbf{I}$, thus

$$E[\mathbf{YY}^{\mathrm{T}}] = \mathbf{B}\ \mathbf{I}\ \mathbf{B}^{\mathrm{T}} = \mathbf{K}$$

The spatial correlation coefficients (SCC), which are obtained from the absolute prediction error E_{a}, makes up the covariance matrix $\mathbf{K}$ as shown in Equation 3.2. Under an assumption of ergodicty on SCC, the scc_j is prepared using two error groups, which are j grids separate from other within one error field. For example, scc_0 is the SCC with its own cell, thus scc_0 should be 1.0, and scc_1 is the SCC with the error of the next cell,

$$\mathrm{K}=\begin{bmatrix} scc_0 & scc_1 & scc_2 & \cdots & scc_n \\ scc_1 & scc_0 & scc_1 & \cdots & scc_{n-1} \\ scc_2 & scc_1 & scc_0 & \cdots & scc_{n-2} \\ \vdots & \vdots & \vdots & \ddots & \vdots \\ scc_n & scc_{n-1} & scc_{n-2} & \cdots & scc_0 \end{bmatrix} \tag{3.2}$$

which is around 0.70 in the June 1993 Event. Although it is possible to get scc_i from every prediction error field at every time increment, time averaged scc_i is used for the matrix **K** following the assumption of ergodicty.

The matrix **K** is decomposed into a symmetric matrix **B** approximately by the Chebyshev polynomials (see more details on the matrix decomposition in Davis, 1987; Tachikawa and Shiiba, 2000). Vector **Y** (or UREF), which is a non-conditional simulation of spatially correlated random vectors, can be generated continuously by multiplying the matrix B by an uncorrelated random vector $\boldsymbol{w}$. Figure 3.3 (c) shows one example of UREF.

The statistic fields convert the UREF to the prediction error fields as Equation 3.3:

$$\begin{bmatrix} E_{s,1} \\ E_{s,2} \\ E_{s,3} \\ \vdots \\ E_{s,n} \end{bmatrix} = \begin{bmatrix} sd_1 & 0 & 0 & \cdots & 0 \\ 0 & sd_2 & 0 & \cdots & 0 \\ 0 & 0 & sd_3 & \cdots & 0 \\ \vdots & \vdots & \vdots & \ddots & 0 \\ 0 & 0 & 0 & \cdots & sd_n \end{bmatrix} \begin{bmatrix} y_1 \\ y_2 \\ y_3 \\ \vdots \\ y_n \end{bmatrix} + \begin{bmatrix} m_1 \\ m_2 \\ m_3 \\ \vdots \\ m_n \end{bmatrix} \tag{3.3}$$

Here, the m_i and sd_i are the mean and standard deviation of the current prediction error on grid i. The y_i is the unit random error of the vector **Y**, and the $E_{\mathrm{s,i}}$ is the simulated error for the prediction target time. Equation 3.3 is a linear equation, thus the spatial correlation structure of **Y**, which is obtained from the E_a, is maintained in the E_s. The form of Equation 3.3 is identical with Figure 3.3. The total grid number of the Miyama radar image is 80×80, thus the n in Equation 3.3 is 6400. This procedure allows each

random error value y_i to have statistical characteristics on its own grid. Fifty sets of prediction error fields at each time increment were generated for the ensemble simulation.

3.3.2 Generation of the Extended Prediction Fields

Deterministic prediction rainfall field from the translation model are extended to many prospective prediction rainfall fields by combining them with the simulated prediction error fields in a manner of:

$$R_{e,i} = R_{p,i} + E_{s,i} \tag{3.4}$$

where $E_{s,i}$ is the simulated prediction error value on grid i, $R_{p,i}$ is the prediction from the translation model, and Re,i is the extended prediction. Because the simulated prediction error contains the error statistics of the absolute prediction error ($E_{s,i} \approx E_{a,i}$), the extended prediction can be close to the observed rainfall on the prediction target time as:

$$R_{e,i} \approx R_{o,i} = R_{p,i} + E_{a,i} \tag{3.5}$$

In other words, the properly simulated prediction error can remove the discrepancy, which would occur in the prediction target time, and therefore has the ability to improve the accuracy of the deterministic prediction.

One example of this accuracy improvement is shown in Figure 3.5. The deterministic prediction field failed to give high rainfall intensities, marked by a red circle in Figure 3.5. During a prediction of the given deterministic field, the circled area shows perpetual underestimation of rainfall for a certain duration by missing newly generated rainfall at those times. Because the underestimation lasted for several hours, this temporal and spatial characteristic of prediction error was detected and included in the simulated error fields in a stochastic way. After the deterministic field from the translation model is combined with the simulated error fields, the extended prediction

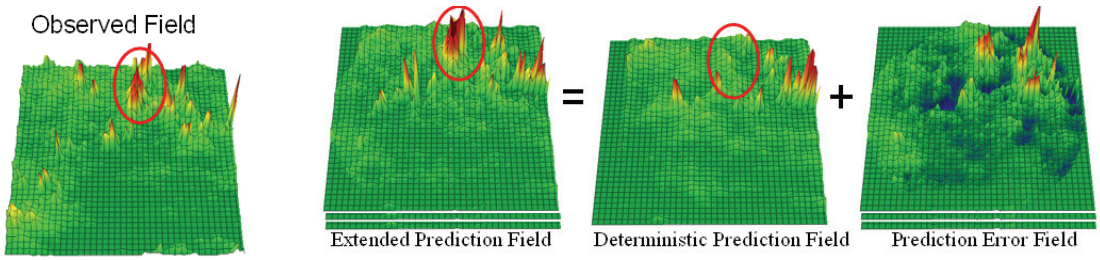

Figure 3.5 Example of bias correction by the simulated error fields.

fields can produce bias-corrected values. This mechanism gives an accuracy improvement of the extended prediction fields as well as probabilistic variability of the prediction values.

Because some values on the simulated prediction error field yield negative value that can be larger than the predicted rainfall value at that point, negative values could occur on the extended prediction field. These negative rainfall values are set to zero, and the same amount of negative values is subtracted from the positive rainfall values so as to keep the total rainfall amount as:

$$\begin{aligned} R'_{e,i} &= R_{e,i}(1+r) \quad (\text{if } R_{e,i} \geq 0.0) \\ &= 0.0 \quad (\text{if } R_{e,i} < 0.0) \end{aligned} \tag{3.6}$$

$$\text{where} \quad r = \frac{\sum MinusR_{e,i}}{\sum PlusR_{e,i}}$$

The value r stands for the ratio of the total negative rainfall amount on each extended prediction field to the total positive rainfall amount. The total amount of negative rainfall generally has 10% to 20% of the total positive rainfall amount, therefore, r varies from -0.1 to -0.2. In addition to tallying total rainfall amount, this procedure gives a smoothing effect on the extended prediction fields, so that it decrease an abnormally high prediction value caused by abnormally high random error values.

3.3.3 Evaluation of the Extended Prediction Fields

For validity of an error field simulation, the extended prediction fields should have similar error structure to the real prediction error. Furthermore, if the bias correction mentioned in the previous section works properly, the extended prediction fields should have a much closer value to the observed radar rainfall intensities.

First, spatially averaged rainfall intensities are checked as shown in Figure 3.6 (a) with the 60 min prediction case of the Event in Aug. 1992. The intensities from the extended prediction fields make a certain range and show similar patterns of intensities in the deterministic prediction. From the rainfall intensity comparison, it is difficult to specify whether the extended prediction produces an improvement of accuracy or reasonable reliability range to the original deterministic prediction. The intensities of the extended prediction fields distributed to the outer part of the deterministic rainfall intensity and the range of the ensemble prediction hardly covers the observed intensities.

The correlation coefficients from the extended prediction show improved results in most prediction times. Figure 3.6 (b) represents the correlation coefficients of the extended prediction fields and the observed radar rainfall fields as well as the coefficients of the deterministic prediction fields. In most prediction times, the coefficients from the extended prediction fields have higher values compared to the values from the deterministic prediction. When considering that the correlation coefficient value is a rather strict measurement index for prediction performance, the improved correlation values are encouraging results implying the enhancement of the prediction accuracy.

Yet, the CSI values in Figure 3.6 (c) do not show a vast difference between the extended prediction and the deterministic prediction. Because the error field simulation is based on the most recent prediction results, theoretically, the simulated error field contains the same area as the prediction fields. Even though there is slight variation of rainfall covering area as time passes, it does not significantly alter the CSI values, as they can simply be considered as an overlap ratio of prediction towards the observation.

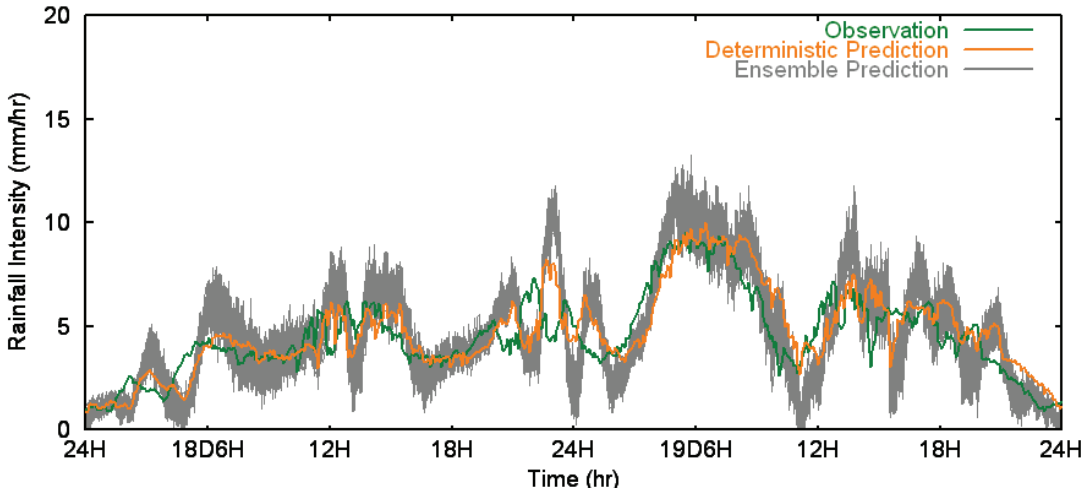

(a) Average rainfall intensity

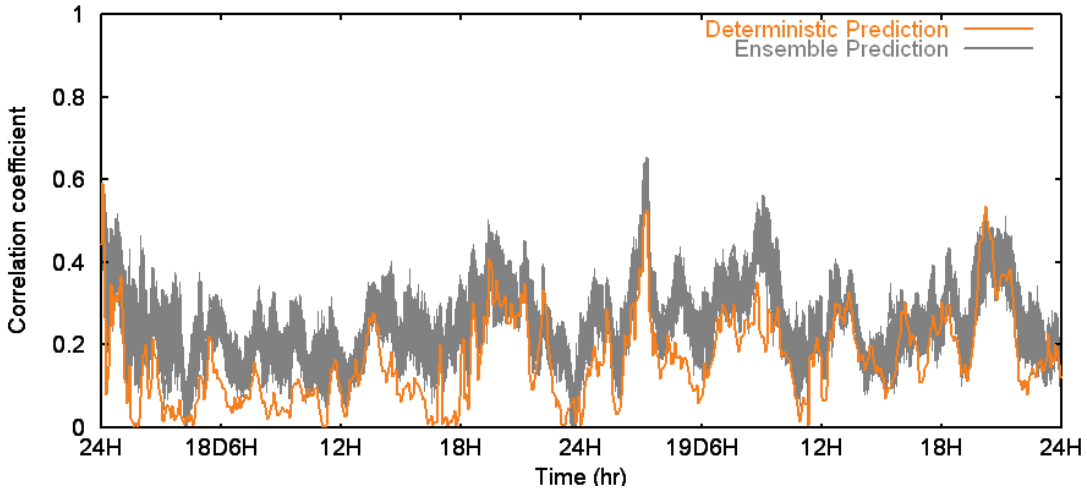

(b) Correlation coefficient

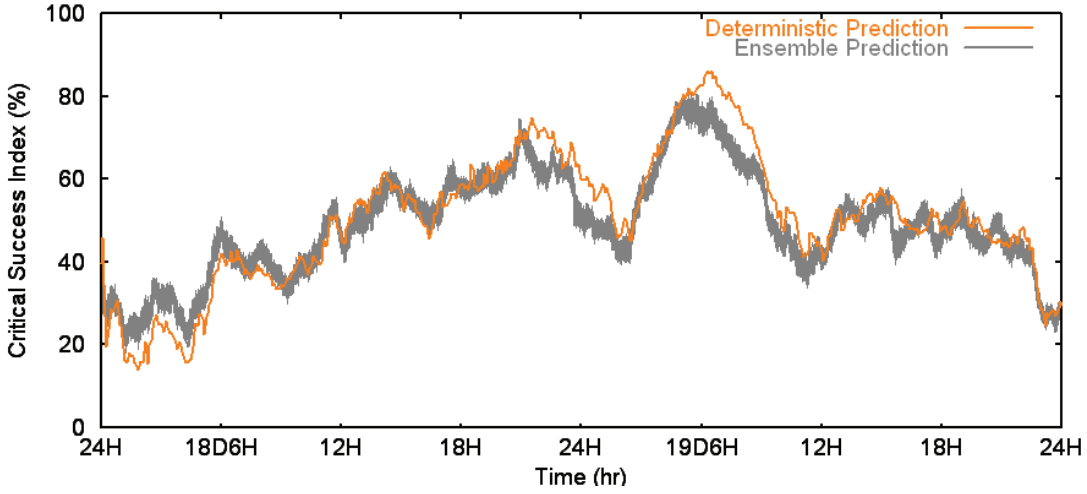

(c) Critical success index

Figure 3.6 Evaluations for extended prediction fields (August 1992 Event, 60min Pred.).

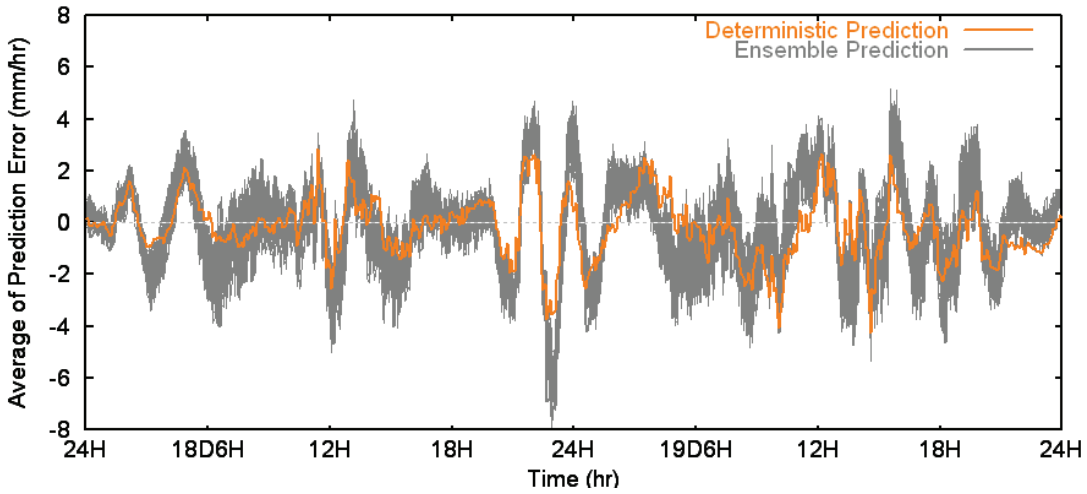

(d) Mean of Prediction error

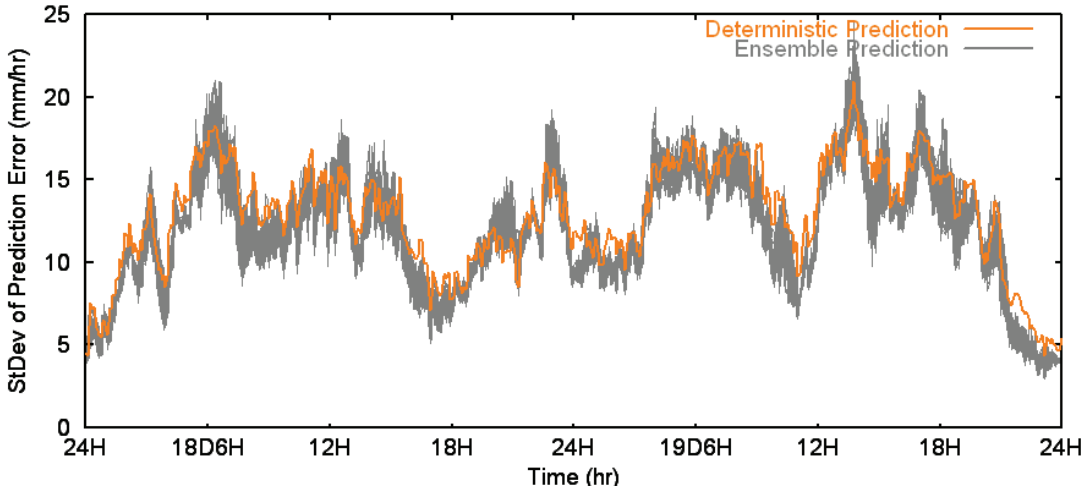

(e) Standard deviation of error

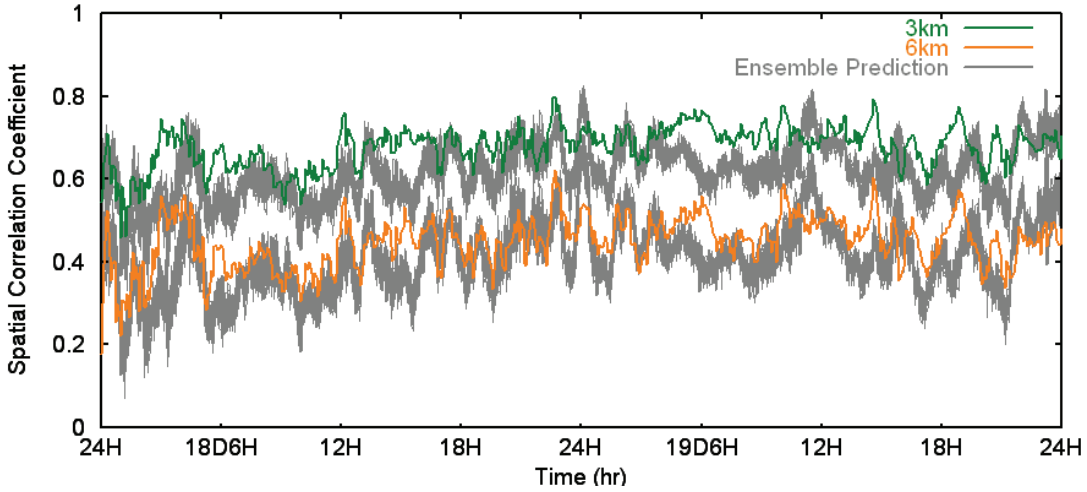

(f) Spatial correlation coefficient

Figure 3.6 Evaluations for extended prediction fields (continued) (Event in August 1992, 60 min Prediction).

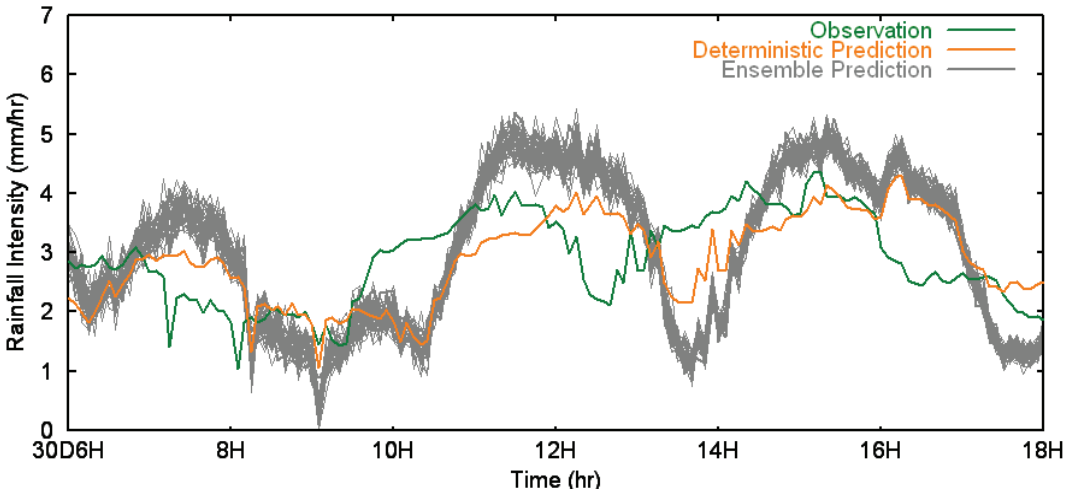

(a) Average rainfall intensity

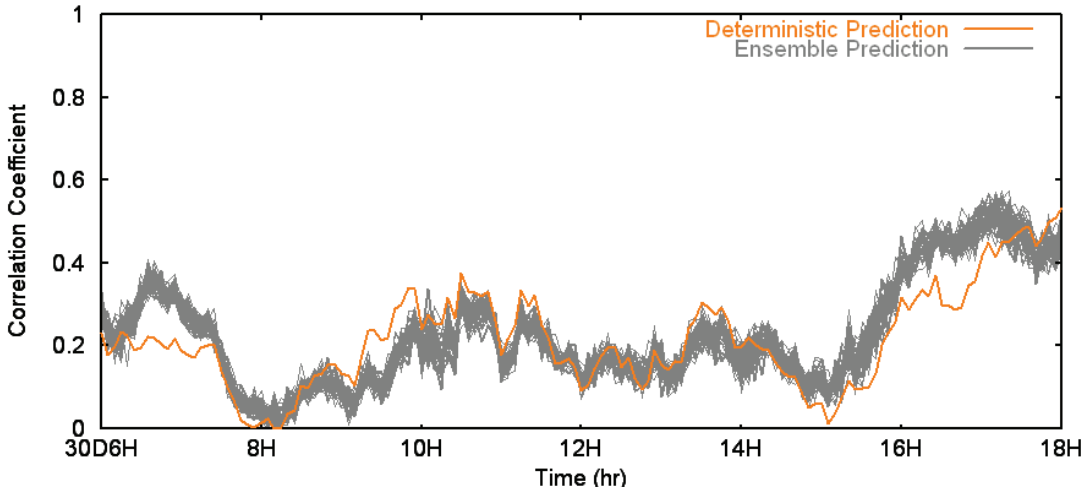

(b) Correlation coefficient

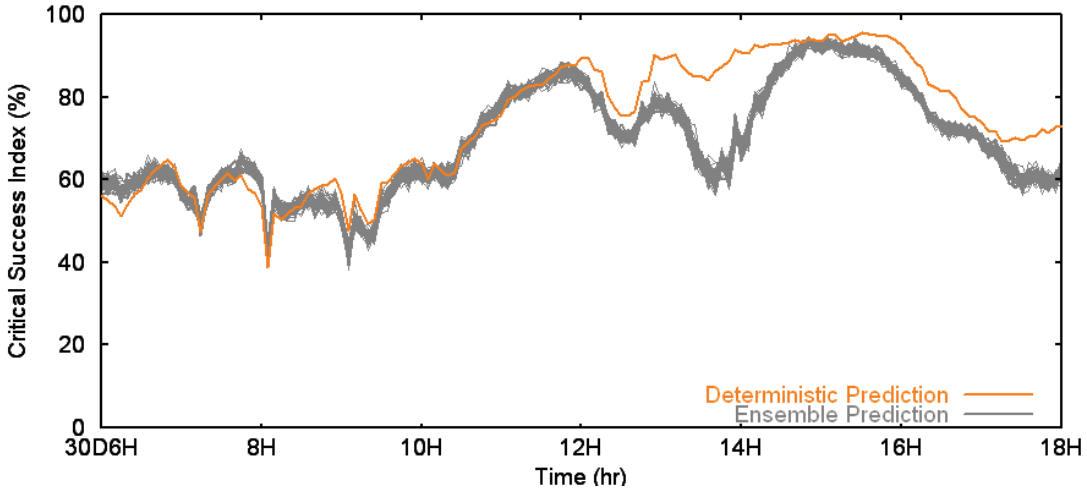

(c) Critical success index

Figure 3.7 Evaluations for extended prediction fields (June 1993 Event, 60min Prediction).

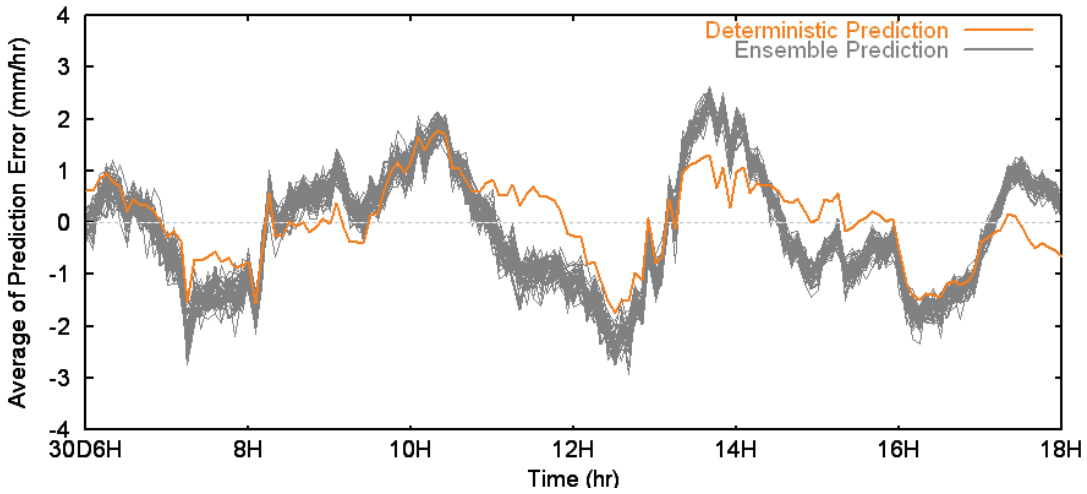

(d) Mean of Prediction error

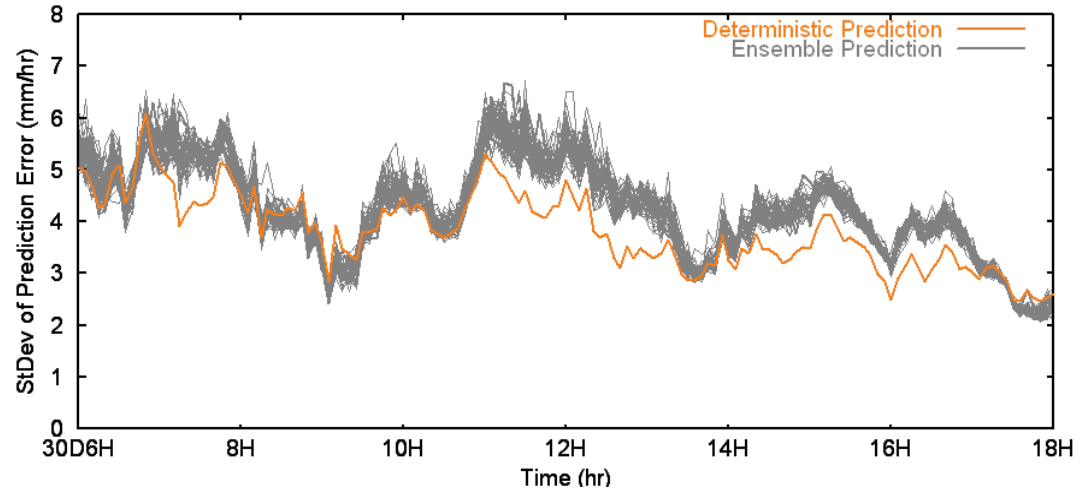

(e) Standard deviation of error

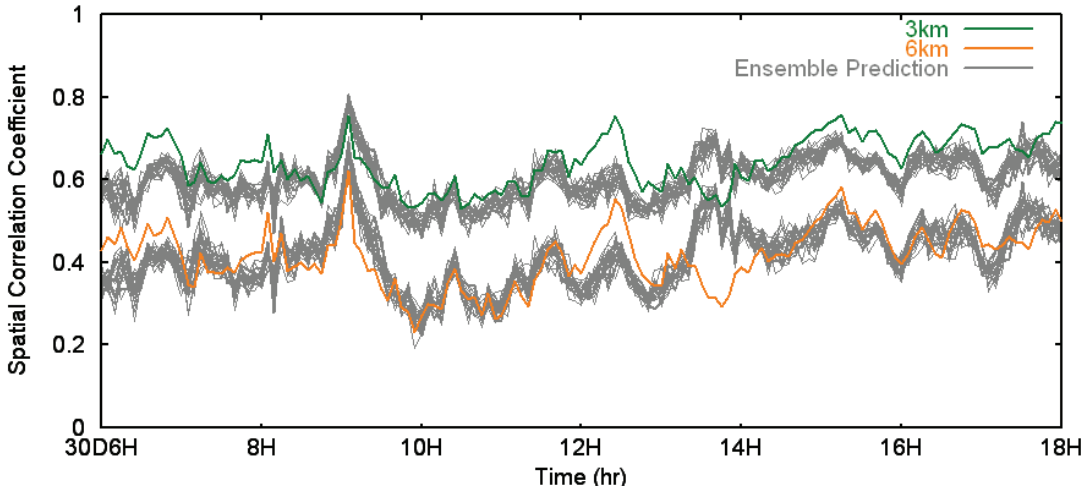

(f) Spatial correlation coefficient

Figure 3.7 Evaluations for extended prediction fields (continued) (Event in June 1993, 60 min Prediction).

The mean (Figure 3.6 (d) and 3.7 (d)) and standard deviation (Figure 3.6 (e) and 3.7 (e)) of the simulated prediction error show that the statistical characteristics of the prediction error as well as spatial correlation coefficients (Figure 3.6 (f) and 3.7 (f)) were successfully maintained throughout the error field simulation.

3.3.4 Forecast Verification

For an overall forecast verification, several performance indexes were adopted, such as accumulated rainfall amounts, root mean square error and mean absolute error. First, accumulated rainfall amount (*ACRA*) is the gradual amount of rainfall during the simulation after the rainfall intensities are spatially averaged. The *ACRA* of observed and forecasted (whether deterministic or ensemble) rainfall is calculated as:

$$ACRA = \sum_{t=1}^{n_t}\left(\frac{1}{n_s}\sum_{s=1}^{n_s} O_{t,s}\right) \quad or \quad = \sum_{t=1}^{n_t}\left(\frac{1}{n_s}\sum_{s=1}^{n_s} F_{t,s}\right) \tag{3.7}$$

where n_s and n_t are the number of rainfall grids, and time increments. $O_{t,s}$ and $F_{t,s}$ are observed and forecasted values at time t on point s. Note that the observed values $O_{t,s}$ may different to the ground gauge observation, since the radar observation used in this study is not adjusted to the ground gauge data. However, this radar observation $O_{t,s}$ is regarded as the reference rainfall values of the forecasted rainfall.

For the ensemble forecasting results, which has fifty sets of the extended prediction field, the mean and standard deviation of the *ACRA* were calculated, and the minimum and maximum of the *ACRA* values were examined as shown in Figure 3.8 and 3.9 as well as Table 3.3 and 3.4. Better results having closer *ACRA* value to the observed one are marked with bold character in those tables.

Additional performance indexes adopted to attain a single overall score are Root Mean Square Error (*RMSE*) and Mean Absolute Error (*MAE*) as expressed in Equation 3.8 and 3.9.

$$RMSE = \frac{1}{n_t}\sum_{t=1}^{n_t}\left(\sqrt{\frac{1}{n_s}\sum_{s=1}^{n_s}(O_{t,s} - F_{t,s})^2}\right) \tag{3.8}$$

$$AME = \frac{1}{n_t}\sum_{t=1}^{n_t}\left(\frac{1}{n_s}\sum_{s=1}^{n_s}\left|O_{t,s} - F_{t,s}\right|\right) \tag{3.9}$$

The simplest method for an overall scoring of forecast performance is to disregard the difference between the temporal and spatial dimensions, namely all error information is comprised into one value (Drosdowsky and Zhang, 2003). In most forecast results, the forecast performance will variant not only event by event, but also spatially and temporally even down to one event. Although this kind of comprisal scoring is not appropriate for examining a specific spatial and temporal variance of the forecast performance, *RMSE* and *MAE* are still convenient to check the overall comparison of performance, which is implemented by other similar forecast methods, along with the overall pattern of performance from the variant lead-times.

Lastly, time averaged correlation coefficient and critical success index were examined. These are simply the mean of *CC* and *CSI* values' time series for a perspective comparison of variant prediction lead-time.

$$MCC = \frac{1}{n_t}\sum_{t=1}^{n_t} CC_t \tag{3.10}$$

$$MCSI = \frac{1}{n_t}\sum_{t=1}^{n_t} CSI_t \tag{3.11}$$

Figure 3.8 and Table 3.3 show the comparison of accumulated rainfall amount values of observation, deterministic and ensemble prediction from the variant prediction lead-time of the August 1992 Event. In the figure, *ACRA* of the observation is presented with a

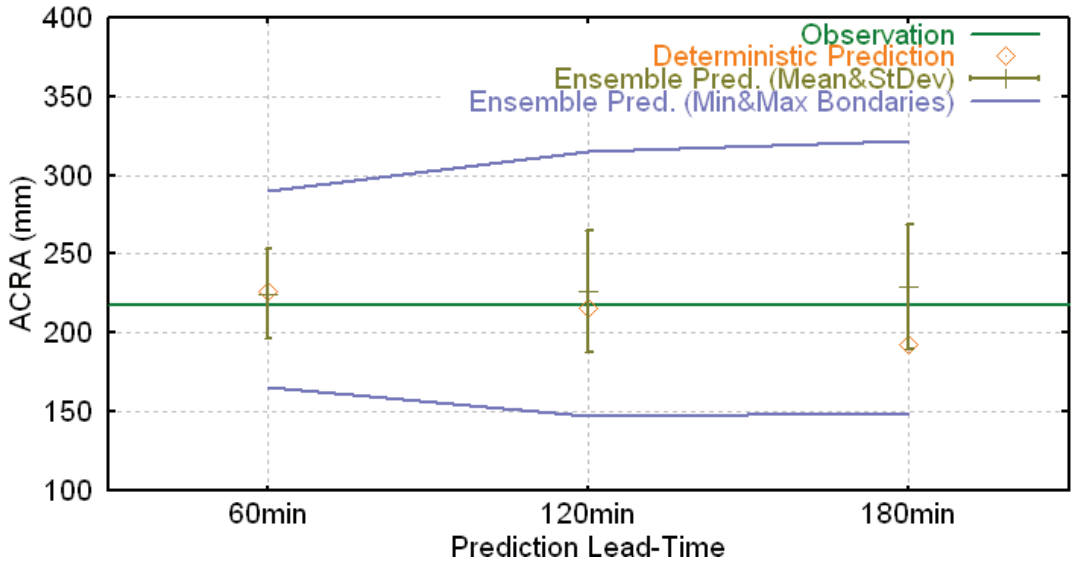

Figure 3.8 Accumulated rainfall amounts comparison (August 1992 Event).

Table 3.3 Accumulated rainfall amount values (August 1992 Event, Unit: mm/hr).

Lead-time	Observation	Deterministic Prediction	Ensemble Prediction	
			Mean±StDev	Min~Max
60 min Pred.	217.38	226.64	**224.79**±28.51	165.09~290.06
120 min Pred.	217.38	**215.94**	226.29±38.29	147.15~314.78
180 min Pred.	217.38	192.17	**228.97**±39.74	149.04~321.40

solid green line along the *x*-axis for showing the reference value, 217.38 mm. Here, the *x*-axis represents the prediction lead-time. The ACRA values from the deterministic and ensemble prediction are expressed with points and error-bars.

The *ACRA* values from the deterministic prediction decrease as prediction lead-time elongates, showing some differences to the observed one. The reason of the decrease can be found in the simulation behavior of the Translation model. When the model performs a simulation, the optimized *u* and *v* vector transfer the current rain bands, and therefore some rainfall area is located outside of the radar range at the prediction target time. In addition, because new rain band that comes in the radar range during the prediction lead-time is not counted in the prediction results, the deterministic prediction shows a trend of decreasing rainfall area as well as the *ACRA* values.

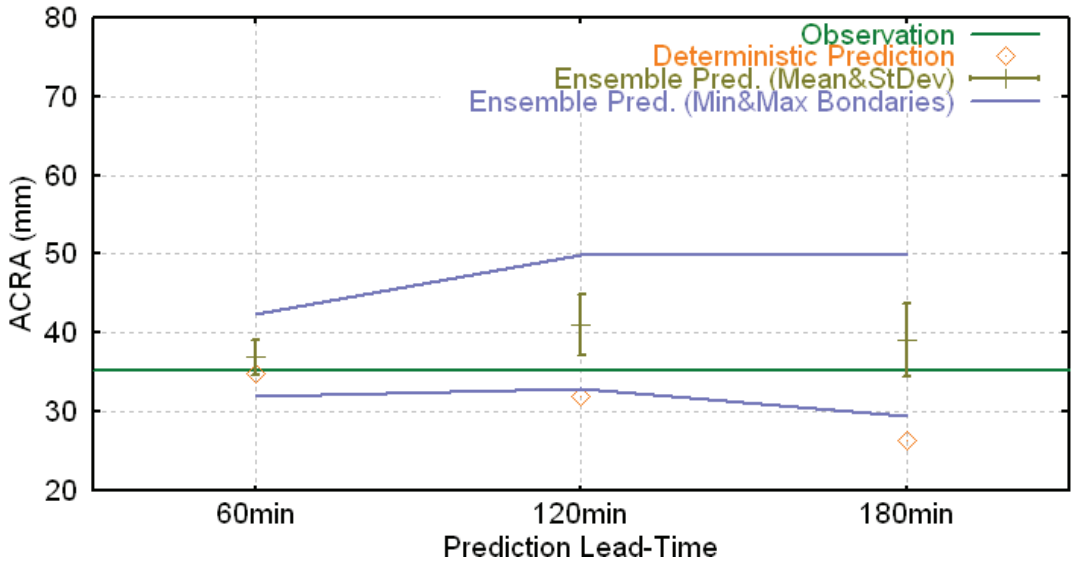

Figure 3.9 Accumulated rainfall amounts comparison (June 1993 Event).

Table 3.4 Accumulated rainfall amount values (June 1993 Event, Unit: mm/hr).

	Observation	Deterministic Prediction	Ensemble Prediction	
			Mean±StDev	Min~Max
60 min Pred.	35.14	**34.81**	36.88±2.30	31.97~42.28
120 min Pred.	35.14	**32.01**	40.98±3.85	32.85~49.97
180 min Pred.	35.14	26.42	**39.06**±4.67	29.39~50.06

However, the error field simulation of this study incorporates the information of the newly added rain bands, and as a result, the ensemble forecasting shows relatively steady *ACRA* values regardless of the prediction lead-time.

The reliability range of the ensemble forecasting (whether the standard deviation, or the maximum and minimum values) clearly expresses the uncertainty of the forecasted values; the larger the prediction lead-time is extended, the wider the range becomes. In the case of 180 min prediction, the standard deviation of the ensemble forecasting's *ACRA* is ±39.74 mm, and the difference of the minimum and the maximum value is 172.36 mm, which might be considered as a large uncertainty for a 3 hrs lead-time forecasting. The Detailed values are presented in Table 3.3.

Figure 3.9 shows the comparison of *ACRA* values from the variant prediction lead-time of the June 1993 Event. In the figure, *ACRA* of the observation is 35.14mm and the values from the deterministic prediction show a larger discrepancy for the observation as the lead-time gets longer. While the mean values from the ensemble forecasting also show negative results, the range values from the ensemble simulation successfully encompass the observation values. Detail vales are illustrated in Table 3.4.

Table 3.5 Root mean square error and mean absolute error (August 1992 Event).

Lead-time	RMSE		MAE	
	Deterministic	Ensemble	Deterministic	Ensemble
60 min Pred.	12.97	**11.50**	5.96	**5.36**
120 min Pred.	14.01	**12.17**	6.60	**5.86**
180 min Pred.	14.06	**12.59**	6.58	**6.19**

Table 3.6 Root mean square error and mean absolute error (June 1993 Event).

Lead-time	RMSE		MAE	
	Deterministic	Ensemble	Deterministic	Ensemble
60 min Pred.	**5.22**	5.25	**3.26**	3.35
120 min Pred.	**5.33**	5.38	**3.36**	3.48
180 min Pred.	**5.41**	5.42	**3.41**	3.47

Tables 3.5 and 3.6 show the *RMSE* and *MAE* from the variant forecast lead-time of the August 1992 Event and June 1993 Event. The August 1992 Event clearly illustrates that the ensemble forecasts gives much smaller error values than the deterministic prediction in all lead-times. Furthermore, one should notice that both scoring values become larger for longer lead-times, which proves higher uncertainty for longer lead-time predictions. On the other hand, the June 1993 Event resulted in better values for the deterministic prediction than the ensemble forecasts. This may be because the June 1993 Event has low rainfall intensities, therefore the ensemble forecasts are much more influenced by the negative rainfall handling during the extended prediction field simulation. However, undefined spatial and/or temporal characteristics in a certain rainfall pattern can be there

during the June 1993 Event, and therefore more detailed study with various event types is required in order to generalize the proposed ensemble forecasting method.

The mean of correlation coefficient (*MCC*) and mean of critical success index (*MCSI*) for the August 1992 Event and June 1993 Event are respectively presented in Table 3.7 and 3.8. The values for the ensemble forecasts are averaged values from the fifty sets of extended prediction results. From the both tables, the values clearly show that ensemble forecasts give improved accuracy compare to the deterministic predictions while the accuracy decreases as prediction lead-time gets longer.

Table 3.7 MCC and MCSI values comparison (August 1992 Event).

	Mean Correlation Coefficient		Mean Critical Success Index (%)	
	Deterministic	Ensemble	Deterministic	Ensemble
60 min Pred.	0.164	**0.252**	**50.5**	49.1
120 min Pred.	0.063	**0.173**	42.1	**46.6**
180 min Pred.	0.052	**0.143**	36.6	**45.7**

Table 3.8 MCC and MCSI values comparison (June 1993 Event).

	Mean Correlation Coefficient		Mean Critical Success Index (%)	
	Deterministic	Ensemble	Deterministic	Ensemble
60 min Pred.	0.216	**0.229**	**74.03**	69.45
120 min Pred.	0.090	**0.123**	65.15	**66.73**
180 min Pred.	0.070	**0.072**	56.51	**64.86**

3.4 Ensemble Runoff Simulation with a Distributed Hydrologic Model

For real-time flood forecasting, there has been considerable interest in utilizing weather radar and distributed hydrologic models, as it can provide continuous spatiotemporal measurements and outputs that are immediately available at any location in catchments. From a hydrological point of view, runoff responses of forecasted rainfall throughout a

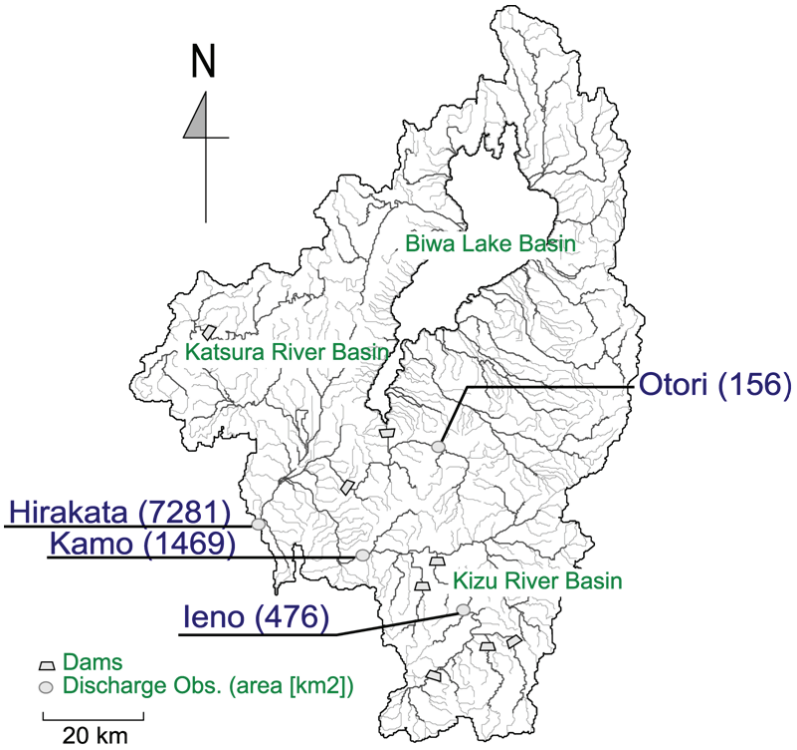

Figure 3.10 Entire Yodo river basin and its sub-basins: Ootori, Ieno and Kamo.

hydrologic system are valuable information for checking the validity of the input data during operational usage. This study assesses the simulated extended prediction fields with a distributed hydrologic model, which is developed for the Yodo river basin located in the Miyama radar observation range. Figure 3.10 shows the Yodo river basin as well as its sub-basins, and the location map of the basin is given in Figure 2.1.

The Yodo river model (Sayama *et al*., 2005) used in this study solves kinematic wave equations for both subsurface flow and surface flow using the Lax-Wendroff scheme. Discharge and water depth propagate node to node according to a predefined routine order, which is determined in accordance with DEM and river channel network data. One characteristic of the Yodo river model is a specific stage-discharge relationship, which incorporates saturated and unsaturated flow mechanisms. More details about the stage-discharge relationship are illustrated in Chapter 4 with an introduction of the distributed hydrologic model, CDRMV3. For additional details on the Ohymos system refer to Ichikawa *et al*.(2000), and on the Yodo river model refer to Sayama *et al*.(2005).

The runoff simulation is carried out in three different catchments located within the observation range of the Miyama radar: Ootori (156 km^2), Ieno (476 km^2) and Kamo (1469 km^2). The catchments, which are located near the radar station (see Figure 2.2) are selected to avoid inherent radar error, which is mainly caused by reflectivity attenuation. The parameters were calibrated with the Miyama radar observation and observed discharge data for each outlet. Although the calibrated parameter set may not necessarily correspond to the best series, and additionally the simulated results does not specifically represent the actual discharge, the simulated discharge from the observed radar data is nevertheless set as a reference to compare with the discharge from the deterministic prediction and extended prediction data.

The purpose of this rainfall-runoff simulation is to examine the accuracy and reliability range of the extended rainfall prediction from a hydrological point of view. The final goal is the achievement of ensemble discharge, which has values around the discharge output from the observation.

3.5 Application Results and Discussion

The fifty sets of extended prediction fields generate an ensemble rainfall-runoff simulation through the distributed hydrologic model. Each extended prediction field among the fifty sets of input data was assigned to each runoff simulation independently. Firstly, preliminary simulation was conducted with the observed rainfall data until 0:00 on the 18th for the August 1992 Event and until 6:00 on the 30th for the June 1993 Event. The deterministic and extended prediction fields data was inputted after the above mentioned times. The ensemble simulation was carried out until 0:00 on the 20th (August 1992 Event) and until 18:00 on the 30th (June 1993 Event). After those time periods, the observed rainfall data was equally set to every fifty-ensemble simulation, upon which the simulation was shortly continued in order to observe the remaining effect of the input rainfall on the runoff. The rainfall data, whether observed or predicted, was given every 5 min for the distributed hydrologic model, which produced a hydrograph every 10 min.

Figure 3.10 shows the ensemble runoff simulation results (60 min prediction) in the August 1992 Event for all three subject basins: Ootori (156 km^2), Ieno (476 km^2) and Kamo (1469 km^2). The green line stands for the discharge from the observed radar rainfall, which is the reference discharge regarded as the actual value. The orange line represents the discharge from the original deterministic predicted rainfall for 60 min ahead of every time increment. Fifty gray lines show each discharge from the extended prediction fields, which was simulated in the previous section.

In the three sets of the simulation results, the discharges from the ensemble simulations show closer values to the discharges from the observed radar rainfall, which implies the improved prediction accuracy of the extended prediction. At the first peak in the Ootori simulation (17:00 on the 18^{th} of August) in Figure 3.11 (a), the deterministic prediction produced a 350 m^3/sec discharge, while the reference discharge form the observed rainfall produced only 90 m^3/sec. The discharge results from the extended prediction data diminished from the highly overestimated value above down to 150 m^3/sec. The results from the Ieno simulation (Fig 3.11 (b)) clearly show the improved prediction accuracy with the reduced discharge compared to the output from the deterministic rainfall data.

From Figures 3.11 to Figure 3.16 show the same form of the ensemble simulation results with a 60, 120 and 180 min prediction of the August 1992 Event and the June 1993 Event. While the results with the August 1992 Event give optimistic results for the 120 min prediction, the results with the June 1993 Event show that the ensemble simulation with error field simulation still has much room for improvement.

Note that the ensemble simulation results were given by the continuous application of the extended prediction data, therefore the discharge output accumulated the prediction error. In a practical usage of forecasts rainfall data in a real-time simulation, the rainfall input data will be given in accordance with the most updated forecast for each lead-time. When considering that only the 60, 120 or 180 min prediction data was given for every time increment, the improved accuracy proved and continues to be worthy of attention in practical usages.

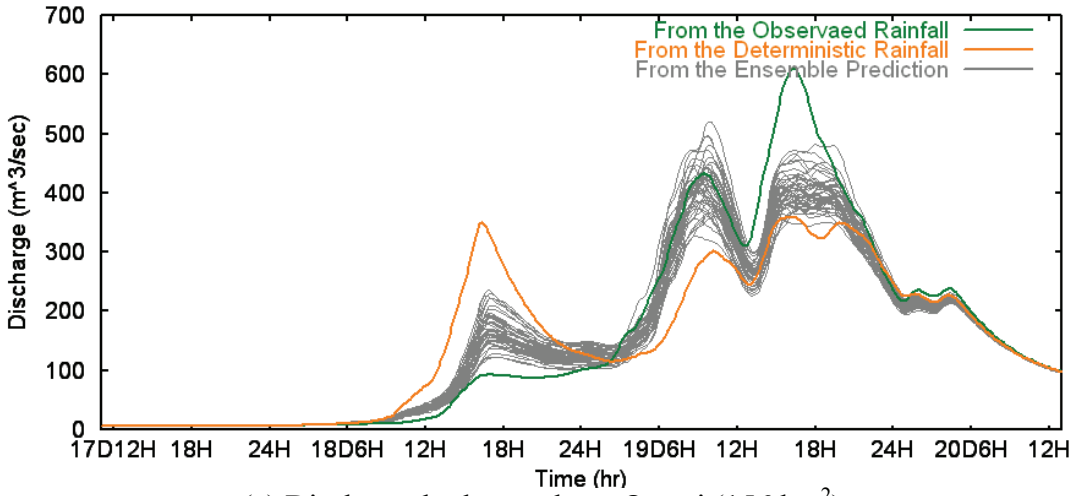

(a) Discharge hydrographs at Ootori (156 km^2)

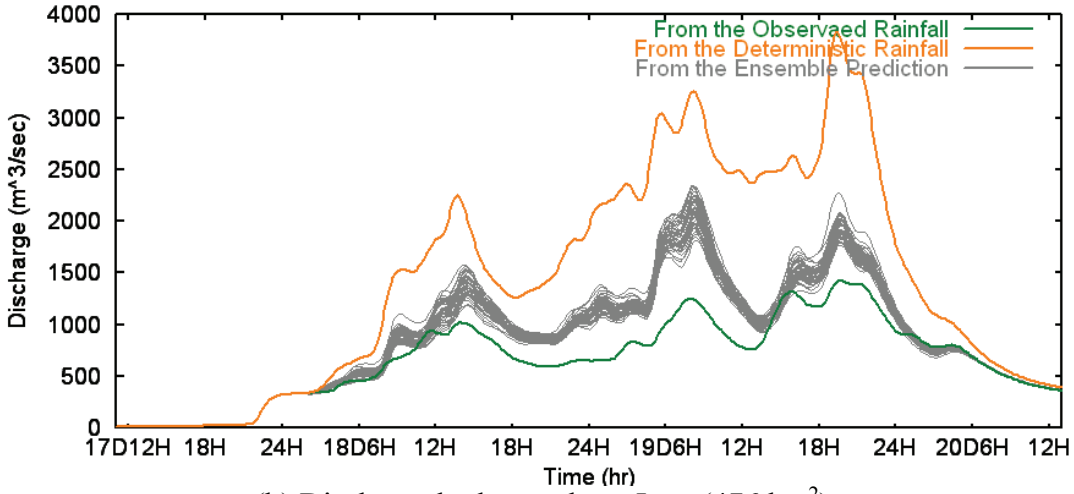

(b) Discharge hydrographs at Ieno (476 km^2)

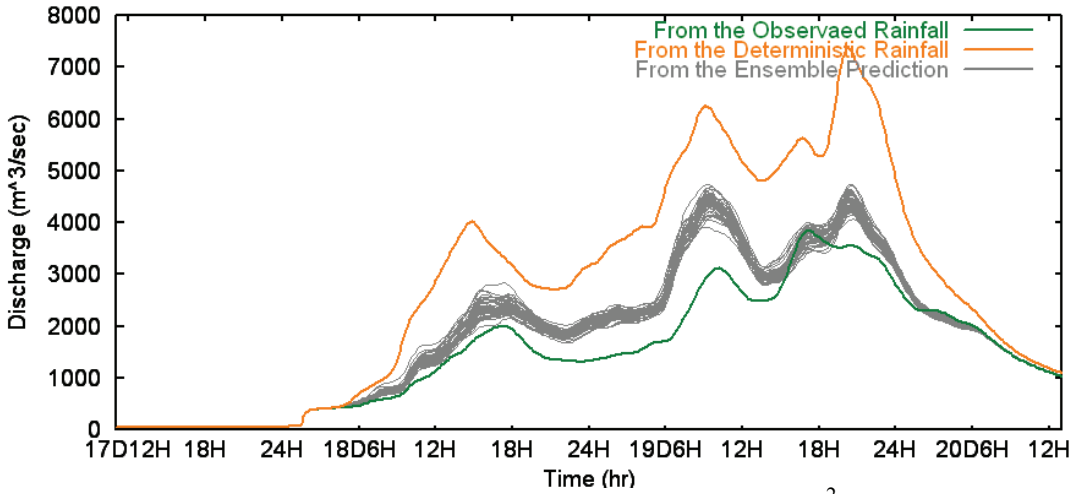

(c) Discharge hydrographs at Kamo (1469 km^2)

Figure 3.11 Runoff simulation results with 60 min prediction, August 1992 Event.

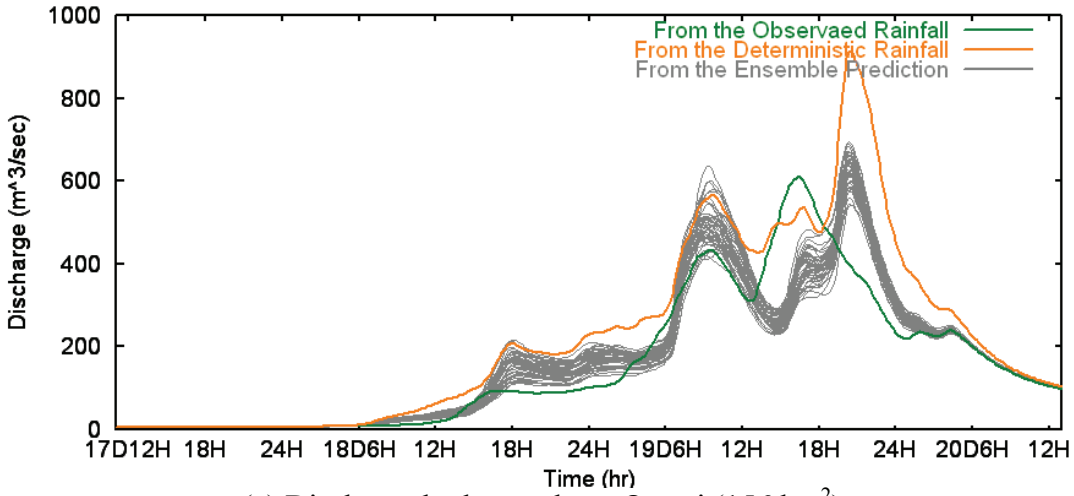

(a) Discharge hydrographs at Ootori (156 km^2)

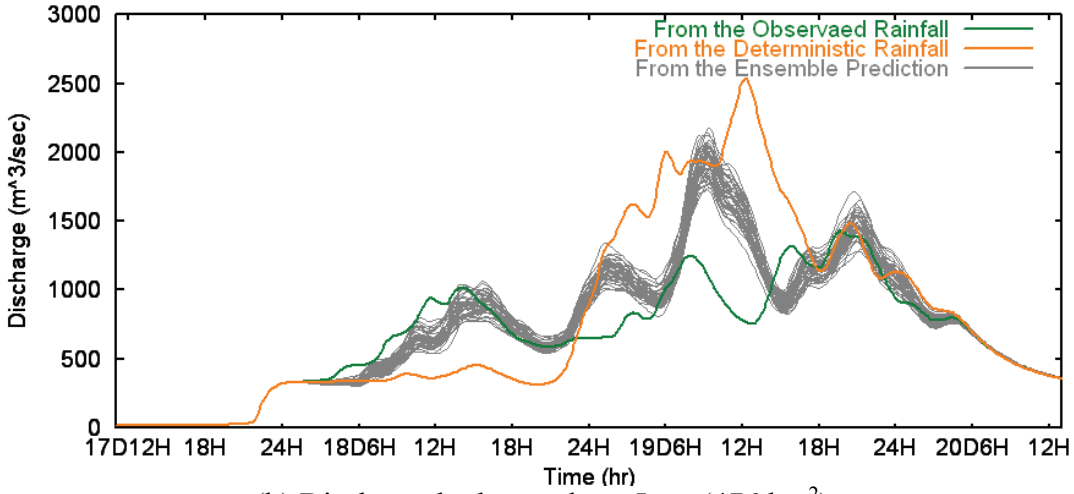

(b) Discharge hydrographs at Ieno (476 km^2)

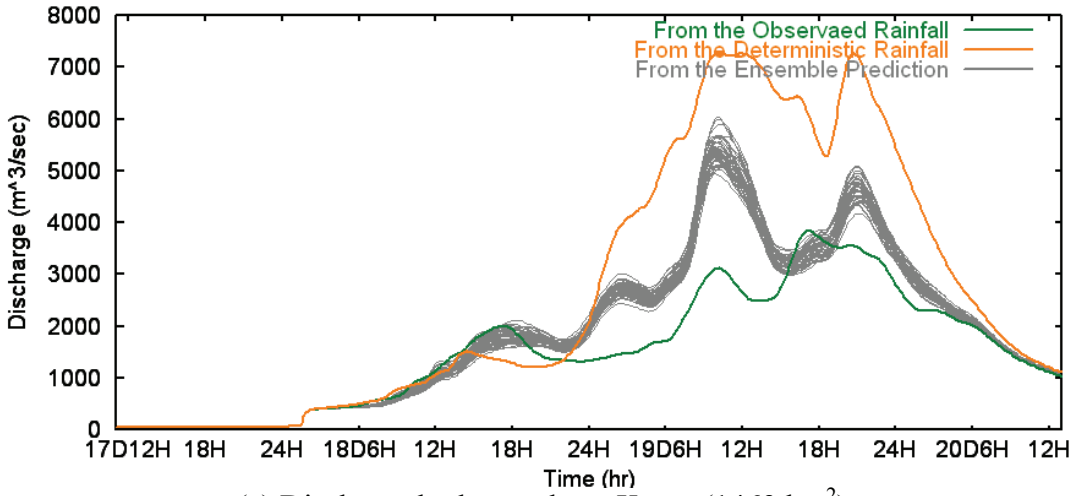

(c) Discharge hydrographs at Kamo (1469 km^2)

Figure 3.12 Runoff simulation results with 120 min prediction, August 1992 Event.

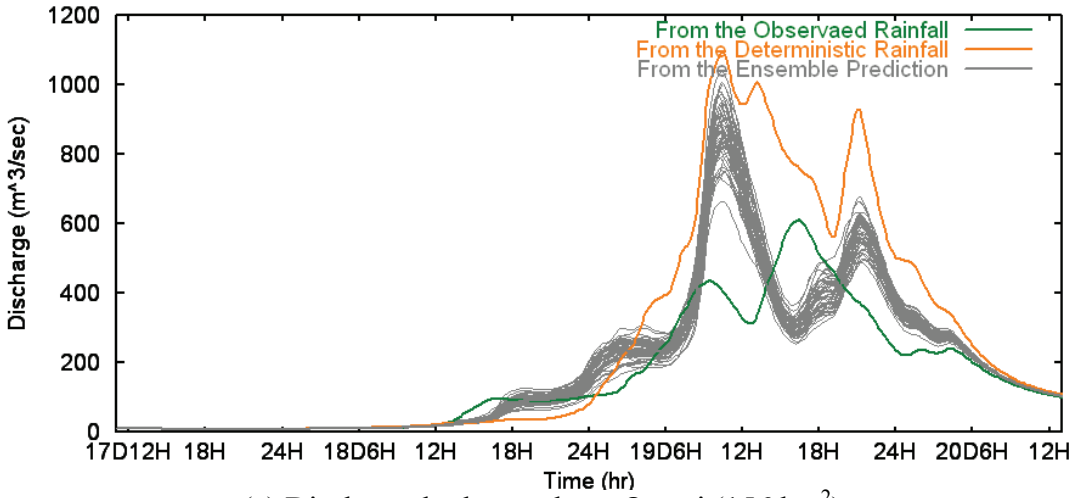

(a) Discharge hydrographs at Ootori (156 km^2)

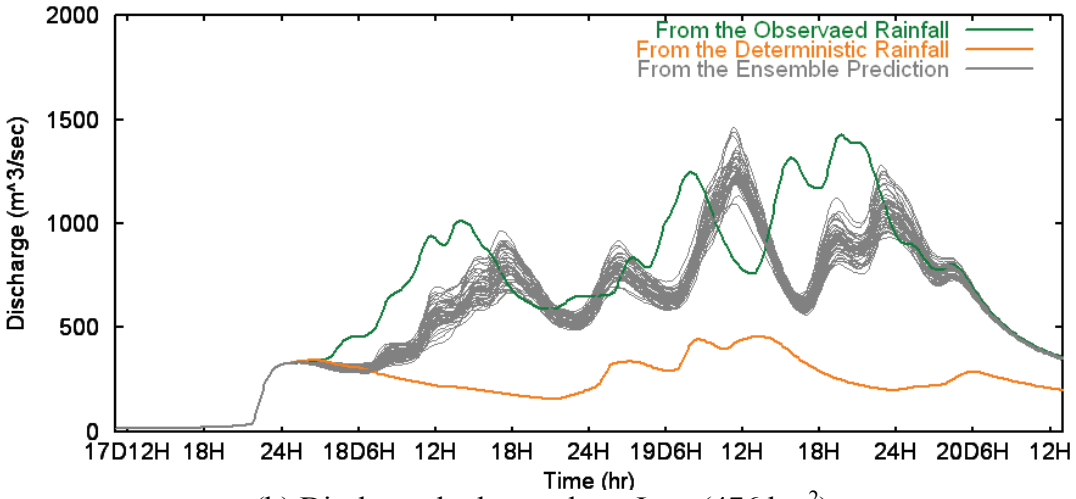

(b) Discharge hydrographs at Ieno (476 km^2)

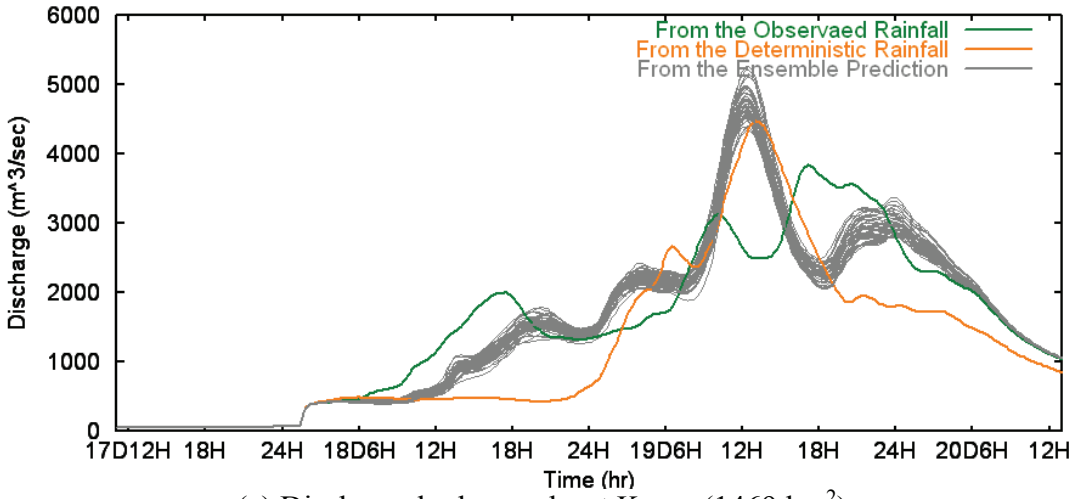

(c) Discharge hydrographs at Kamo (1469 km^2)

Figure 3.13 Runoff simulation results with 180 min prediction, August 1992 Event.

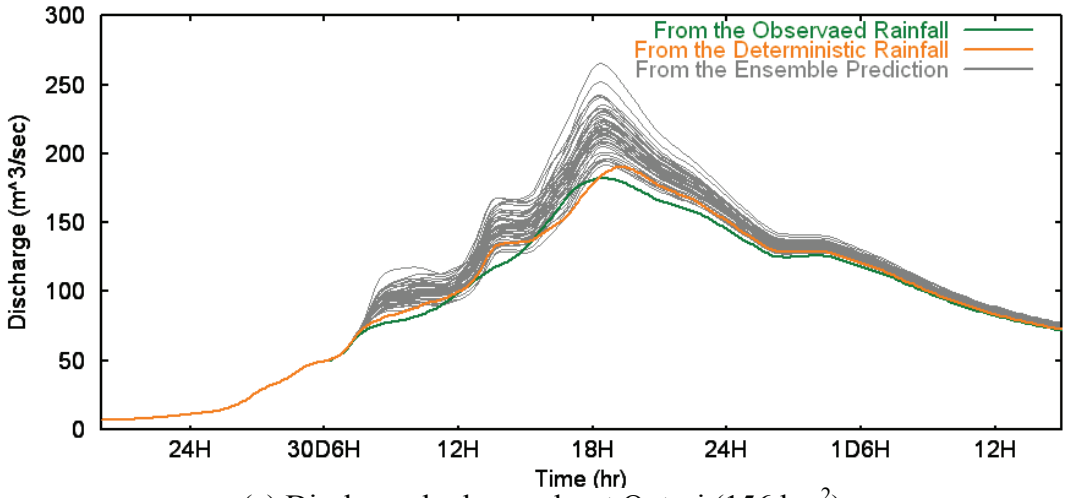

(a) Discharge hydrographs at Ootori (156 km^2)

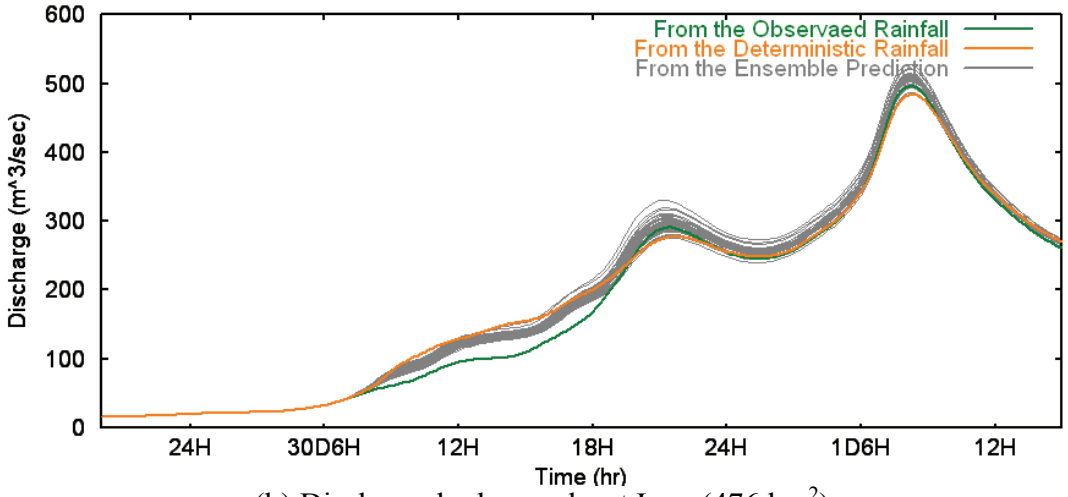

(b) Discharge hydrographs at Ieno (476 km^2)

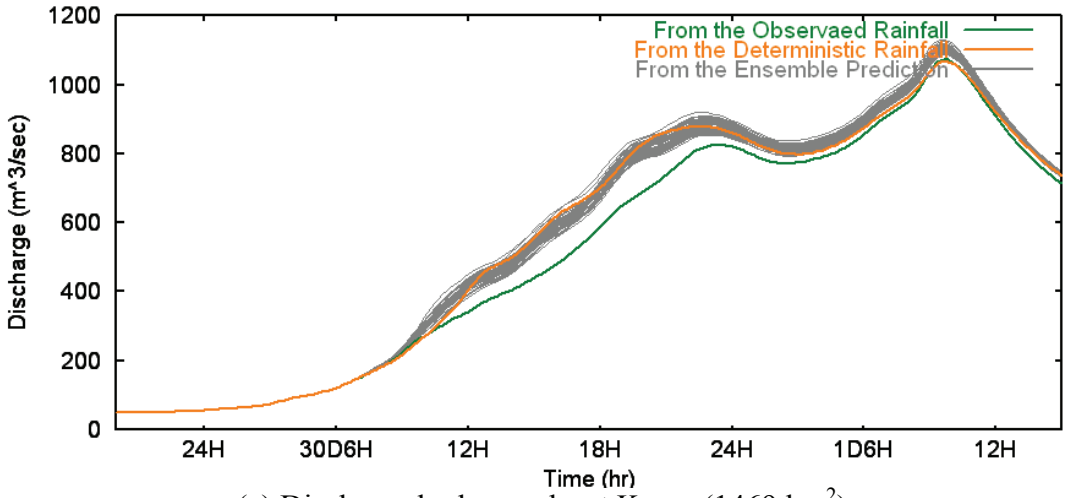

(c) Discharge hydrographs at Kamo (1469 km^2)

Figure 3.14 Runoff simulation results with 60 min prediction, June 1993 Event.

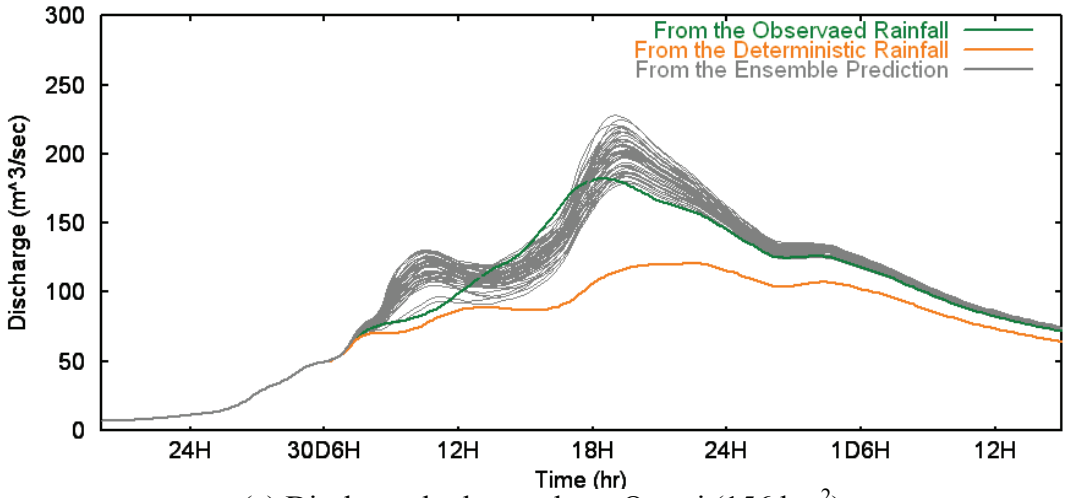

(a) Discharge hydrographs at Ootori (156 km^2)

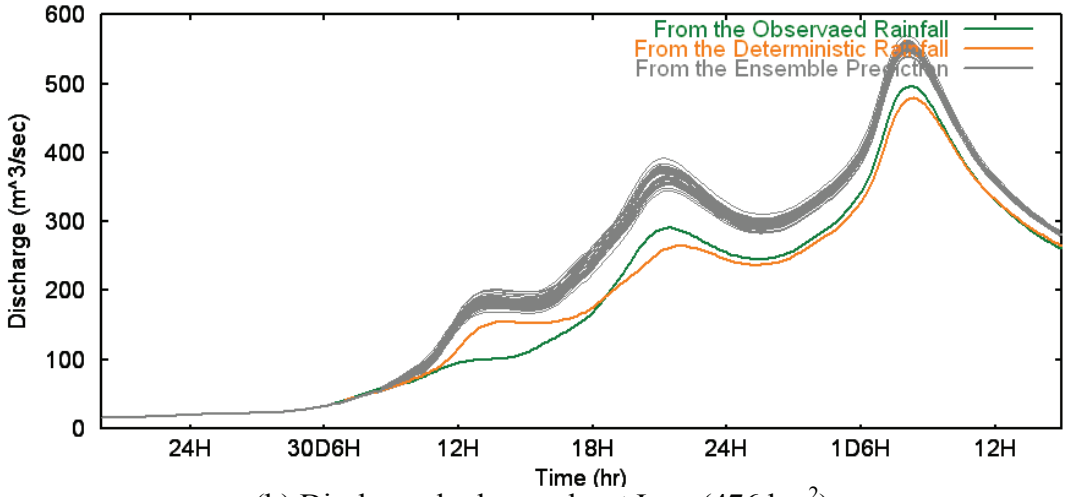

(b) Discharge hydrographs at Ieno (476 km^2)

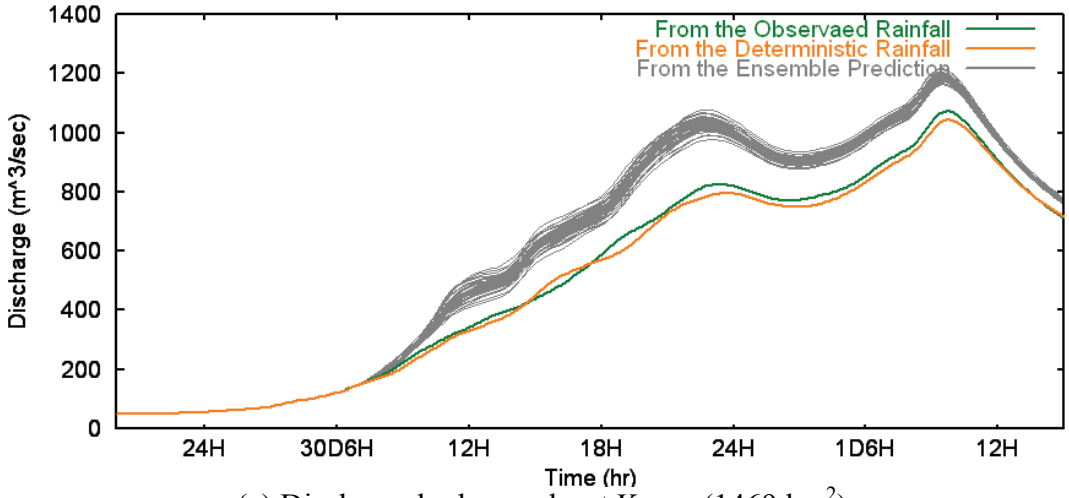

(c) Discharge hydrographs at Kamo (1469 km^2)

Figure 3.15 Runoff simulation results with 120 min prediction, June 1993 Event.

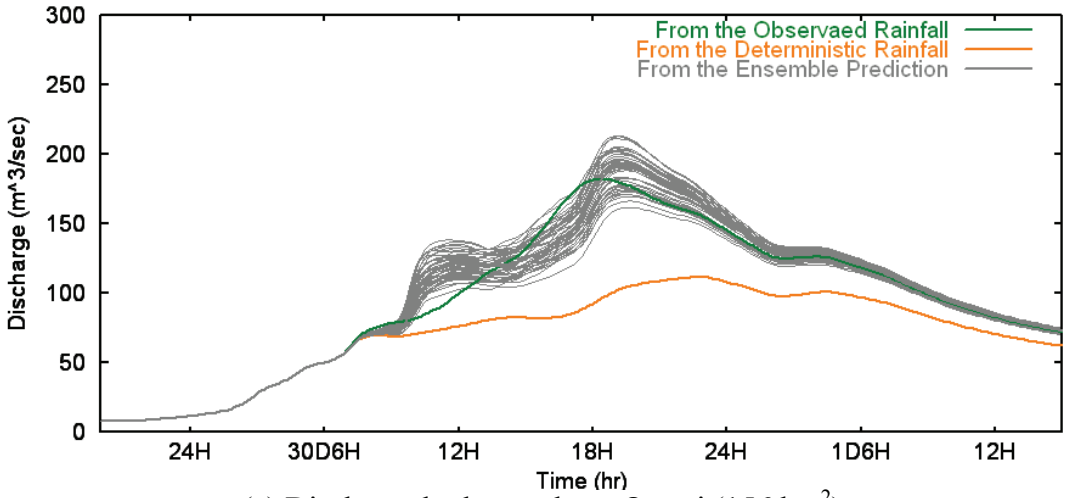

(a) Discharge hydrographs at Ootori (156 km^2)

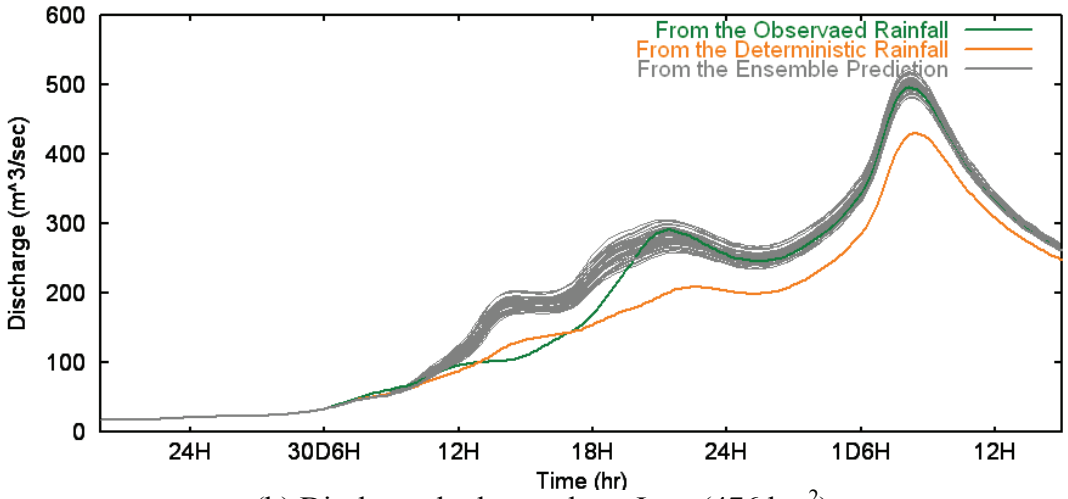

(b) Discharge hydrographs at Ieno (476 km^2)

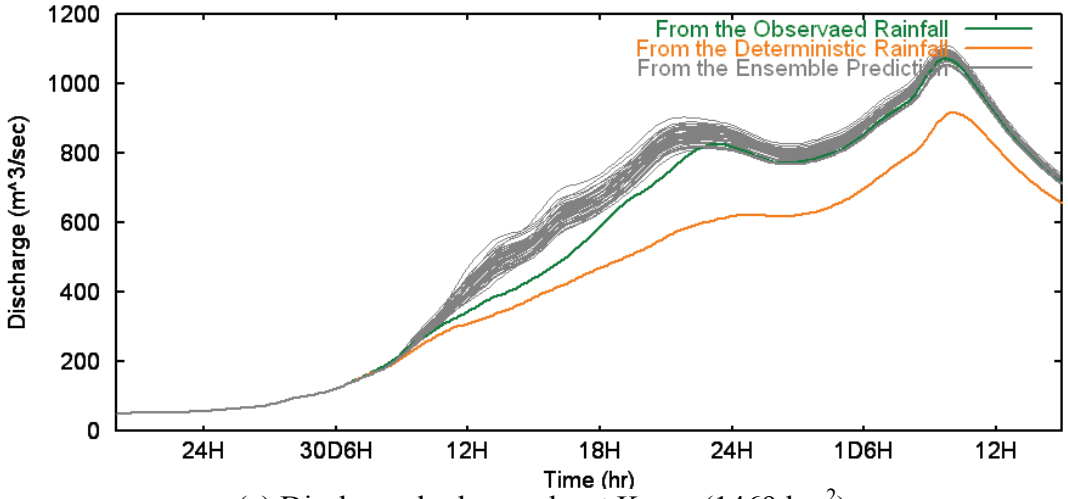

(c) Discharge hydrographs at Kamo (1469 km^2)

Figure 3.16 Runoff simulation results with 180 min prediction, June 1993 Event.

While the improvement of forecast accuracy show encouraging developments, the band, which stands for the reliability range of the extended prediction, is hard to determine that the results are acceptable. Proper reliability bands from the ensemble simulation should be around the true values, but the presented results hardly cover the reference discharge with a wide enough range. Wider reliability bands can be simply acquired by applying longer durations for the statistic fields, since in most cases, longer duration gives bigger standard deviation. However, more study for giving proper reliability range with appropriate duration for the statistic fields should be continued.

For an overall comparison of the ensemble runoff simulation, peak discharges of each case from both events are extensively examined, and those values are presented in Table 3.9 and 3.10. In the case of August 1992 Event, the peak discharges form the deterministic prediction give variant values showing large overestimation in most cases. For example, the peak discharge of Kamo basin for 60 min prediction is 7362.8 m^3/sec, while the peak of observation is only 3836.1 m^3/sec. However, the ensemble forecasting using the error simulation model decreases that overestimation of discharge down to 4474.8 m^3/sec. In most simulation case of the August 1992 Event, the ensemble forecast gives accuracy improved results in a sense of having closer values to the reference discharges. The closer values are marked with bold character in the table.

In the results from the June 1993 Event (Table 3.10), about the half of the ensemble forecasting does not produce positive results with a reasonable reliability range. For Ieno and Kamo basin, the deterministic prediction already provides highly accurate peak discharge values, and the ensemble forecasting fails to offer much more accurate and reasonable reliability. This result may be because of a certain characteristic in the June 1993 Event as mentioned in the earlier section including low rainfall intensities.

The ACRA values are calculated using the rainfall data on each testing basin, and the values are presented in Table 3.11 and 3.12. The *ACRA* values of each basin has similar pattern to the earlier analysis using the overall rainfall amount within the radar range; the values from the ensemble forecasting provide not only improved result but also its reliability range. The accumulated rainfall amount in the August 1992 Event is rather

Table 3.9 Peak discharge comparison of August 1992 Evnet (Unit: m^3/sec).

	Prediction Lead-time	Observation	Deterministic Prediction	Ensemble Prediction	
				Mean	Min~Max
Ootori ($156km^2$)	60 min	610.3	358.9	**432.1**	378.0~520.3
	120 min	610.3	913.4	**622.5**	542.7~694.3
	180 min	610.3	1096.2	**866.9**	664.1~1040.3
Ieno ($476km^2$)	60 min	1426.7	3838.6	**2108.4**	1882.5~2348.5
	120 min	1426.7	2534.7	**1947.4**	1728.6~2175.2
	180 min	1426.7	454.3	**1259.9**	1095.5~1463.2
Kamo ($1469km^2$)	60 min	3836.1	7362.8	**4474.8**	4063.2~4743.4
	120 min	3836.1	7271.0	**5385.6**	4939.0~6034.5
	180 min	3836.1	**4470.3**	4718.8	4343.5~5271.2

Table 3.10 Peak discharge comparison of June 1993 Event (Unit: m^3/sec).

	Prediction Lead-time	Observation	Deterministic Prediction	Ensemble Prediction	
				Mean	Min~Max
Ootori ($156km^2$)	60 min	181.8	**190.2**	218.6	191.5~265.3
	120 min	181.8	120.7	**201.2**	179.0~228.1
	180 min	181.8	111.3	**188.9**	161.6~213.1
Ieno ($476km^2$)	60 min	496.2	484.3	**504.6**	487.4~527.3
	120 min	496.2	**479.2**	552.2	538.5~569.4
	180 min	496.2	430.3	**501.5**	481.5~522.9
Kamo ($1469km^2$)	60 min	1073.6	**1067.2**	1104.5	1087.2~1131.2
	120 min	1073.6	**1043.8**	1190.5	1162.9~1218.6
	180 min	1073.6	918.0	**1083.2**	1052.9~1112.5

Table 3.11 Accumulated rainfall amount values of August 1992 Event (Unit: mm/hr).

	Prediction Lead-time	Observation	Deterministic Prediction	Ensemble Prediction	
				Mean±StDev	Min~Max
Ootori ($156km^2$)	60 min	273.2	341.6	**331.3**±24.2	284.7~376.8
	120 min	273.2	442.8	**357.9**±27.0	281.0~416.5
	180 min	273.2	593.8	**459.3**±30.9	390.7~507.0
Ieno ($476km^2$)	60 min	362.7	818.9	**487.5**±27.2	424.4~537.7
	120 min	362.7	437.3	**413.4**±26.4	350.4~477.4
	180 min	362.7	80.0	**300.3**±18.9	258.4~352.1
Kamo ($1469km^2$)	60 min	319.6	574.4	**389.2**±14.7	357.8~418.4
	120 min	319.6	533.5	**387.4**±18.9	340.5~421.1
	180 min	319.6	238.9	**312.4**±13.3	258.9~336.4

Table 3.12 Accumulated rainfall amount values of June 1993 Event (Unit: mm/hr).

	Prediction Lead-time	Observation	Deterministic Prediction	Ensemble Prediction	
				Mean±StDev	Min~Max
Ootori ($156km^2$)	60 min	58.2	55.2	**60.5**±7.1	46.1~80.2
	120 min	58.2	27.6	**51.1**±6.0	39.9~66.0
	180 min	58.2	39.7	**63.2**±7.9	48.5~88.1
Ieno ($476km^2$)	60 min	41.5	**50.0**	53.8±3.1	47.5~60.2
	120 min	41.5	**53.0**	62.1±3.5	54.0~71.6
	180 min	41.5	**44.4**	59.0±4.5	45.4~68.0
Kamo ($1469km^2$)	60 min	41.7	**51.4**	54.2±2.3	50.3~60.6
	120 min	41.7	**47.1**	58.7±2.9	49.9~63.5
	180 min	41.7	**36.8**	54.7±3.5	47.8~62.1

large amount when considering that is within two days' accumulation. However, this is because the radar observation used in this study is not adjusted to the ground gauge data, and it may cause some difference in rainfall intensity as well as accumulated amount.

For forecast accuracy improvement and ensemble flood forecasting with an external error consideration, this chapter introduced ensemble rainfall forecasting using a stochastic error field simulation along with a runoff simulation using a distributed hydrologic model. The proposed algorithm is for offering probable variation of the deterministic prediction results from the extrapolation model, as well as improving its forecast accuracy. The random error fields were simulated using the error structure, and the extended prediction field, which is the combination of the deterministic rainfall and the simulated error, was generated, after which its stochastic validity was examined. The extended prediction fields not only gave probable reliability with variant form of rainfall fields but also improved the accuracy of the deterministic prediction.

The validation of the extended prediction fields was completed from two different perspectives: juxtaposing the extended fields to the radar observed data, and comparing hydrographs simulated through a distributed hydrologic model. Firstly, the mean and standard deviation as well as spatial correlation coefficients of the simulated prediction error showed that the statistical characteristics of the prediction error were successfully maintained through the error field simulation.

Secondly, for an overall forecast verification, several performance indexes, such as *ACRA*, *RMSE* and *MAE* were adopted. From the *ACRA* testing, the reliability ranges of the ensemble forecasting clearly expressed the uncertainty of the forecasted values; the larger the prediction lead-time is extended, the wider the range becomes.

Finally, the ensemble runoff simulation results with the Yodo river model verified the hydrologic effectiveness of the extended prediction fields. While the ensemble runoff simulation showed highly encouraging results, the range, which stands for the reliability of the extended prediction, needs more detailed study based on various event types in order to confirm the proposed ensemble forecasting method.

References

Davis, M. W. (1987): Generating large stochastic simulation-The matrix polynomial approximation method, Mathematical Geology, Vol. 19, No. 2, pp. 99-107.

Drosdowsky, W. and Zhang, H. (2003): Chapter 6. Verification of Spatial Fields, *Forecast Verification: A Practitioner's Guide in Atmospheric Science*, Edited by Jolliffe, I. T. and Stephenson, D. B., 2003 John Wiley & Sons.

Du, J. and Mullen, S. L. (1997): Short-range ensemble forecasting of quantitative precipitation, Monthly Weather Rev., Vol.125, pp. 2427-2459.

Epstein, E. S. (1969): Stochastic dynamic prediction, Tellus, Vol 21, pp. 739-759.

Ichikawa, Y., Tachikawa, Y., Takara, K. and Shiiba, M. (2000): Object-oriented hydrological modeling system, Proceedings of Hydroinformatics 2000.

Kim, S., Tachikawa, Y. and Takara, K. (2005): Real-time prediction algorithm with a distributed hydrologic model using Kalman filter, Annual of Hydraulic Engineering, JSCE, Vol. 49, pp. 163-168.

Kim, S., Tachikawa, Y. and Takara, K. (2006): Ensemble rainfall-runoff prediction with radar image extrapolation and its error structure, Annual of Hydraulic Engineering, JSCE, Vol. 50, pp. 43-48.

Krzysztofowicz, R. (2001): The case for probabilistic forecasting in hydrology, Journal of Hydrology, Vol 249, pp. 2-9.

Leith, C. E. (1974): Theoretical skill of Monte Carlo forecasts, Monthly Weather Rev., Vol.102, pp. 409-418.

Lorenz, E. N. (1969): Atmospheric predictability as revealed by naturally occurring analogues. J. Atmos. Sci., Vol. 26, pp. 636-646.

Sayama, T., Tachikawa, Y., Takara, K. and Ichikawa, Y. (2005): Development of a distributed rainfall-runoff prediction system and assessment of the flood control ability of dams, J. Hydraul. Coastal and Environm Eng. JSCE, Vol. II-73, (in printing).

Tachikawa, Y. and Shiiba, M. (2000): Gaussaian and log normal random field generation based on the square root decomposition of a covariance matrix, J. Hydraul. Coastal and Environm. Eng., JSCE, Vol.656 (II-52), pp. 39-46.

Chapter 4

Updating of State Variables in a Distributed Hydrologic Model

Over the last several decades, there has been more progress in computing, and developments of distributed models, than in field measurement techniques (Beven, 2002). Current hydrology suffers from a measurement problem especially with the distributed properties of catchments, such as water levels and soil moisture at every point of a basin.

However, it is unrealistic to define the detailed spatial distribution of catchment properties through extensive field measurement, as such a process is too costly and time-consuming. Except for few specially designed catchments studied for a specific purpose, outlet discharge is the only commonly available observation in a given catchment. To reflect a low-resolution observation into a detailed spatial resolution for a distributed hydrologic model, an effective method is needed to estimate and update the distributed catchment properties.

To minimize the discrepancy between simulation and observation, correcting the model internal state variables is the most commonly used updating scheme in real-time simulation. However, in updating the measurement for a distributed hydrologic model, not only the magnitude of the state variable but also its spatial distribution pattern should be considered. During runoff simulation, inappropriate rearrangement of the spatial distribution of state variables produces obvious effects on the runoff simulation results (Kim *et al.*, 2004; Kim *et al.*, 2005).

This chapter describes a distributed hydrologic model, CDRMV3 (Kojima *et al.*, 2003), and discusses updating methodologies of distributed state variables in the model. To avoid an unpredictable collapse of the internal model state during a simulation, the update method introduced in this study retains the spatial distribution pattern of the state

variables. This is executed before and after the updating by using a ratio of total storage amount or outlet discharge. The main purpose of updating the state variables is for coupling the Kalman filter algorithm into a distributed hydrologic model.

4.1 Distributed Hydrologic Model, CDRMV3

The model used here is known as the Cell-based Distributed Runoff Model Version 3 (CDRMV3; Kojima *et al*., 2003). The CDRMV3 is a physically based distributed hydrologic model developed at the Disaster Prevention Research Institute of Kyoto University, Japan. The model solves the one-dimensional kinematic wave equations for both subsurface flow and surface flow using the Lax–Wendroff scheme on every computational node in a cell. Discharge and water depth diffuse to the steepest downward adjacent cell according to a flow direction map generated from DEM data.

Kinematic wave modeling, not only for channel routing and overland flow but also for subsurface flow has been widely used in distributed flow computations because of its simplicity and computational efficiency (see Singh, 2001; Reed *et al*., 2004). A good example of kinematic wave modeling simulating the flow of the subsurface in unsaturated and saturated zones is presented in Beven (1982) with a comparison in field observations.

Takasao and Shiiba (1988) analyzed the interaction between surface and subsurface flow on convergent/divergent slopes using kinematic wave equations with a stage discharge relationship with consideration towards surface and subsurface flow generation. Tachikawa *et al*. (2004) extended the concept to include unsaturated subsurface flow, and this extended stage discharge relationship was incorporated into CDRMV3.

The capillary pore layer of depth d_c provides simulation of unsaturated flow. After the water depth reaches d_c the capillary pore layer is assumed saturated and gravity flow occurs in the non-capillary pore layer. Since the total depth of the subsurface flow layer

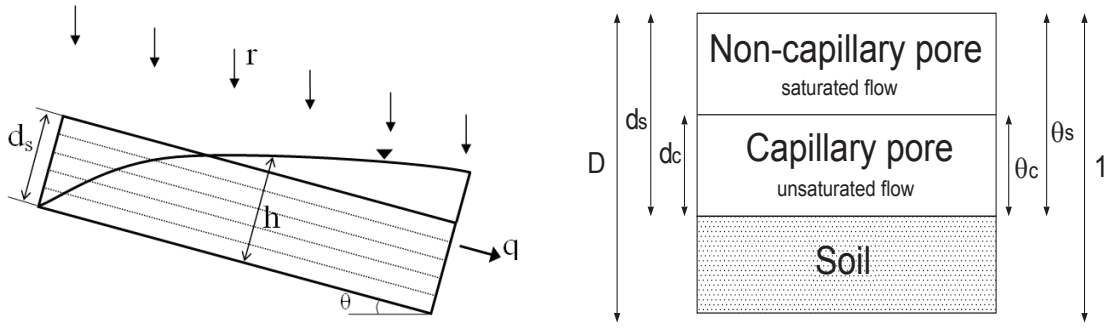

Figure 4.1 Schematic illustration of the water flow within soil layer in CDRMV3.

is d_s, the depth of the saturated soil layer is $d_s - d_c$. After the water depth exceeds d_s, surface flow begins. Within the soil layer, the flow lines are assumed to be parallel to the slope, and the hydraulic gradient is assumed equal to the slope. In mountainous areas with steep slopes, it is reasonable to assume that the flow streamlines are parallel to the slope (Beven, 1981).

In each slope segment, rainfall is directly added to subsurface or surface flow according to the water depth on each point in the basin. Rather than including a vertical infiltration model with additional model parameters that cannot be directly measured, the stage discharge relationship effectively simulates lagged subsurface flow with calibrated soil depths and hydraulic conductivities.

The continuity equation for each slope segment is written as:

$$\frac{\partial h}{\partial t} + \frac{\partial q}{\partial x} = r(t)\cos\theta \tag{4.1}$$

where h is water depth and q is discharge per unit width; t and x are time and distance along water flow, respectively, and $r(t)$ is the rainfall amount on a node at time t. To define the relationship between h and q, a stage–discharge relationship incorporating the saturated and unsaturated subsurface flows as well as the surface flow (Tachikawa *et al*., 2004) is adopted.

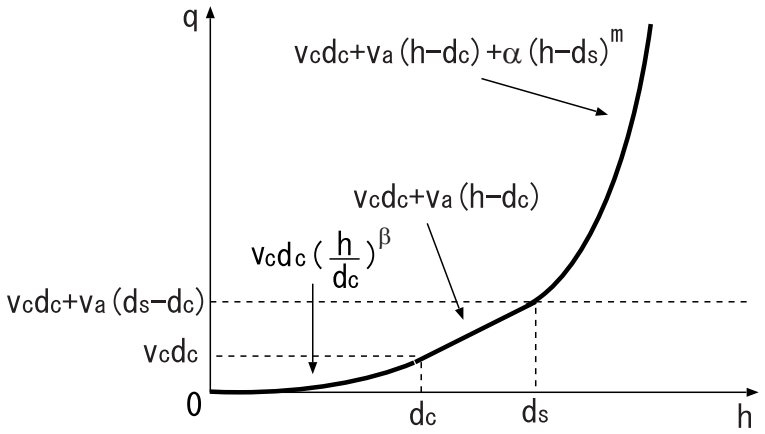

Figure 4.2 Relationship between water depth and discharge per unit width in CDRMV3.

This relationship is expressed by three equations as shown in Figure 4.2, one applying to each water level. When water depth h is less than the depth of the capillary pore layer d_c ($0 \le h < d_c$), flow is described by Darcy's law with a degree of saturation $(h/d_c)^{\beta}$ and saturated velocity v_c (= k_{ci}). Here, β is the degree of saturation ratio, k_c is saturated hydraulic conductivity in the capillary layer, and i is the slope gradient. If h increases ($d_c \le h < d_s$), the velocity of flow from the non-capillary pore layer is expressed as v_a (= k_{ai}), where k_a is the saturated hydraulic conductivity in the non-capillary layer. When the water depth is greater than that of the soil layer ($d_s \le h$), overland flow is added using Manning's resistance law. The equations relating discharge per unit width q to water depth h are formulated as Equation 4.2:

$$q(h) = \begin{cases} v_c d_c \left(h / d_c\right)^{\beta}, (0 \le h < d_c) \\ v_c d_c + v_a \left(h - d_c\right), (d_c \le h < d_s) \\ v_c d_c + v_a \left(h - d_c\right) + \alpha \left(h - d_s\right)^m, (d_s \le h) \end{cases} \tag{4.2}$$

where $\alpha = i^{1/2}/n$, $m = 5/3$, and n is Manning's roughness coefficient.

$$c = \frac{\partial q}{\partial h} = \begin{cases} \beta v_c \left(h / d_c\right)^{\beta - 1}, (0 \le h < d_c) \\ v_a, (d_c \le h < d_s) \\ v_a + m\alpha \left(h - d_s\right)^{m-1}, (d_s \le h) \end{cases} . \tag{4.3}$$

Model parameters in the stage–discharge relationship are d_c, d_s, k_c, k_s and n. The kinematic wave celerity c for each layer is given in Equation 4.3, and β (= v_a/v_c) is determined by the continuity condition on the wave celerity. This specific stage discharge relationship characterizes the distributed hydrologic model CDRMV3. Each cell has its own stage discharge relationship determined by topography, land use, and soil type.

4.2 Updating of Distributed State Variables

During runoff simulation, inappropriate rearrangement of the spatial distribution of state variables produces obvious effects on the runoff simulation results (Kim *et al*., 2004). Figure 4.3 shows one clear example of the negative effects produced when the state variables are reset uniformly as the initial condition setting in CDRMV3. The resetting of the state variables was carried out by means of using the outlet discharge 72 hrs after the beginning of the simulation. After the reset, the spatial pattern of the state variables in the model is setaside and the results of resetting the spatial distribution pattern causes a poor simulation result.

To avoid an unpredictable collapse of the internal model state during a simulation, the update method used maintains the spatial distribution pattern of the state variables before and after updating (see Figure 4.4). Only the total amount of the state variables was updated by multiplying the variables by a specific factor. This factor was calculated from the ratio of the total storage amount, estimated from observed discharge, and the simulated total storage amount. Since the simulated water depth on every computation node in the model was multiplied by the calculated factor, the model was able to retain the spatial distribution pattern of the internal state variables.

This factor application, named ratio method, can be classified into two separate methods by the way of factor calculation. One is the *S*-ratio method using a ratio of total storage amount in the basin and the other is the *Q*-ratio method using a ratio of discharge at the outlet of the basin.

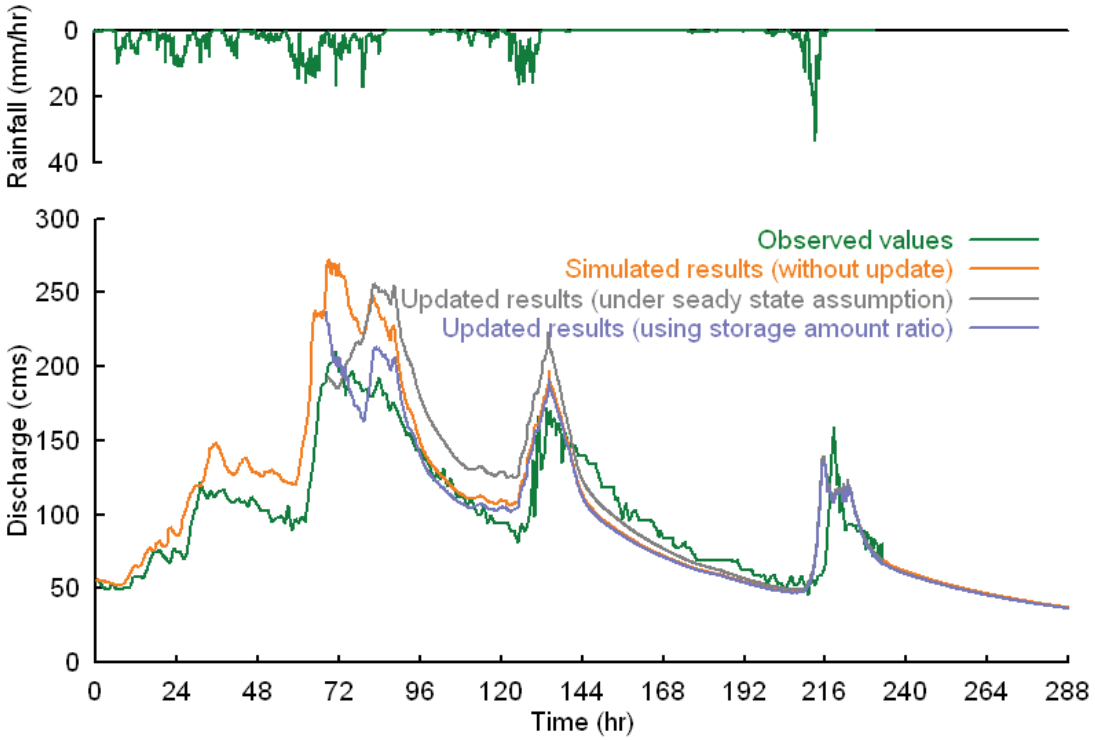

Figure 4.3 Comparison of two updating method; steady state and storage amount ratio.

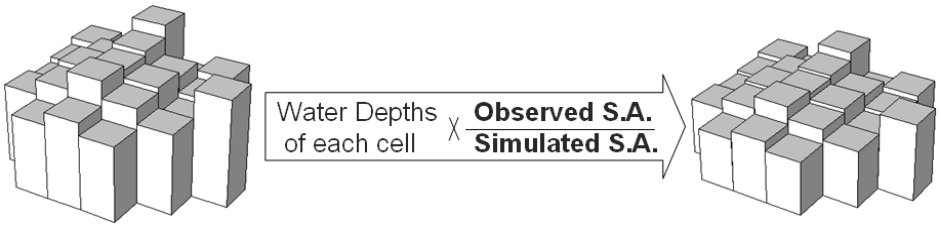

Figure 4.4 Resetting of state variables using the ratio of storage amounts.

4.2.1 S-ratio Method

If a difference between observed discharge and simulated discharge at the outlet of the basin exists, it can be assumed that it is caused by incorrect total storage amounts in the model. When a storage amount is considered as a state variable, a relationship between discharge Q, and storage S can be established. The nonlinear Q-S relationship, as defined in equation 4.4 is generally used.

$$S(t) = KQ(t)^{P} \tag{4.4}$$

where $S(t)$ is storage amount in a basin and $Q(t)$ is discharge of the outlet at time step t. K and P values are parameters for he relationship of the S and Q.

Based on the nonlinear Q-S relationship, the S-ratio method uses the ratio of total storage amount in the subject basin, which is calculated from simulated and observed discharges. To calculate the ratio of total storage amount, both the simulated and observed storage amounts must be acceptably accurate. A simulated total storage amount in a model is easily calculated from the water depth on each grid cell by multiplying by its cell area.

However, because the total storage amount cannot be measured directly, the corresponding total storage amount must be estimated from the observed discharge, assuming there is a discharge–storage relationship. To relate discharge at the basin outlet Q and the total storage amount S, the Q–S relationship under a steady-state assumption was established. Applying a constant rainfall intensity over the study basin until it reached a steady state, one pair of total storage amount and discharge was acquired from the CDRMV3. Through variable rainfall intensities, the Q–S relationship, as shown in Figure 4.5, was obtained at the Kamishiiba catchment.

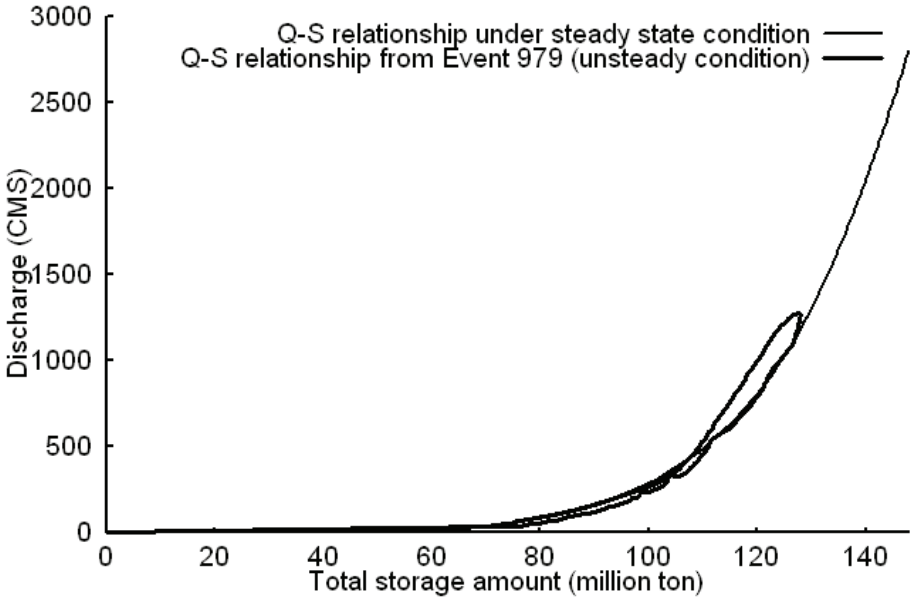

Figure 4.5 Discharge storage relationships under a steady-state and from Event 979.

A runoff simulation under unsteady-state conditions produced a loop-shaped Q–S relationship (thicker solid line in Figure 4.5), and the produced curve appeared to differ from event to event, however the difference of the total storage amount obtained from the curves of the steady-state and unsteady-state condition was not significant. Moreover, instead of direct conversion of observed discharge to the storage amount, the storage amount $S_{o,t}$ at time step t was obtained as

$$S_{o,t} = S_{s,t} + H\left(Q_{o,t} - Q_{s,t}\right) \tag{4.5}$$

where $S_{s,t}$ and $Q_{s,t}$ are total storage amount and the outlet discharge simulated by the model at time step t. $Q_{o,t}$ is the observed discharge at the outlet, and H is the mean of the gradient values on the Q–S relationship at the point defined by $S_{s,t}$ and $Q_{s,t}$. The calculated total storage amount $S_{o,t}$ from Equation 4.5 was regarded as the observed total storage amount. From the Q–S relationship, two H values were obtained, which were essentially different: one came from the simulated discharge $Q_{s,t}$ and the other from the simulated storage amount $S_{s,t}$. Through several test simulations, it is found that those two H values did not produce a recognizable difference in the filtered results. Thus, an arithmetic average of those two H values was used in the application.

Since the calculated ratio from the storage amounts represented the ratio of average water depth in the catchment, this ratio was applied to the simulated water depth on every grid cell to rearrange the distributed storage amount. After this procedure, the updated water depths were equivalent to the storage amount $S_{o,t}$ estimated from the observed discharge. The spatial distributed pattern of water depth contained the predicted water storage pattern before updating, and the pattern reflected the spatial distribution of rainfall and topographic properties.

4.2.2 Q-ratio Method

The second way to reset the distributed storage amount is by applying a ratio of discharge difference at the outlet to the discharge of every point in a basin. This concept is under an assumption that every discharge in a basin would increase or decrease with

the same ratio according to the discharge change in the outlet. The assumption is reasonable when considering a steady state basin.

In the CDRMV3, water depth and discharge on every cell are simulated based on the kinematic wave equation, and those two values are convertible at each calculation time step by the specified stage-discharge relationship on each grid cell. If every discharge is reset by the ratio '$R=Q_s/Q_o$' as shown in the Figure 4.6, each water depth would also be reset by its own stage discharge relationship. The updating of the discharge means the water depth, too, is updated which finally results in the storage amount reformation.

Figure 4.6 shows the schematic drawing of discharge and water depth profile updating at the ideal one dimensional basin with the *Q*-ratio and the stage discharge relationship. While every updated discharge has the same ratio of discharge before updating at each point, the ratio of water depth will be different by each point because of the topographic and physical characteristic of each cell, such as slope and roughness coefficient.

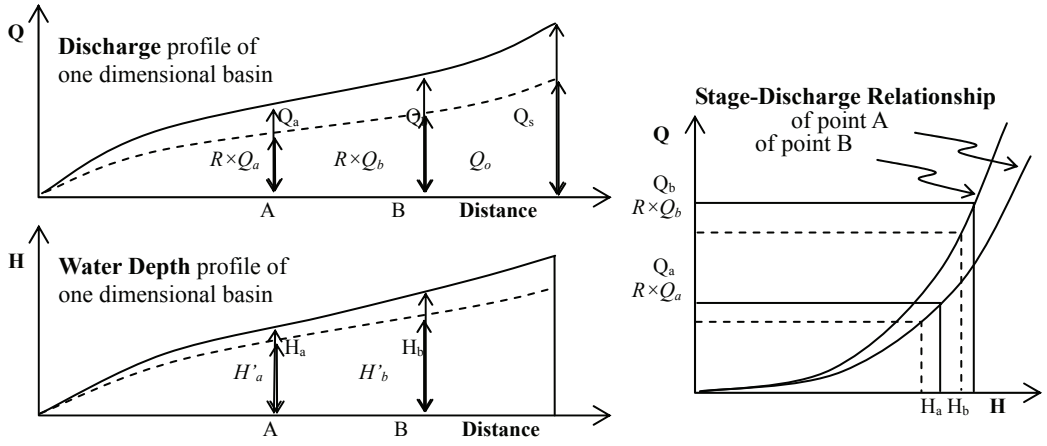

Figure 4.6 Q-ratio application examples to the ideal one dimension basin.

The *Q*-ratio method has several merits compared to *S*-ratio methods: 1) A characteristic stage discharge relationship of each cell can reflect topographic and physical character of cell, 2) Steady state assumptions of *Q*-*S* relationship are not needed to acquire an observed storage amount, and 3) Can efficiently get the ratio and update.

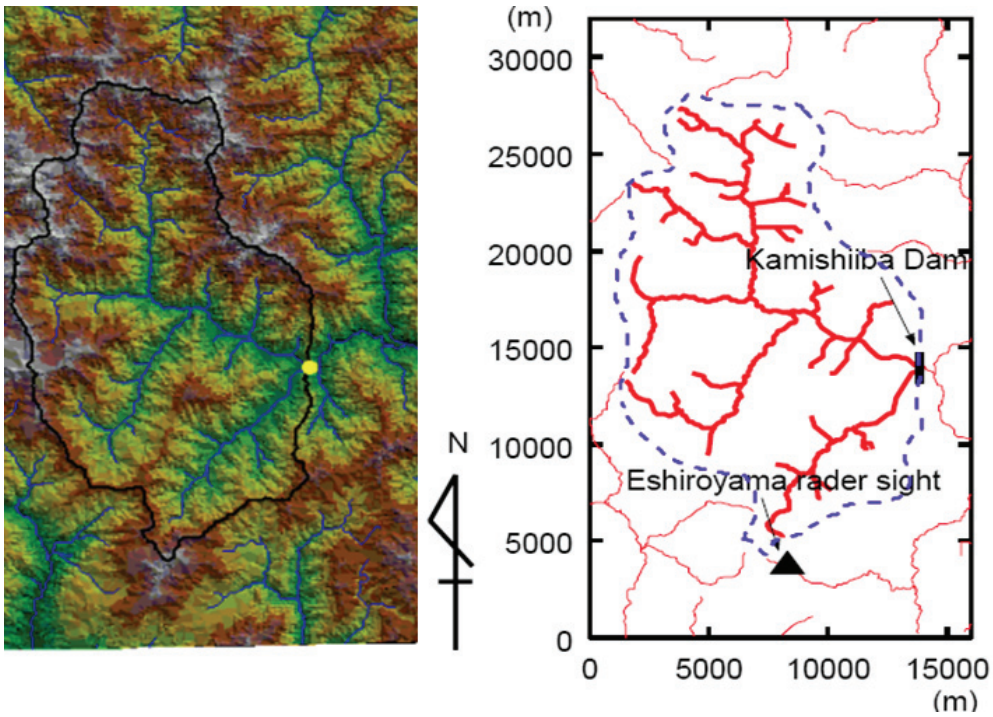

Figure 4.7 Catchment boundary and channel network of Kamishiiba basin.

4.3 Application Results and Discussion

The CDRMV3 model was applied to the Kamishiiba basin (211 km^2) in the Kyushu, Japan (see Figure 4.7). The selected flood events are shown in Table 4.1 with the Nash coefficient, which is used for checking the model performance efficiencies.

Table 4.1 Flood events used in this study and Nash coefficients.

EVENT	Flood Term	Max Q	*N.S.*
Event 979	15–19 September 1997	1203.0 m^3/s	0.988
Event 996	24 June–3 July 1999	210.0 m^3/s	0.698
Event 998	1–7 August 1999	489.0 m^3/s	0.962
Event 999	22–27 September 1999	644.0 m^3/s	0.919

The parameters given in Table 4.2 were mainly calibrated from Event979, and an identical parameter set was used for the other events. There is only one type of land use (forest: n = 0.30) in the Kamishiiba basin, and the cells in the upper area, of which there are more than 500, are assumed to be river cells (n = 0.025).

Table 4.2 Parameter set of CDRMV3 for Kamishiiba basin.

d_a (m)	d_m (m)	K_a (m/s)	$\beta = k_a/k_m$	n (m^3/s)
0.55	0.45	0.01	4.0	0.30 (0.025)

The initial water depth at each slope was determined under the steady state assumption. Given the initial discharge at the basin outlet, the discharge from every grid cell was assigned in proportion to each of the grid cells upstream to it. The assigned discharge in each cell was converted to the value of the water depth by the stage discharge relationship. This water depth and discharge in each cell served as the initial soil moisture distribution for the following rainfall–runoff simulation.

The state variable to be updated stood for the total amount of storage in the basin, and the spatial distribution of water depth was recalculated based on this updated storage amount. As the simulation proceeded, the total amount of storage could easily be calculated by multiplying the water depths at every computational node by the cell area and adding up the entirety of the values in the basin. During this procedure, the parameters were not changed. Radar-observed rainfall data, calibrated by ground gauges, were used as forecast rainfall data. This rainfall data became available every 10 minutes, after which the distributed hydrologic model produced its simulation results with a time increment of 10 min.

Figures 4.8 and 4.9 show the comparison of results from the three ratio methods. When the results are compared, generally the *Q*-ratio method shows a positive relativity with observed discharge. To check the quantitative updating efficiency, root mean square error (*RMSE*) is calculated as:

$$RMSE = \sqrt{\frac{\sum_{i=1}^{N} (Q_{s,t} - Q_{o,t})^2}{N}} \tag{4.6}$$

where Q_S is discharge from the ratio method, Q_O is observed discharge, and N is the number of Q_S and Q_O values.

Table 4.3 The ratio of storage amount and discharge.

Event	Discharge & Storage-amount	R_S	R_Q
Event 979 (38th hr)	$\frac{249.00}{349.24} \rightarrow \frac{0.97292\times108}{1.03476\times108}$	0.9402	0.7130
Event 979 (47th hr)	$\frac{640.00}{788.69} \rightarrow \frac{1.15252\times108}{1.19596\times108}$	0.9637	0.8115
Event 996 (57th hr)	$\frac{100.00}{121.85} \rightarrow \frac{0.81944\times108}{0.86443\times108}$	0.9480	0.8207
Event 996 (68th hr)	$\frac{191.17}{267.44} \rightarrow \frac{0.92619\times108}{0.97295\times108}$	0.9519	0.7148

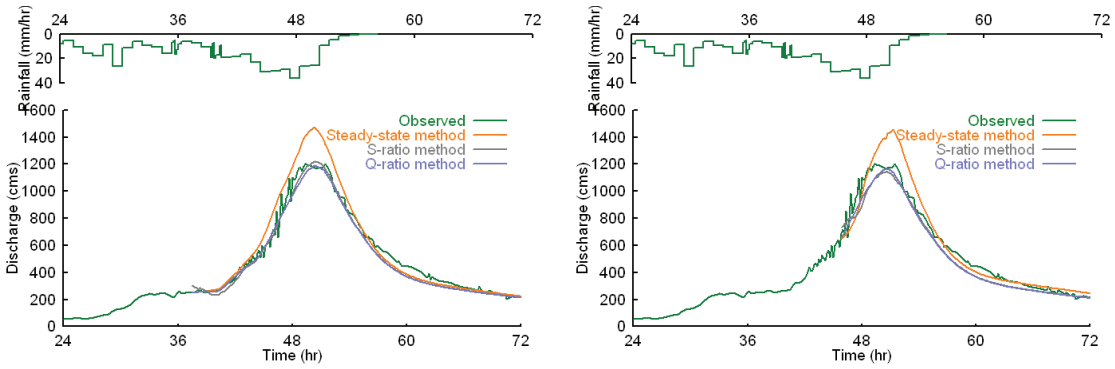

Figure 4.8 Updating results comparison for two Ratio-methods (Event979).

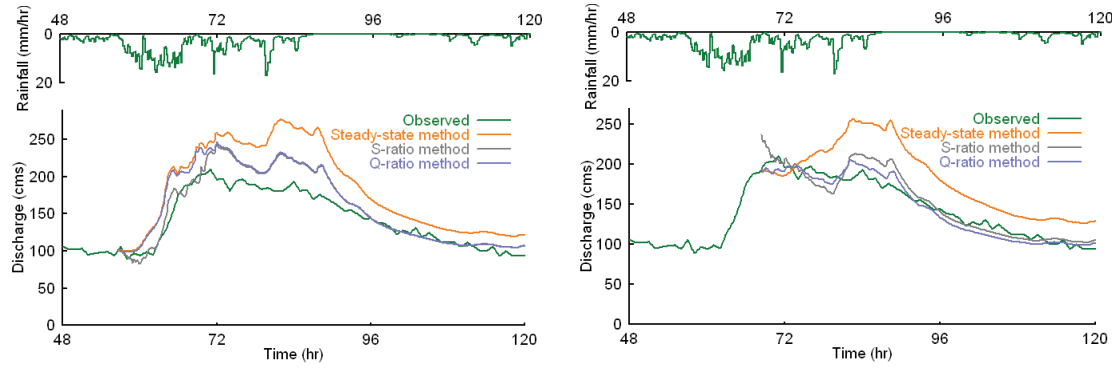

Figure 4.9 Updating results comparison for two Ratio-methods (Event996).

Table 4.4 shows the *RMSE* of each time step after updating. Both the *S*-Ratio and *Q*-Ratio method show optimistic values compared to the values of the steady state method. According to Table 4.5, the *RMSE* values of a 6 hrs period after updating exemplify that of the *Q*-Ratio method which can thus be said to be the most efficient method for updating state variables in a distributed hydrological model. Furthermore, the *Q*-Ratio method is the most straightforward in updating state variables.

Table 4.4 Root Mean Square Error –Every time step after updating.

	Steady-state	*S*-Ratio	*Q*-Ratio
Event 979 (38th hr)	62.777	31.801	32.633
Event 979 (47th hr)	63.046	41.740	39.036
Event 996 (57th hr)	37.485	29.703	30.612
Event 996 (68th hr)	36.142	29.152	28.677

Table 4.5 Root Mean Square Error –6hr period after updating.

	Steady-state	*S*-Ratio	*Q*-Ratio
Event 979 (38th hr)	18.132	30.574	11.451
Event 979 (47th hr)	160.941	108.356	90.599
Event 996 (57th hr)	18.376	6.449	17.017
Event 996 (68th hr)	13.409	15.033	10.239

In this chapter, three different types of methods for updating state variables were tested: the steady state method and two kinds of ratio methods. Though the steady state method proved to be the simplest way to update state variables, it is not an appropriate one to update a spatial distribution of the variables in a distributed hydrological model. Furthermore, during a runoff simulation, ignorance of distributed spatial patterns of state variables causes severe collapse of simulation behavior.

The *S*-Ratio method showed improved simulation results upon updating. The *Q*-*S* relationship under a steady state assumption was found necessary in order to produce a storage amount corresponding to an observed discharge, which may also lead to unexpected error in the *S*-Ratio method. With the *Q*-ratio method, a successful updating of the state variables becomes simple and effective. The stage-discharge relationship of each cell reflect topographic and physical characteristics of each cell during the update.

It is possible to improve real-time forecasting accuracy if the updating method introduced here is conjoined with a data assimilation scheme, and if new observed data is available for several steps of updating. Figure 4.10 shows improved forecasting accuracy by the three steps of *Q*-Ratio updating with observed data. This case can be

regarded as one type of data assimilation when the observed data is believed to be of a true value. However, as the uncertainty in the observation should be highly considered, it will therefore be discussed in the next chapter.

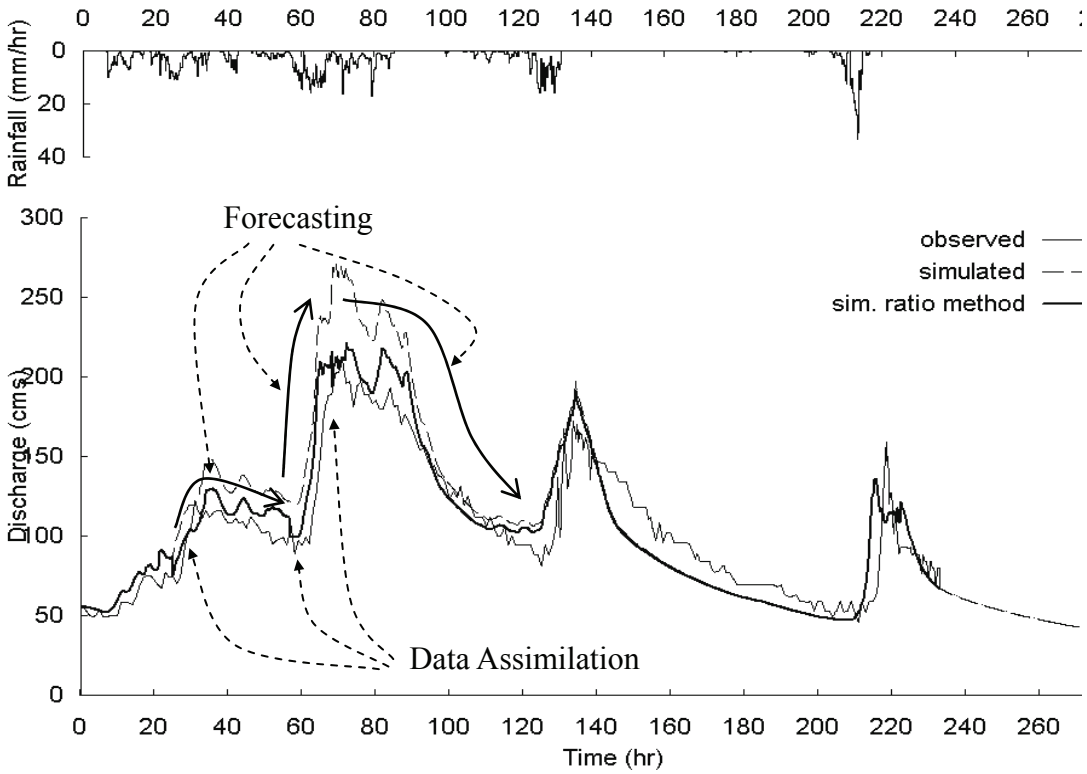

Figure 4.10 Expected result from a multi-step updating by use of S-ratio method.

References

Beven, K. (1981): Kinematic subsurface stormflow, Water Resources Research, Vol. 17, No. 5, pp. 1419-1424.

Beven, K. (1982): On Subsurface Stormflow: Predictions with simple Kinematic theory for saturated and unsaturated flows, Water Resources Research, Vol. 18, No. 6, pp. 1627-1633.

Beven, K. (2002): Towards an alternative blueprint for a physically based digitally simulated hydrologic response modeling system, Hydrological Processes, Vol. 16, pp. 189-206.

Kim, S., Tachikawa, Y. and Takara, K. (2004): Real-time updating of state variables in a distributed hydrologic model, Annuals of DPRI, Kyoto University, No. 47B, pp. 273-282.

Kim, S., Tachikawa, Y. and Takara, K. (2005): Real-time prediction algorithm with a distributed hydrologic model using Kalman filter, Annual of Hydraulic Engineering, JSCE, Vol. 49, pp. 163-168.

Kojima, T. and Takara, K. (2003): A grid-cell based distributed flood runoff model and its performance, Proceding of symposium HS03, Weather radar information and distributed hydrological modeling, IAHS Publ. No. 282, pp. 234-240.

Reed, S., Koren, V., Smith, M., Zhang, Z., Moreda, F., Seo, D. J. and DMIP Participants. (2004): Overall distributed model intercomparison projects results, Journal of Hydrology, Vol. 298, pp. 27-60.

Singh, V. P. (2001): Kinematic wave modelling in water resources: a historical perspective, Hydrological Processes, Vol. 15, pp. 671-706.

Takasao, T. and Shiiba, M. (1988): Incorporation of the effect of concentration of flow into the Kinematic wave equations and its applications to runoff system lumping, Journal of Hydrology, Vol. 102, pp. 301-322.

Tachikawa, Y., Nagatani, G. and Takara, K. (2004): Development of stage-discharge relationship equation incorporating saturated-unsaturated flow mechanism, Annual Journal of Hydraulic Engineering, JSCE, Vol. 48, pp. 7-12, (Japanese with English abstract).

Chapter 5

Embedding Kalman Filter into a Distributed Hydrologic Model

> "By adding stochastic noise components to both the dynamic and observation equations, the model accounts for measurements errors (in observations and inputs) and errors in model structure and model parameters. If the observations are taken at discrete times, the end result is a state-space representation of a stochastic nonlinear rainfall-runoff model." (Puente and Bras, 1987)

R.E. Kalman (1960) developed a recursive optimization algorithm, later called the Kalman filter, for linear filtering problems. To exploit its potential for wider application, this filter has been enhanced as the extended Kalman filter for nonlinear systems. The filter combines all the available observation data, and incorporates prior knowledge about the system and measuring devices to produce estimates of the required variables in such a manner that the error is statistically minimized (Maybeck, 1979). In the last several decades, many hydrologists have applied Kalman filter into hydrological systems for an improved model performance in real-time forecasting of river flows (*e.g.* Takasao *et al.*, 1989). However, most applications were limited to conceptual hydrologic models and few researches were available with a distributed hydrologic model.

The objective of this chapter is to couple the Kalman filter with a distributed model, CDRMV3, and test the performance of the coupled model on a real-time basis. The CDRMV3 using the Kalman filter not only yielded better results than non-filtering simulations but also presented the reliability of the performances and can thus be used as a probabilistic forecast algorithm (Kim *et al.*, 2005). The developed algorithm can incorporate the uncertainty of input and output measurement data as well as the uncertainty in the model itself.

5.1 Kalman Filter in Hydrology

Accurate flood forecasting on a real-time basis has long been the principal aim of many hydrologists, and a large number of rainfall–runoff models have been developed and applied toward forecasting problems. In operational hydrology, real-time forecasting requires not only well developed rainfall–runoff models, but also a method for continuous adjustment of the forecast based on the error observed from earlier forecasts (Nash and Sutcliffe, 1970). This continuous correction, with real-time measurement and updating, is one of the most valuable schemes for improving the forecasting performance of any rainfall–runoff model. Many studies over the last several decades have shown the effectiveness of filtering methods in applying this continuous correction.

Hino (1973) was among the first to adopt a filtering theory for use with a hydrologic system by applying a recursive estimation approach to the problem of real-time river runoff forecasting. Several papers have discussed recursive real-time parameter estimation for conceptual hydrologic systems (e.g., Wood and Szöllösi-Nagi, 1978; Cooper and Wood, 1982; Puente and Bras, 1987; Rajaram and Geogakakos, 1989; Lee and Singh, 1999).

The Kalman filter (Kalman, 1960) has been the most widely used algorithm for recursive updating. It is still believed that there is no reason to fix the model structure throughout all time steps and to ignore newly observed data. For comparatively simple conceptual rainfall–runoff models, adjusting inappropriate model structure is reasonable and even necessary for simulation of the nonlinear behavior of hydrologic systems.

However, as Kitanidis and Bras (1980b) pointed out, most of the proposed hydrologic systems using recursive update algorithms have been achieved at the expense of employing oversimplified models. The recursive calibration of model parameters based on the output measurements has been somewhat overemphasized, while the use of more sophisticated and physically based models, which can be used to correctly project into

the future, has been overlooked. This is a kind of hydrologist's trade-off for incorporating the filtering concept into the hydrologic model. The Kalman filter, which is the most representative recursive data processing algorithm, requires linearized equations for the system dynamics and a linear observation function related to the system states. These requirements have deterred many hydrologists from applying filtering theory in a physically based distributed hydrologic system.

Current data availability, such as the use of digital elevation models (DEM) and radar observation of rainfall, together with exponential increases in computer data storage and processing speed, have allowed hydrologists to study watershed behavior at remarkably small scales and to use physically based process equations. Under these conditions, considerable research effort has been directed toward the development of distributed hydrologic models by solving the numerous and complex physically based equations (Smith *et al*., 2004). However, the usefulness of the recursive measurement updating method in operational hydrology has not diminished, even for a state-of-the-art distributed hydrologic model, since the model is still based on a deterministic system.

Recent trends in flood forecasting have been diverging from deterministic forecasts and heading toward probabilistic forecasts, accepting their prediction uncertainties. A deterministic forecast gives a point estimate of the predicted values, such as river stages/discharges; thus, it may create the illusion of certainty in a user's mind and cause immense losses of property and/or one's life as a result of a wrong decision caused by overconfidence (Krzysztofowicz, 2001). However, a probabilistic forecast provides a certain probability distribution for the predicted values. The predictive probability can be assigned a numerical measure of reliability, such as the mean and variance of discharge, by means of, for example, a hydrologic model incorporating the Kalman filter.

Hence, it is now appropriate to consider utilizing the filtering concept with a distributed hydrologic model; much more flexible and improved performance can be anticipated when the model is applied on a real-time basis to varying nonlinear catchments.

5.2 Kalman Filter Application into CDRMV3

For the incorporation of the filtering concept into a distributed model, there are several hurdles to be overcome. First, linearized equations for the system dynamics are necessary for projecting the state variables and their error covariance in the Kalman filter. The Monte Carlo simulation method makes it possible to project the nonlinear variation of system states and their error covariance without the need for linearized system equations. Evensen (1994) has shown that Monte Carlo methods permit the derivation of forecast error statistics in the Kalman filter algorithm, and thus, the inefficiency involved in the linearization of system states can be eliminated.

Second, as an alternative to the linear observation function, this study introduced an external relationship of observed data and the internal state variables of the hydrologic model. Here, the observed data are outlet discharge and the state variable in the Kalman filter algorithm is the total amount of storage in the basin. Rather than inputting a linear function of the observation and the system states into the Kalman filter, a table of those two sets of values successfully defines the nonlinear interaction in the updating algorithm.

The last problem to be considered was how a very large number of state variables, which are usually based on the fine grid cells of a distributed hydrologic model, can be updated at the same time without a excessive computational burden. A simple but very efficient method using a ratio of the state variables makes it possible to solve this restriction of the application with the Kalman filter for a distributed hydrologic model. The Kalman filter algorithm updates the total amount of storage in the basin, and a ratio of the updated and simulated storage amount is calculated and applied to each of the internal state variables on a fine grid cell.

The Kalman filter algorithm consists of two parts: a measurement update algorithm for the assimilation of observed data into the system state variables, and a time update algorithm for predicting simulated state variables and their error covariance. The

following sections illustrate these two parts in relation to coupling with the distributed hydrologic model CDRMV3.

5.2.1 Measurement Update Algorithm

In the measurement update algorithm of the Kalman filter, an observation vector y_k at time step k is described as a linear vector function of a state vector x_k, and observation noise vector w_k assuming white noise is included in the observation as:

$$y_k = H_k x_k + w_k, \quad w_k \sim N(0, R_k), \tag{5.1}$$

which has an error covariance matrix R_k. The $m \times n$ matrix H relates the state vector to the observation. The state variables are updated as follows:

$$\hat{x}(k|k) = \hat{x}(k|k-1) + K_k(y_k - H_k\hat{x}(k|k-1)) \tag{5.2}$$

$$P(k|k) = P(k|k-1) - K_k H_k P(k|k-1) \tag{5.3}$$

$$K_k = P(k|k-1)H_k^T(H_k P(k|k-1)H_k^T + R_k)^{-1}. \tag{5.4}$$

The difference, $y_k - H_k\hat{x}(k|k-1)$, which is called the residual or innovation, reflects the discrepancy between the estimated observation $H_k\hat{x}(k|k-1)$ and the actual observation y_k. In the measurement update algorithm, the state vector $\hat{x}(k|k-1)$ and its error covariance vector $P(k \mid k–1)$ as estimated at time step k–1, are updated by use of the $m \times n$ matrix K_k at time step k. The matrix K_k, called Kalman gain, is chosen to minimize the updated error covariance P($k \mid k$). In the algorithm, the superscript '^' indicates estimated value and '^{T}' indicates the transpose of a matrix.

Here, the observation equation is the *Q*–*S* relationship shown in Figure 4.5; thus, the scalar value of H represents the gradient of the *Q*–*S* relationship using the simulated results at the updating time step. The results from the measurement update algorithm were used to update the total storage amount of the study basin and its error variance. With the updated watershed storage amount, the ratio method described in the previous

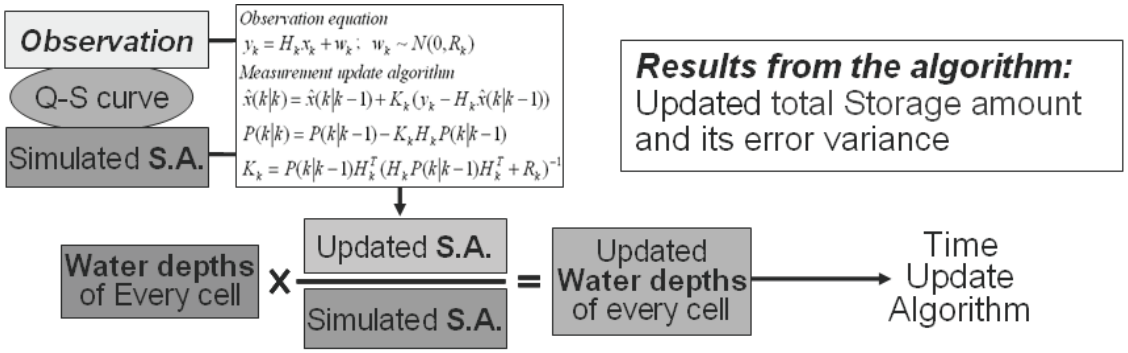

Figure 5.1 Illustration of the measurement update algorithm using the ratio method.

section was used to update the spatial distribution of water depth in the distributed hydrologic model. The flow of measurement update algorithm using the *Q*-*S* curve and *S*-ratio method is presented in Figure 5.1.

5.2.2 Time Update Algorithm

The $n \times n$ matrix F in the system equation relates the state variables x at the current time step k to those at the next step $k+1$ as:

$$x_{k+1} = F_k x_k + B_k + v_k;\ \ v_k \sim N(0, Q_k) \tag{5.5}$$

The system is continuously affected by white Gaussian system noise, v_k, with system error covariance matrix Q_k. The matrix B_k provides optional control input to the state x. The time update algorithm

$$\hat{x}(k+1|k) = F_k \hat{x}(k|k) + B_k \tag{5.6}$$

$$P(k+1|k) = F_k P(k|k) F_k^T + Q_k \tag{5.7}$$

is used to project forward the current state and the $n \times n$ error covariance to obtain estimates for the next time step.

In the CDRMV3, a complicated relationship exists between the present and the next time-step state variable, *i.e.*, the present and the next time-step total storage amount. The

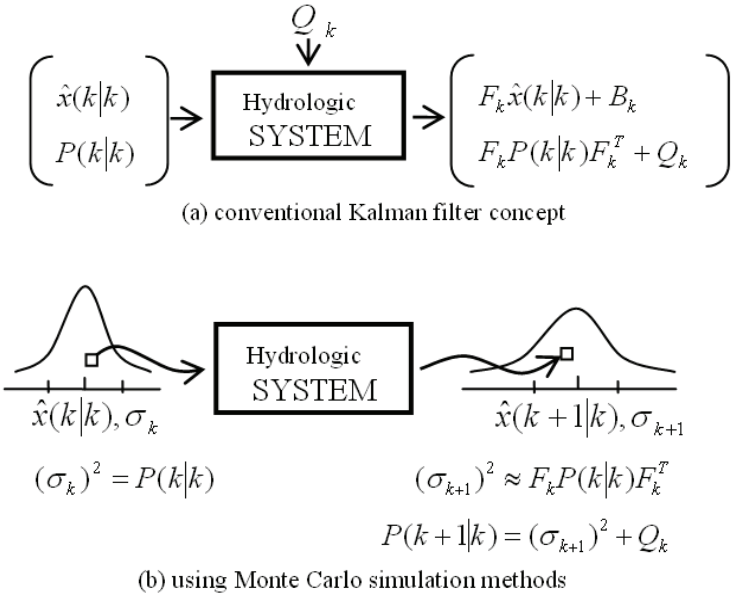

Figure 5.2 Schematic drawing of time update algorithm (a) of the conventional Kalman filter concept and (b) using Monte Carlo simulation methods.

current water depth at each cell responds interdependently to the next step's water depth according to the current spatial distribution of water depth and rainfall input.

It is impractical to define the system matrix F_k to formally express this process from the hydrologic system equations as shown in the schematic drawing in Figure 5.2 (a); instead, a Monte Carlo simulation (drawing (b) in Figure 5.2) was applied to solve this problem. Many random variables were generated at time step k; and used to generate 100 total storage amount values within the range of the probability distribution, $N(\hat{x}(k|k), \sigma_k)$, where $\sigma_k = P(k \mid k)^{0.5}$.

The ratio method was then used to rearrange the spatial distribution of the each water stage at each cell by multiplying the ratio of each generated storage amount to the updated storage amount $\hat{x}(k|k)$. After 100 simulations, the probability distribution of the total storage amount at the next time step, $N(\hat{x}(k+1|k), \sigma_{k+1})$, was calculated from the simulated results. The estimated state $\hat{x}(k+1|k)$ was the mean value of the simulated total storage amounts, and the error variance $(\sigma_{k+1})^2$ was taken as $F_kP(k \mid k)F_k^T$.
Adding the additional system error covariance Q_k completed the estimation of the error

variance $P(k+1 \mid k)$ at time step k+1. The estimated error variance $F_k P(k \mid k) F_k^T$ stands for a diffusion of the existing error variance $P(k \mid k)$ through the simulation, and Q_k denotes a generated or added system covariance during simulation from time step k to the next time step k+1. The newly added system covariance is caused by either system structure or newly input rainfall data. The methodology used to determine the system error covariance, Q_k, is discussed in the following section.

5.3 Setting the Observation and System Noise

The most difficult part of applying the Kalman filter to a hydrologic model is determining the covariance of the system and observation noise. Although the Kalman filter provides an algorithm for better forecasting by updating the state estimates, its success depends largely on an appropriate determination of the error statistics, which requires proper judgment by the hydrologist.

The basic assumption of the Kalman filter is that the system and observation noise are both white and Gaussian. This assumption is justified physically when the noise is largely caused by a number of small sources (Mayback, 1979). From this perspective, it is reasonable to regard the observation noise, which is usually corrupted by several definable error sources, as derived from a white, Gaussian distribution. In addition, an accuracy assessment test using data obtained over a long duration makes it possible to properly estimate the measurement error covariance (Kitanidis and Bras, 1980a).

However, the system error variance is a critical value for the Kalman filter, as it contains many error sources, which are difficult to define separately. The system error covariance should reflect system structure error, parameter identification error and input data error, as well as system linearization error. Underestimation of the system error leads to excessive certainty in the model behavior, and overestimated system error makes the filter too sensitive for observation values. In practice, the system error variance is usually estimated by a trial and error procedure assuming it is constant.

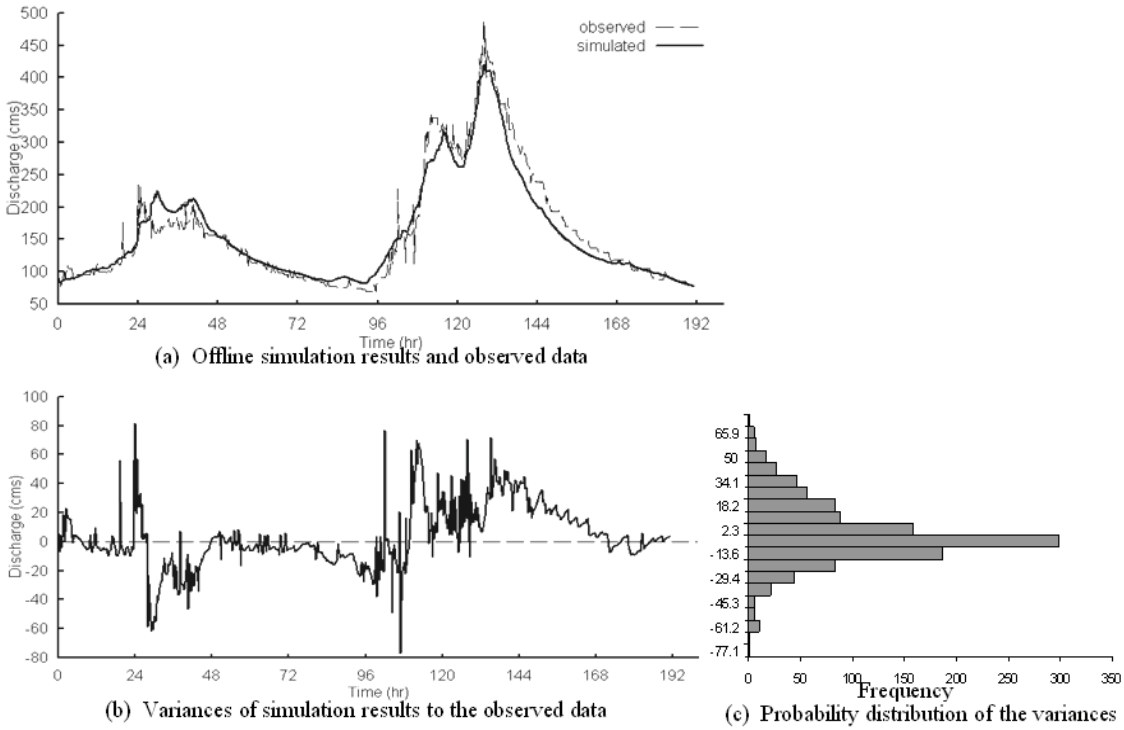

Figure 5.3 Variances of system error and its probability distribution (Event 998).

Several cases of feedback performance with various assumed error co variances were tested. The simple method used to estimate the system error covariance was as follows. If observed data were comparatively close to the absolute true values and assuming the noise was white Gaussian, the biases of simulation results to the observed values could also be regarded as system noise. When the biases were examined, the distribution of the biases was different event-by-event; however, each distribution can be regarded as a normal as shown in Figure 5.3.

Table 5.1 shows the first and second statistical moments of the biases. The mean values were around zero and the standard deviations were around $30 m^3/s$. In addition, we confirmed that the biases were distributed as a normal probability distribution. Following this analysis, the standard deviation of the biases was assumed equal to the second moment of the system noise in terms of discharge. The discharge noise was converted to the error covariance of the total storage amount Q_k. The system noise in terms of discharge was translated to the noise in terms of storage amount by use of the *Q–S* relationship as shown in Figure 5.4.

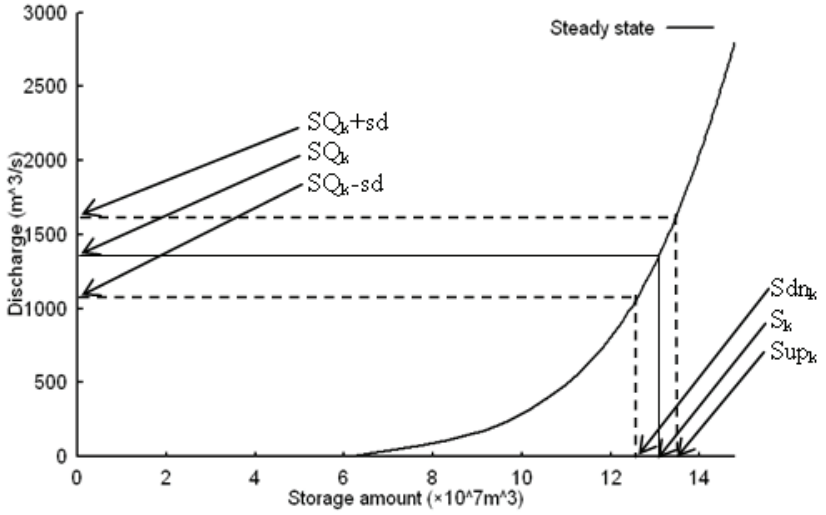

Figure 5.4 Conversion of the noise term from discharge to storage amount.

Table 5.1 Statistical values of simulation results.

Event	Mean (m^3/s)	StDev (m^3/s)
Event 979	–2.22	36.48
Event 996	–10.80	22.93
Event 998	3.32	22.11
Event 999	–1.02	25.70

Three discharges, D_k, D_k+Sd, and $D_k–Sd$, where D_k is the discharge at time step k and Sd is the second moment of the noise distribution, were converted to the three different storage amounts, S_k, Sup_k, and Sdn_k, respectively. Using the differences of storage amount, Sup_k, S_k and $S_k – Sdn_k$, the system error covariance Q_k was calculated as

$$Q_k = \left|(Sup_k - S_k) \times (S_k - Sdn_k)\right|. \tag{5.8}$$

Even if the probability distribution of the discharge follows normal probability, because the relationship between discharge and storage amount is nonlinear, the distribution of storage amount cannot strictly be considered normal. However, this nonlinear effect on the probability distribution was not significant in this study; the *Q*–*S* relationship can be taken as approximately linear over a short range.

The observation noise was also assumed to be a stationary value with a constant ratio to the system noise. Since the second moment of the system noise in terms of discharge was set to $30m^3/s$, the second moment of the observation noise was first taken as the same as the system noise. Then, three other cases were tested in the application of the Kalman filter-coupled CDRMV3: (1) both the system and observation contain noise; (2) only the system contains noise, while no observation noise exists; and (3) no system noise is present, while the observation contains noise. If there is no observation noise in the Kalman filter, the filter takes the observed value as the true value, and the feedback through the filter should match the observed data. However, if no system noise is present, the filter "believes" the system produced perfect results and ignores any other observed data. In the case when noise is present in both the system and observation, the feedback values are located in the range between the system output and the observed data.

The initial state value $x(1)$ is given automatically once the initial condition of the model is set by the outlet discharge of each event. The initial state error variance $P(1)$ takes the same value as the system error variance.

5.4 Application Results and Discussion

The Kalman filter-coupled distributed hydrologic model CDRMV3 was tested on the Kamishiiba basin under various error covariance conditions. Figures 5.5 and 5.6 show the feedback through the algorithm under the three different error conditions. In the figures, the label SN30:ON30 indicates the results from the condition that both the system and the observation are assumed to have the given noise. The labels SN00:ON30 and SN30:ON00, respectively represent feedback when no system noise is present and when no observation noise is present.

In both Figures 5.5 and 5.6, the feedback result with the condition SN00:ON30 exactly matches the off-line simulation result. Because the Kalman filter algorithm "believes" the model is perfect, it produces absolutely true values. On the other hand, the case

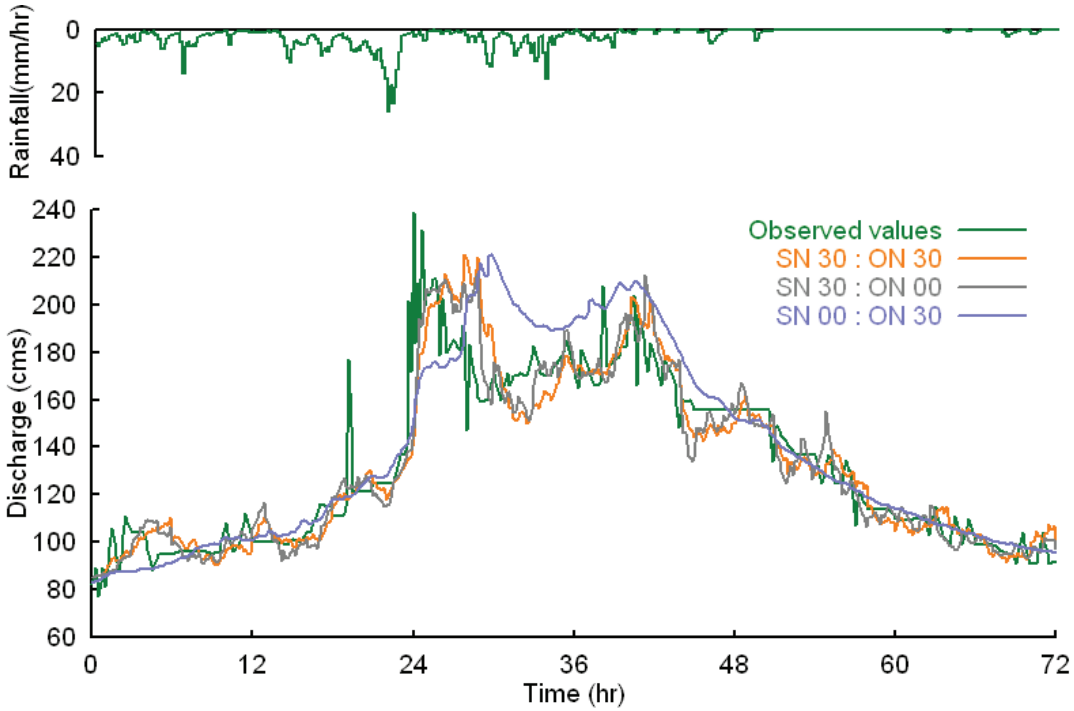

Figure 5.5 Observed and feedback values through the Kalman filter under various system and observation noise conditions (Event 998).

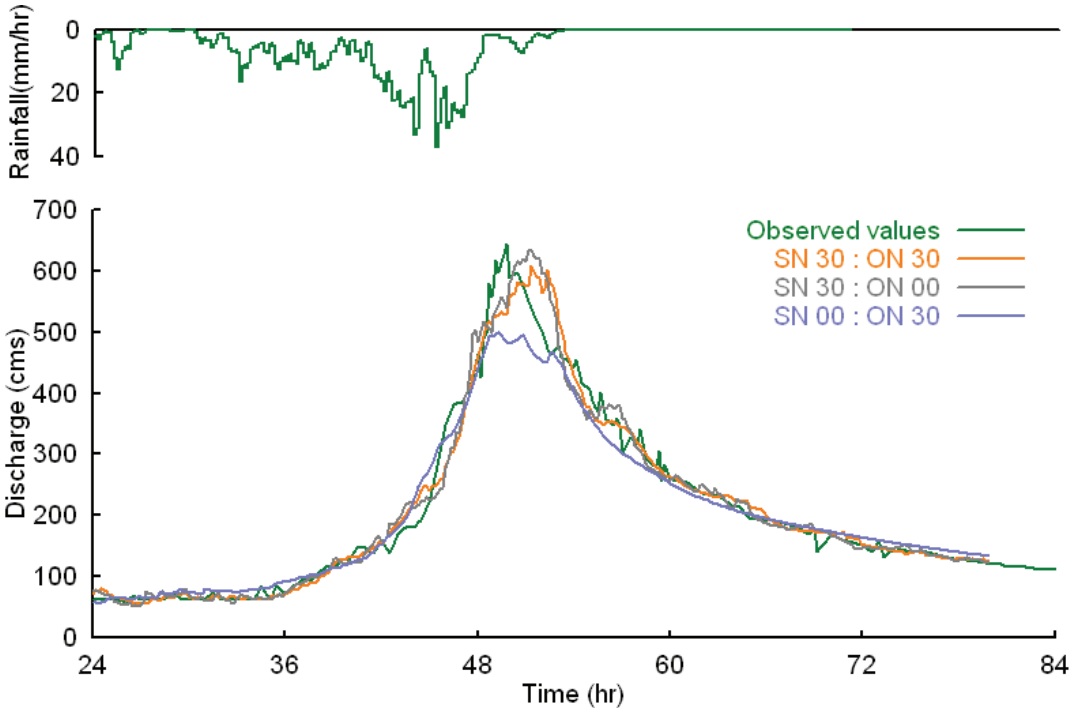

Figure 5.6 Observed and feedback values through the Kalman filter under various system and observation noise conditions (Event 999).

SN30:ON00 shows that the feedback essentially follows the observed data. The feedback is particularly satisfying at the rising limb and the falling limb of the hydrographs. However, at the peak of both events (see the hydrograph around 30 hrs in Figure 5.5 and 50 hrs in Figure5.6), the feedback shows a delayed response relative to the other parts of the simulations. This time lag around the peak was mainly caused by the *Q–S* relationship, which was derived under steady state conditions.

As mentioned earlier, the original relationship of discharge and storage amount has a looped shape. It appears that a small difference of gradient between both relationships causes little difficulty for the updating algorithm, since the rising and the falling limb show positive relativity with the observed values. However, around the peak of the hydrograph (which corresponds to around the turning point of the *Q–S* relationship loop), the relationship applied under the steady state cannot properly estimate the total storage amount because of the sudden changes of discharge under the highly unsteady conditions. As a result, the feedback produces a response from 1 hr to 2 hrs late.

The effect of the difference between steady and unsteady states on the *Q-S* curve can be explained by conceptual storage amount distributions as shown in Figure 5.7. When the steady state assumption is made, discharge and storage are expressed as a single valued function (see Figure 5.7 (a)). On the other hand, although the discharge is the same as shown in Figure 5.7 (b) and (c), different storage values occur through a runoff, which is under an unsteady state condition. The differences in storage amount at the beginning of the runoff (the difference of the Storage A and Storage B) cause the underestimation of discharge at the rising limb, while after the peak (the difference of the Storage A and Storage C) cause the over estimation at the falling limb of the hydrograph.

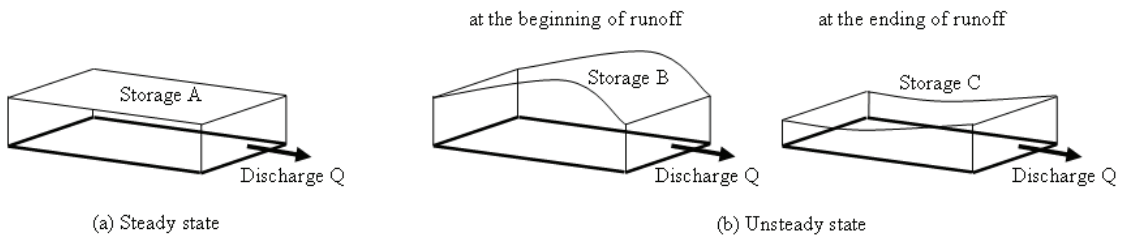

Figure 5.7 Conceptual distributions of storage amount according to state differences.

The case SN30:ON30 shows that the feedback values are between the off-line simulation results and the observed data. Even though the noise values were set to the same $30m^3/s$, the filtered results were closer to the observed data than the off-line simulation results.

Several explanations are possible for this phenomenon: a different form of error variance on the system and the observation, as well as the initial state and its error variance. While the observation error covariance in the filter is in terms of discharge, the system error covariance is in terms of storage amount transformed from the discharge noise. The initial error covariance is also believed to produce an effect on the filtered results. In practical use, appropriate system error covariance and initial error variance can be estimated by a trial and error procedure for each basin.

To check the prediction accuracy after coupling with the Kalman filter, 1 hr, 6 hrs, and 12 hrs prediction results were compared. Table 5.2 shows the root mean square error of the prediction results compared to the observed values. As expected, prediction for short lead times showed higher accuracy, and furthermore, the prediction for 12 hrs ahead produced quite good accuracy compared to the short lead-time forecasting.

Table 5.2 RMSE of prediction results (m^3/s).

EVENT	1 hr ahead	6 hrs ahead	12 hrs ahead
Event 979	37.18	39.64	37.28
Event 996	11.42	17.24	20.14
Event 998	16.45	21.93	22.17
Event 999	28.00	34.72	27.85

The main reason for the efficient prediction was the use of recorded rainfall data. The simulation and prediction were performed under the condition that the observed radar rainfall data was taken as the forecast rainfall. In practice, error in the forecast rainfall is large, and the prediction results are highly dependent on the accuracy of the input data. If the uncertainty of the rainfall forecasting is known, it should be added to the system error covariance Q_k.

The Kalman filter was successfully coupled to the distributed hydrological model, CDRMV3, to update internal distributed state variables. Rather than attempting an impractical algorithm formulation, several techniques were adopted such as use of the *Q*–*S* relationship, efficient updating of the water depth by the ratio method, and Monte Carlo simulation methods. In the measurement update algorithm, the *Q*–*S* relationship was used as the observation equation, and the ratio of total storage amount was applied for setting the water stage for each cell in the distributed hydrologic model.

For the prediction algorithm, a Monte Carlo simulation was adopted to diffuse the state variable and its error covariance. The CDRMV3 using the Kalman filter yielded more effective results than off-line simulations and can thus be used as a probabilistic forecast algorithm. The developed algorithm can incorporate the uncertainty of input and output measurement data as well as the uncertainty of the model itself.

Further work will include developing a method to apply several observations for the updating method to fully utilize the properties of a distributed hydrologic model. One way would be to define sub basins according to the location of observation stations, and to apply different factors to each sub basin for updating the spatial pattern of water depth. For nested river basins with different observation stations, sophisticated methods to define the ratio would be required.

Using the *Q*–*S* relation curve to evaluate the estimated total storage amount should also be investigated. The *Q*–*S* relationship represents the overall relation of the storage amount in a catchment to the outlet discharge under a steady state assumption. The uncertainty from the *Q*–*S* relationship should be included in the observation error variance.

References

Cooper, D. M. and Wood, E. F. (1982): Parameter estimation of multiple input-output time series models: Application to rainfall-runoff processes, Water Resources Research, Vol. 18, No. 5, pp. 1352-1364.

Evensen, G. (1994): Sequential data assimilation with a nonlinear quasi-geostrophic model using Monte Carlo methods to forecast error statistics, Journal of Geophysical Research, Vol. 99, pp. 10143-10162.

Hino, M. (1973): Runoff forecast by linear predictive filter, Journal of Hydraulic Division, ASCE, Vol. 96, No. 3, pp.681-707.

Kalman, R. E. (1960): A new approach to linear filtering and prediction problems, Transaction of the ASME – Journal of Basic Engineering, Vol. 83, pp. 35-45.

Kim, S., Tachikawa, Y. and Takara, K. (2005): Real-time prediction algorithm with a distributed hydrologic model using Kalman filter, Annual of Hydraulic Engineering, JSCE, Vol. 49, pp. 163-168.

Kitanidis, P. K. and Bras R. L. (1980a): Adaptive filtering through detection of isolated transient errors in rainfall-runoff models, Water Resources Research, Vol. 16, No. 4, pp. 740-748.

Kitanidis, P. K. and Bras R. L. (1980b): Real-time forecasting with a conceptual hydrologic model – 1. Analysis of uncertainty, Water Resources Research, Vol. 16, No. 6, pp. 1025-1033.

Krzysztofowicz, R. (2001): The case of probabilistic forecasting in hydrology, Journal of Hydrology, Vol. 249, pp. 2-9.

Lee, Y. H. and Singh, V. P. (1999): Tank model using Kalman filter, Journal of Hydrologic Engineering, ASCE, Vol. 4, No. 4, pp. 344-349.

Maybeck, Peter S. (1979): Stochastic Models, Estimation, and Control, Volume 1, Academic Press, New York.

Nash, J. E. and Sutcliffe, J. V. (1970): River flow forecasting through conceptual models, Part 1- A discussion of principles, Journal of Hydrology, Vol. 10, pp. 282-290.

Puente, C. E. and Bras, R. L. (1987): Application of nonlinear filtering in the real time forecasting of river flows, Water Resources Research, Vol. 23, No. 4, pp. 675-682.

Rajaram, H. and Georgakakos, K. P. (1989): Recursive parameter estimation of hydrologic models, Water Resources Research, Vol. 25, No. 2, pp. 281-294.

Smith, M. B., Georgakakos, K. P. and Liang X. (2004): Preface, The distributed model intercomparison project (DMIP), Journal of Hydrology, Vol. 298, pp. 1-3.

Takasao, T., Shiiba, M. and Takara, K. (1989): Stochastic state-space techniques for flood runoff forecasting, Pacific International Seminar on Water Resources Systems, Tomamu, 1989, pp 117-132.

Wood, E. F. and Szöllösi-Nagy, A. (1978): An adaptive algorithm for analyzing short-term structural and parameter changes in hydrologic prediction models, Water Resources Research, Vol. 14, No. 4, pp. 577-581.

Chapter 6

Conclusions

This study discussed stochastic real-time flood forecasting with radar image extrapolation and a distributed hydrologic model, while also presenting a real-time flood forecast algorithm. This algorithm mainly consists of two parts; 1) stochastic rainfall forecasting with a radar image extrapolation and the simulation of prediction error fields, and 2) the updating of state variables in a distributed hydrologic model using Kalman filter algorithm.

Firstly, a new attempt of ensemble rainfall forecasting was carried out with radar rainfall prediction and spatial random error field simulation. The radar extrapolation model gave a deterministic rainfall prediction. Then, its prediction error structure was analyzed by comparing the prediction fields with the observed rainfall fields. With the analyzed error characteristics, spatial random error fields were simulated using a covariance matrix decomposition method. The simulated random error fields, which successfully maintained the analyzed error structure, improved the accuracy of the deterministic rainfall prediction.

Secondly, a Kalman filter was coupled with a distributed hydrologic model to update spatially distributed state variables, and to incorporate the uncertainty of rainfall forecast data. Here, rather than attempting to formulate an impractical algorithm, several new techniques were adopted. In the measurement update algorithm, the discharge and storage amount relationship (Q–S relationship) was used as the observation equation, and the ratio of total storage amount was applied for setting the water stage for each cell in the distributed hydrologic model. For the prediction algorithm, a Monte Carlo simulation was adopted to diffuse the state variable and its error covariance from one time step to another. The distributed hydrologic model coupled with the Kalman filter made it possible to incorporate the input as well as the system uncertainty into the flood forecasting.

At each step for composing the algorithm, every procedure was carefully examined and discussed. These acquired results are provided in the next section.

Summary of the Study

The radar image extrapolation model, namely the Translation model, enabled deterministic forecasting to be produced. Upon comparing the prediction results with observed rainfall fields, the behavior of the translation model was examined. Spatially averaged rainfall intensities of prediction were compared with an observation, and it was found that there were overall delays of rainfall intensities as prediction lead-time was extended. Because the translation model only represents the movement of the rainfall bands without their growth or decay, the model assumes the same amount of current rainfall intensities lasts for the duration of each lead-time. The correlation coefficients of the observation, and the prediction in short lead-times have higher values compared to longer lead-time predictions. Even for such longer lead times, the CSI show rather high values in most prediction times.

This study analyzed the absolute prediction error and simulated the possible error fields on a real-time basis. The analyzed error characteristics include mean, standard deviation, and spatial correlation coefficients of the error. The spatial correlation coefficients show high values for close distances, and decreases as the distance enlarges. It was also found that the prediction error from longer prediction times has higher spatial correlation coefficient values, which are almost diminished around 15 km in most prediction cases. When frequency distribution of prediction error was checked, even though there was a slight variation in each event and prediction case, the distribution pattern primarily gave forth normal distribution.

For checking the spatial pattern of the prediction error, the absolute errors on each grid were accumulated event by event, and found that there was a certain spatial pattern on each accumulation. It was assumed that the wind direction and topographic pattern had

a relation to the rainfall generation and extinction, therefore eventually causing a different spatial pattern of the prediction error. However, detailed study is required in order to 1) determine whether a certain relationship between topography and the prediction error pattern exists, and 2) establish what exact type of relationship that is.

For forecast accuracy improvement and ensemble forecasting with an external error consideration, this study introduced ensemble rainfall forecasting using a stochastic error field simulation. The proposed algorithm is for offering probable variation of the deterministic prediction results from the extrapolation model, as well as improving its forecast accuracy. By means of the simulated error fields, which successfully keep the analyzed error structure, not only are probable rainfall field variations for the ensemble simulation produced but also improved accuracy of the deterministic prediction by correcting the possible prediction error becomes a result.

The extended prediction field, which is the combination of the deterministic rainfall and the simulated error, was generated, after which its stochastic validity was examined. The intensities of the extended prediction fields were distributed around the deterministic rainfall intensity and then showed a certain range, which can be regarded as a reliability band. The correlation coefficients from the extended prediction showed improved results in most prediction lead-times. On the one hand, the coefficients from the extended prediction fields have higher values compared to the values from the deterministic prediction. On the other hand, the CSI values do not show great variance between the extended and the deterministic prediction. The mean and standard deviation as well as spatial correlation coefficients of the simulated prediction error show that the statistical characteristics of the prediction error were successfully maintained through the error field simulation.

An Ensemble runoff simulation was carried out in three different catchments located within the observation range of the Miyama radar: Ootori (156 km^2), Ieno (476 km^2) and Kamo (1469 km^2). Within the three sets of the simulation results, the discharges from the ensemble simulations showed closer values to the discharges from the observed radar rainfall, which was previously identified as the reference discharge. This

illustrates the improved prediction accuracy of the extended prediction. While the ensemble runoff simulation showed highly encouraging results, it is hard to say whether the band, which stands for the reliability range of the extended prediction, can be accepted as a reasonable result. In most cases, the range was not enough in covering the reference discharges. More study for giving proper reliability range with appropriate duration on the statistic fields should be followed.

To minimize the discrepancy between simulation and observation during a runoff simulation, correcting internal state variables of a hydrologic model was tested with various methods. To avoid an unpredictable collapse of the internal model state during a simulation, the update method used in this study retains the spatial distribution pattern of the state variables This factor application, called the ratio method, can be classified into two methods by way of factor calculation. The first is the *S*-ratio method using the ratio of the total storage amount in a basin, and the second is the *Q*-ratio method using the ratio of the discharge at the outlet of a basin.

After the Kalman filter was coupled with the CDRMV3, the performance of the coupled model was tested on a real-time basis. The CDRMV3 using the Kalman filter not only yielded better results than non-filtering simulations, but also presented the reliability of the performances, thus proving able to be used as a probabilistic forecast algorithm. The developed algorithm incorporates the uncertainty of input and output measurement data as well as the uncertainty of the model itself.

For the incorporation of the filtering concept with a distributed model, various developed techniques were implemented. Firstly, the Monte Carlo simulation method made it possible to project the nonlinear variation of system states and their error covariance without the need for linearized system equations. Secondly, as an alternative to the linear observation function, this study introduced an external relationship of observed data and internal state variables within the hydrologic model. The Kalman filter algorithm updates the total amount of storage in the basin, and a ratio of the updated and simulated storage amount is calculated and applied to each of the internal state variables on a fine grid cell.

The distributed hydrologic model CDRMV3 coupled with the Kalman filter was tested on the Kamishiiba basin under various error covariance conditions. When no system error was assumed in the filter, the feedback results exactly matched those of the off-line simulation. Furthermore, when the system contained no observation errors, for the most part, the feedback followed the observed data. However, upon closer examination of the results, specifically at the peak of the simulation, the feedback showed a delayed response. This time lag around the peak of the hydrograph was mainly caused by the *Q*–*S* relationship, which was produced under steady state conditions. In order to evaluate the estimated storage amounts, further investigation into the usage of the *Q*-*S* relationship curve should be considered.